Pan African University
PAU Institute of Water and Energy Sciences

PAN-AFRICAN UNIVERSITY
INSTITUTE FOR WATER AND ENERGY SCIENCES
(including CLIMATE CHANGE)

Master Dissertation

Submitted in partial fulfillment of the requirements for the Master degree in

Energy Engineering

Presented by

Yassine, Mohammed KEBBATI

DESIGN, MODELLING AND CONTROL OF A GRID-CONNECTED HYBRID PV-WIND SYSTEM (CASE STUDY OF ADRAR)

Defended on 05/09/2018 Before the Following Committee:

Chair	Boumediene Benyoucef	Professor	U.A.B-Tlemcen
Supervisor	Lotfi BAGHLI	Professor	U.A.B-Tlemcen
External Examiner	Alexander POGREBNOI	Professor	U.A.B-Tlemcen
Internal Examiner	Latifa NEGADI	Professor	N.M.A.I.S.T-Arusha

This research thesis is submitted in partial fulfillment of the requirements of the Master of Science in Energy Engineering at the Pan African University Institute of Water and Energy Sciences (including Climate Change)-(PAUWES) at the University of Tlemcen in Algeria.

September 2018.

DECLARATION

I, **KEBBATI Mohammed Yassine** do hereby declare that this thesis is my original work and to the best of my knowledge, it has not been submitted for any award in any University or Institution.

Signed_____ Date _____

KEBBATI Mohammed Yassine 10/08/2018

CERTIFICATION

This thesis has been submitted with my approval as the supervisor

Signed  Date_____

Prof. BAGHLI Lotfi 08/08/2018

ABSTRACT

Most countries are planning to increase their power supply capacities and diversify resources for electricity generation. In Africa, ambitious objectives in this regard, have been set by many countries. Large scale renewable energy power plants are primordial for increasing the renewable energy share in the total energy mix, though they are rare in African countries except for the case of hydropower. In February 2015, the Algerian government adopted an ambitious Renewable Energy Program planning the installation of 22 GW of Renewable Energy by 2030 [1]. However, the major challenge to the development of such programs are the subsidized electricity prices in the country, these low prices result in one of the highest irrational energy consumptions in the continent. Due to its semi-arid to arid climate, the country witnesses very high power-demand in summer, caused by accumulated cooling loads. The national grid often struggles to deliver such power resulting in electricity outages and blackouts, especially in the southern part of the country.

In the present thesis, a general review is conducted on different renewable energy resources in Algeria, the solar and wind energy potential in Adrar is investigated along with the climate conditions. A state-of-the-art review on photovoltaic, wind and hybrid energy systems is carried out. Technologies used in each of the systems are revealed and the control techniques employed in the different components of the systems are also presented.

The city of Adrar, situated in the south-west of Algeria, was chosen as the case study of this work because of the available solar and wind energy potential. Another reason for this choice is the power outages and poor performance of the grid noticed during the summer season. Therefore, to tackle overload problems and contribute to the Algerian Renewable Energy Program, a hybrid grid-connected PV-wind system has been designed and modelled in MATLAB/SIMULINK. The control mechanisms for the different components of the system have been studied and modelled, and the sizing of the system was based on the available potential of solar and wind energies and on the electricity demand of the city for two critical seasons (Winter and Summer).

The performance of the implemented control techniques proved to be robust, and the modelled system was simulated in SIMULINK for the months of January and August. METEONORM software was used to provide the weather file for Adrar, which contains hourly data for solar irradiation, wind speeds and temperature. It was found that the designed system contributes to the performance of the grid by a minimum of 10% and a maximum of 200%, depending on the available potential. Moreover, an economic and environmental analysis of the system was undertaken in HOMER software. Although, the overall cost of the system was evaluated at $42.1 million, the levelized cost of electricity (LCOE) was found as low as 0.084 $/kWh due to the feed in tariffs policy adopted in the country, thus the system proved to be very profitable. Furthermore, the hybrid system helped mitigating global warming and climate change by reducing a significant amount of greenhouse gas emissions, that would rather be emitted by conventional natural gas power plants.

Key words: Renewable Energy, Photovoltaic, Hybrid Energy Systems, METEONORM, MATLAB, HOMER, LCOE, Global warming.

RÉSUMÉ

La plupart des pays prévoient d'augmenter leurs capacités à fournir de l'énergie et de diversifier leurs ressources pour la production d'électricité. En Afrique, des objectifs ambitieux à cet égard ont été fixés par de nombreux pays. Les centrales à énergie renouvelable à grande échelle sont primordiales pour augmenter la part des énergies renouvelables dans le mix énergétique total, bien qu'elles soient rares dans les pays africains à l'exception du cas de l'hydroélectricité. En février 2015, le gouvernement algérien a adopté un programme d'énergie renouvelable ambitieux prévoyant l'installation de 22 GW d'énergie renouvelable d'ici 2030 [1]. Cependant, le principal défi au développement de tels programmes sont les prix subventionnés de l'électricité dans le pays, ces bas prix entraînent l'une des consommations d'énergie irrationnelle les plus élevées du continent. En raison de son climat semi-aride à aride, le pays connaît une forte demande d'énergie en été, causée par les charges de refroidissement. Le réseau national a souvent du mal à fournir une telle puissance, ce qui entraîne des coupures d'électricité, plus particulièrement dans le sud du pays.

Dans le présent mémoire, une étude générale est menée sur différentes ressources d'énergie renouvelable en Algérie, le potentiel d'énergie solaire et éolienne dans la région d'Adrar est étudié, ainsi que le climat. Une revue de l'état de l'art sur les systèmes photovoltaïques, éoliens et hybrides est réalisée. Les technologies utilisées dans ces systèmes sont révélées et les systèmes de commande employées dans les différents composants des systèmes énergétiques sont également présentées.

La ville d'Adrar, située dans le sud-ouest de l'Algérie, a été choisie comme cas d'étude dans ce travail en raison de son haut potentiel d'énergie solaire et éolienne disponible. Une autre raison de ce choix sont les coupures fréquentes et la mauvaise performance du réseau électrique constatée pendant la saison estivale. Afin de faire face aux problèmes de surcharge et contribuer au programme d'énergie renouvelable algérien, un système hybride PV-éolienne connecté au réseau a été conçu et modélisé sur MATLAB / SIMULINK. Les systèmes de contrôle des différents composants du système ont été étudiés et modélisés, et le dimensionnement du système a été basé sur le potentiel disponible des énergies solaire et éolienne et sur la charge d'électricité dans la ville en question pour deux saisons critiques (hiver et été).

Les performances des systèmes de commande utilisées ont prouvé leur robustesse et le système modélisé a été simulé sur SIMULINK pour les deux mois de Janvier et Août. Le logiciel METEONORM a été utilisé pour fournir le fichier météo d'Adrar, qui contient les données horaires de l'irradiation solaire, la vitesse du vent et la température. Il a été constaté que le système conçu contribue à la performance du réseau par un minimum de 10% et un maximum de 200%, en fonction du potentiel disponible. De plus, une analyse économique et environnementale du système a été réalisée sur le logiciel HOMER. Bien que le coût global du système ait été évalué à 42,1 millions de dollars, le coût actualisé de l'électricité (LCOE) a été jugé aussi bas que 0,084 $/kWh en raison de la politique de tarifs de rachat adoptée dans le pays. Ainsi, le système s'est révélé très rentable. D'autre part, le système hybride a contribué à l'atténuation de réchauffement et changement climatique en réduisant une quantité importante d'émissions de gaz à effet de serre, qui seraient plutôt émises par les centrales au gaz naturel conventionnelles.

Mots clés : Energie Renouvelable, Photovoltaïque, Systèmes Énergétiques Hybrides, METEONORM, MATLAB, HOMER, Coût actualisé d'électricité, Changement climatique.

ACKNOWLEDGEMENTS

I am extremely beholden to Allah and tremendously grateful for his blessing without which I would never have succeeded. I am largely indebted to my family for their unique and exceptionally continuous support and I thank them for their strong faith in me, for their essential help and their precious prayers.

I address my sincere respect and gratitude to the African Union Commission and thank them for the Master's scholarship that I have benefited from through PAUWES. I also express my regards and appreciation to the thematic partners and sponsors. My acknowledgment and high esteem go to the administration of PAUWES and the host institution

I am appreciative to my supervisor, Professor Lotfi BAGHLI, and I thank him for his significant support and guidance. I am also very thankful to my friend Younes DRIS who helped me a lot and contributed to this work. I am thankful to the director of PAUWES Professor Abdellatif ZERGA and to my friend and brother Djamel Eddine BENHADJI SERRAJ at large.

I am especially thankful to all the jury members for accepting to review and evaluate my work. To all those who helped me from far or close, who guided me directly or indirectly, who simply have been there for me, THANK YOU!

TABLE OF CONTENTS

LIST OF FIGURES

LIST OF TABLES

NOMENCLATURE

AC:	Alternating Current
BIPV:	Building Integrated PV
BOS:	Balance of System
CAES:	Compressed Air Energy Storage
CDER:	Centre de Développement des Énergies Renouvelables
CG:	Centralized Generation
DC:	Direct Current
DFIG:	Doubly Fed Induction Generator
DG:	Decentralized Generation
DHI:	Diffuse Horizontal Irradiation
DNI :	Direct Normal Irradiation
ET :	Equation of Time
FF :	Fill Factor
GDP	Gross Domestic Product
GHI:	Global Horizontal Irradiation
GTI	Grid Tie Inverter
GSC:	Grid Side Converter
HAWT:	Horizontal Axis Wind Turbine
HRES:	Hybrid Renewable Energy Systems
IC :	Incremental Conductance
IGBT:	Insulated Gate Bipolar Transistor
LCOE:	Levelized Cost of Electricity
MOSFET:	Metal Oxide Semiconductor Field Effect Transistor
MPPT:	Maximum Power Point Tracking
NPV:	Net Present Value
NREL:	National Renewable Energy Laboratory
P&O:	Perturb and Observe
PCU:	Power Conditioning Unit
PLL:	Phase Lock Loop
PM:	Permanent Magnet
PV:	Photovoltaic
PWM:	Pulse Width Modulation
RSC:	Rotor Side Converter
SMES:	Superconducting Magnetic Energy Storage
SRC:	Specified Rated Capacity
STC:	Standard Testing Conditions
SVF:	Sky View Factor
SVC:	Static Var Compensator
TSR:	Tip Speed Ratio
VAWT:	Vertical Axis Wind Turbine
UT:	Universal Time

CHAPTER ONE: GENERALE INTRODUCTION

Outline

1.1. Introduction

In this part, an overview of the hydrocarbon sector in Algeria is conducted, and the impact of fossil fuel dependency on the economy of the country is highlighted. The energy situation in Algeria is explained and the renewable energy potential is discussed briefly. A review of the Algerian renewable energy program is given along with the share of each technology in the total program production capacity. The main problem addressed by this thesis is stated and the objectives are listed with the scope of the study.

1.2. Background Information

Algeria plays an important role in the sector of hydrocarbons, the daily production in the country exceeds 1.54 million barrels of crude oil, and 92.1 billion cubic meters of natural gas. These two nonrenewable sources of energy are the backbone of the economy, their exports account for nearly 20% of the gross domestic product, and about 85% of total exports [2].

The reliance on fossil fuels in Algeria has a huge effect on its economy as the latter is mostly based on exporting oil and natural gas whose prices are not stable. Over the last years, the fall of oil prices has widely affected the economy resulting in a huge deficit in the country's budget.
Between 2014 and 2016, the price of one barrel of oil fell from $100 to $45.13, due to the fact that the country's economy is mainly dependent on hydrocarbon exports, the total revenues were reduced by two thirds, dropping from $60 billion in 2014 to less than $20 billion in 2016. With this sharp decline, the country's gross domestic product (GDP) fell from $235 billion in 2014 to $160 billion in 2016. In 2015 for instance, the state's budget reached its lowest record at -15.3% of the total GDP.

The country provides major subsidies for electricity and oil prices, electricity for instance costs 0.038 $/kWh, which is among the lowest prices in the world. These subsidies started decreasing since the oil crisis emerged, and fossil fuel prices are now growing more and more expensive. To aggravate the situation, electricity consumption in Algeria will reach 83 TWh in 2020 and roughly 150 TWh in 2030. In the light of the projection studies, oil reserves will last only for the next 50 years, while natural gas will cover the next 70 years [3]. On the other hand, the country emits a big amount of greenhouse gases, thus integrating renewable energies should decrease fossil energy dependency and reduce greenhouse gas emissions.

Worldwide energy consumption in the year 2012 had a respectable share of 19% from renewable sources, the contribution of renewable energy continued to rise year after year reaching 19.3% in 2015, of which 1.6% goes to solar, wind, biomass and geothermal power combined [4]. Algeria is home to one of the world's greatest solar deposits, the duration of sun exposure is more than 2,000 hours a year, up to 3900 hours in the highlands and the desert. This means that the country enjoys from 1,700 to 2,263 kWh/m^2/year of solar energy [5]. The south of Algeria has a significant wind resource, especially the region of Adrar where average wind speeds range from 4 to 6 m/s, which makes it very attractive for installing wind farms [5].

The government of Algeria is trying to attract investments in wind and solar energies by establishing suitable policies with the aim of installing 5 GW of wind power and 13.6 GW of solar PV by 2030. Moreover, the country launched in 2011 an ambitious renewable energy and energy efficiency program with the vision of developing and diversifying renewable energy resources. The goal of the program is to install 22,000 MW by 2030, of which 10,000 MW is aimed to be exported to the European market and 12000 MW is dedicated to the national market [6]. The distribution and share of renewable energy technologies is shown in the figure below.

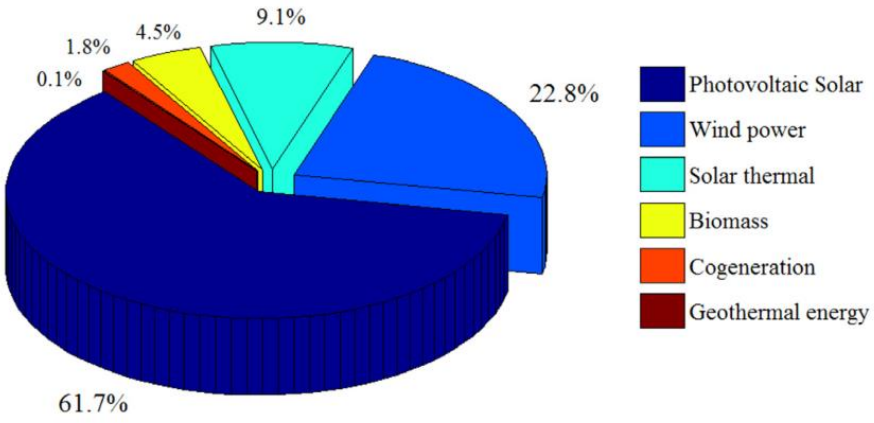

Figure 1.1: Share of technologies in the renewable energy and energy efficiency program [6].

1.3. Problem Statement

Algeria is a large country situated in the north of Africa, it is endowed with solar energy, and some regions of the country receive respectable amounts of wind as well. Despite The high electrification rate of 99% in the country, electricity provision faces numerous blackouts and shortages especially during summer, because of the hot climate and the need for air conditioning. The case for the southern part is worse since the cooling loads are higher due to the Saharan climate that prevails in the southern provinces, in addition to low power supply and grid disconnection between the north and the south.

Renewable energy resources vary in nature, solar and wind proved to be intermittent and this fact makes them a bit tricky to harness, because their intermittency creates challenges to maintaining a continuous and reliable power supply. In grid-connected systems, it is even more difficult especially in the case of weak grids that are not able to handle the fluctuation of power generation when the amount of integration of solar or wind is important. Hybrid systems can tackle this issue, combining solar PV with wind is an attractive solution that provides reliable and economical renewable power generation. Therefore, this work aims at empowering the national grid capability by integrating a share of production from solar and wind energies.

The study focuses on the design of a grid-connected PV-wind system, and the modelling and simulation of the system with relevant data to determine its performance and contribution to the national grid. The system will comprise of a small wind farm coupled with a small PV power plant and employs different control systems including maximum power point tracking to maximize power extraction. The case study was picked based on the available potential of wind and solar energies.

1.4. Research Questions

1) Can the hybrid energy system, consisting of a small wind farm and a small PV plant, provide continuous power to the region of Adrar considering the available potential?
2) Is it possible to harvest the maximum energy from wind and solar irradiation relying on MPPT technique?
3) To what extent is the suggested hybrid energy system able to improve the performance of the national grid?
4) What contribution will the hybrid energy system bring to the economy and what are its environmental impacts?

1.5. Objectives

1.5.1. General objective

The main objective is to design a grid-connected hybrid renewable energy system that will enhance the power supply in the region of Adrar, reduce power shortages and improve the performance of the national grid.

1.5.2. Specific objectives

- Provide a design for a small wind farm and PV power plant that enables the system to fully exploit the potential of wind and solar energies in the region.
- Incorporate control techniques to control the different elements of the system and ensure power injection into the grid.
- Apply maximum power point tracking algorithms to maximize the energy output from the hybrid system.

1.6. Scope of the Study

The case study of this thesis is the city of Adrar, it is located in the south west of Algeria and has significant solar and wind resources. Data like wind speed, solar radiation and temperature for the specified location, will be generated by METEONORM software. Electricity consumption data will be collected from the national company for electricity distribution (Sonelgaz).

The sizing of the system will depend on the available energy potential and the electricity demand to choose the number and type of PV modules and wind turbines. With the help of MATLAB software, a Simulink model will be built and it will incorporate the different components of the system (PV panels, wind turbines, DC-DC converters, DC-AC inverters, etc.). Appropriate control techniques will be modelled for the different components of the system and maximum power point trackers will also be programmed for the system to ensure maximum power extraction from the available resources.

The simulation will take place under Simulink using the obtained data for the region of Adrar. Charts and graphs will be generated for interpretation and system performance evaluation.

Finally, an economic study of the system will be undertaken using HOMER software. The cost of the system will be calculated and analysed including the capital cost and the operating and maintenance cost in order to determine the payback time of such investment. The LCOE will be evaluated and compared to the price of grid electricity to assess the profitability of the system and its economic contribution. Environmental impacts of the system will also be studied and highlighted.

CHAPTER TWO: LITERATURE REVIEW

Outline

2.1. Introduction

In this chapter, an overview of the potential of different renewable energies in Algeria is done, the abundant resources are discussed in details witch recent numbers and figures. The case study is defined along with its climate conditions, the wind and solar energy potential in the area is studied in depth. In the subsequent sections, a literature review is conducted on solar photovoltaic systems covering the working principle and technologies of PV systems as well as the types and components of such systems. Wind energy systems are also reviewed, the basics are exposed and the control schemes of wind turbines are presented. The effect of wind power penetration is also discussed. Finally, an overview of hybrid energy systems, their types and topologies is presented.

2.2. Renewable Energy Potential in Algeria

Algeria is known of its important potential in hydrocarbon resources, but it also houses a huge solar energy potential thanks to its location in the Mediterranean basin. The southern part of the country receives more sunshine as it lies exactly in the sunbelt. Wind energy is the second most abundant resource with speeds ranging from 2 to 6 m/s, half of the country's surface shows a considerable average wind speed that favors wind energy utilization [6].

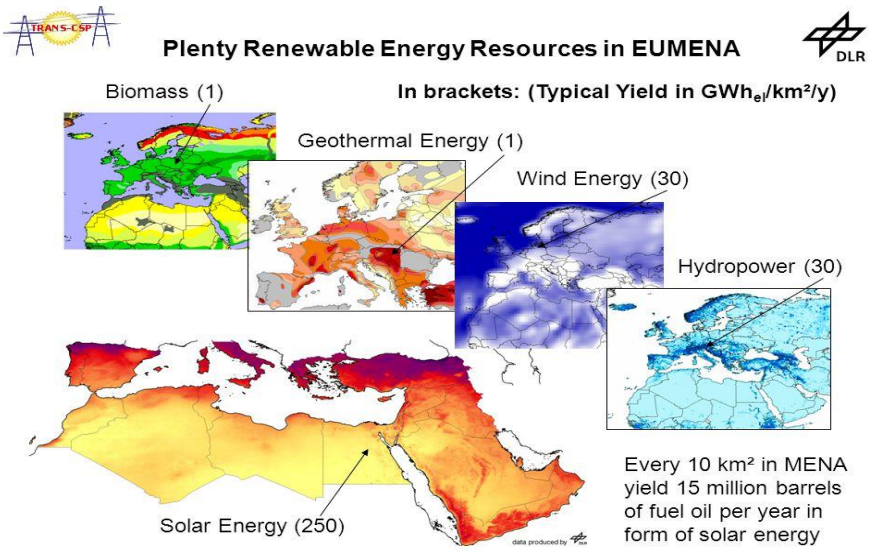

Figure 2.1: Renewable energy resources in the EUMENA [7]**.**

Other resources such as hydropower, biomass and geothermal energy have lower potentials as illustrated in the figure above showing a variety of renewable energy resources in the EUMENA according to their considerable potential.

2.2.1. Solar energy potential in Algeria

According to its geographical location, Algeria has one of the biggest solar potentials. Indeed, following a satellite assessment, the DLR (German Aerospace Center) concluded that the country has the biggest solar potential in the Mediterranean basin with 169,440 TWh per year allocated to thermal solar applications, and 13.9 TWh/year for Photovoltaics (see Figure 2.2) [8].

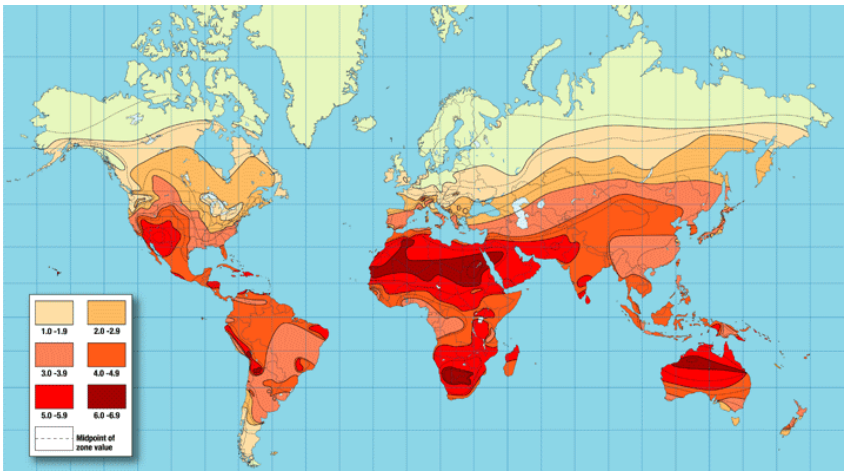

Figure 2.2: Solar insolation in the world [6].

Sunshine lasts over 2000 hours per year on almost all the country and can easily reach 3900 hours in the Highlands and the Sahara, thus the global average irradiation is very high as seen in Figure 2.3. The daily amount of energy that can be obtained on a horizontal surface is nearly 5 kWh on the major part of the national territory, about 1700 kWh/m²/year for the north of Algeria and 2263 kWh/m²/year for the southern part [8].

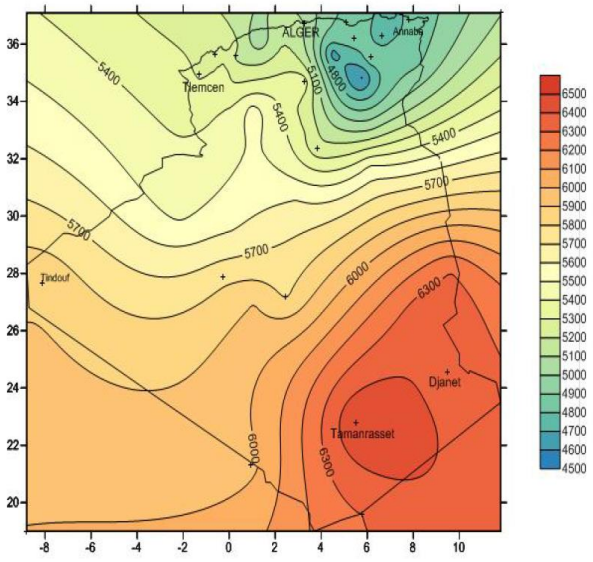

Figure 2.3: Average, yearly, global irradiation on a horizontal plane in Algeria (in kWh/m²/day) [9]**.**

The climate situation in the country is favorable for developing solar energy on account of the abundant sunshine throughout the year, especially in the desert, with daily capacities varying form 7.26 kWh/m² in the south to 4.66 kWh/m² in the north of Algeria [10].

Since Algeria is a vast country, its climate conditions are diversified, which in turn results in a variable solar potential. The average duration of sunshine and average received energy is depicted in Table 2.1. The south of Algeria receives continuous sunshine for nearly 10 hours every day, thus acquiring the highest energy as well, while coastal regions enjoy a little more than seven hours of daily sunshine and a minimum of 1700 kWh/m²/year.

Table 2.1: Average solar energy and sunshine duration by region [9]**.**

Region	**Coastal**	**Highlands**	**South**
Areas (%)	4	10	86
Average duration of sunshine (Hours/year)	2650	3100	3600
Received average energy (kWh/m²/year)	1700	1900	2650

2.2.2. Wind energy potential in Algeria

The resources of wind energy in Algeria change widely from one place to another. This is mainly due to the diversified topography and climate [11]. The vast country is subdivided into two large geographical areas, the Northern Mediterranean area is known by a long coastline of 1200 km and mountainous terrain represented by two chains; the Tellian and the Saharan Atlas. Between these are plains and highlands with a continental climate. The south is recognized by a Saharan climate. Figure 2.4 below, shows that the south has wind of higher velocities than the north; this is particularly correct in the south-west where speeds are greater than 4 m/s and surpass 6 m/s in the region of Adrar making it the windiest part of Algeria.

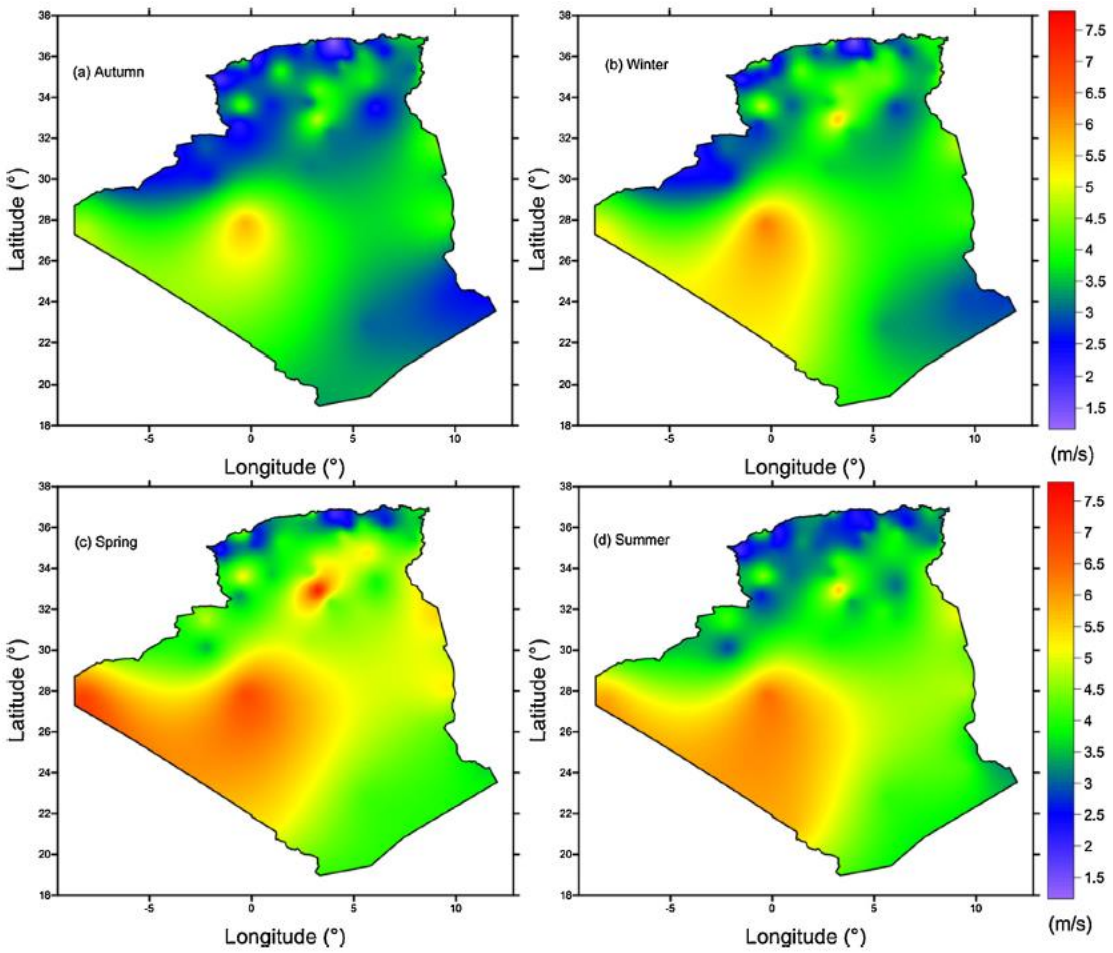

Figure 2.4: Distribution of seasonal mean wind speed in Algeria (10 m altitude) [10].

The south-western region has a significant wind potential because it is located in an area of pressure difference, and being close to the Atlantic Ocean makes it prone to high intensity weather disturbances. For the northern part, it appears that the average velocity is low. However, micro climates are still observed in the coastal areas of Annaba, Oran and Bejaia, on the highlands of Tiaret and Kheiter, including the region bounded by Bejaia in the northern part and Biskra in the southern part. Table 2.2 illustrates average wind speeds in sites of most important potentials, it appears that Adrar is the most suitable site for wind applications since it has significantly higher wind speeds.

Table 2.2: Wind velocities in Algeria's windiest regions [12]**.**

Sites	Adrar	Tindouf	Bordj Badji Mokhtar	Bechar	Tamanrassat	Djanet
Annual Average Speed (m/s)	6.3	5.1	4.6	4.4	3.7	3.3

The total wind potential in Algeria is estimated at 37 TWh per year, from which, one TWh lies on the coast, and 4.5 TWh on the highlands, while the remaining 31.5 TWh are available in the Sahara. A first wind farm shown in Figure 2.5 was completed in 2013 in order to harness some of the available wind energy in Adrar. The farm is located in Ksar Kabertene and generates up to 10.2 MW with an installation of 12 Gamesa 850 kW turbines [3][9].

Figure 2.5: Kabertene wind farm in Adrar [13]**.**

2.2.3. Geothermal energy potential in Algeria

Algeria does not lack commercially exploitable sources of geothermal energy. The potential is fair and, in some regions, can even be exploited for renewable electricity production. The center of development of renewable energies (CDER) conducted studies in the field and reported more than 200 hot springs where the highest temperatures registered were 98 °C and 118 °C in Hammam El Maskhoutin and in Biskra respectively. These natural outflows from the existing reservoirs (see Figure 2.6) have a flow rate of more than 2 m^3/s [14].

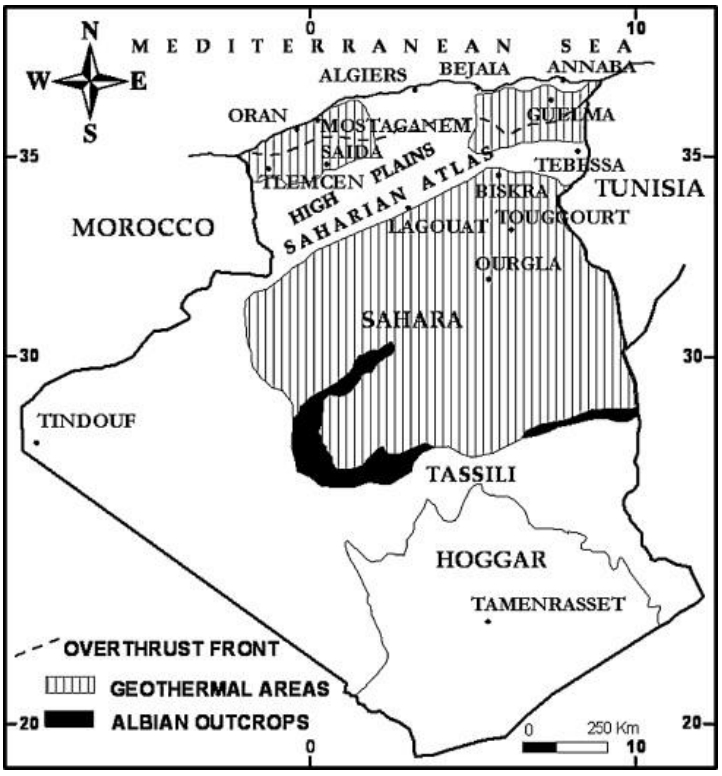

Figure 2.6: Geothermal resources in Algeria [14]**.**

In the Sahara, the continental rock formation, called the ‘‘Albian platform’’, extends over thousands of km² constituting a huge geothermal reservoir. This reservoir has outflows of hot water of 57 °C flowing at a flow rate of over 4 m^3/s [14].

2.2.4. Biomass energy potential in Algeria

Biomass resources are fair in the country; forests provide 37 Million TOE (Tons oil equivalent) recoverable at a rate of around 10%. Urban and agricultural wastes also present 5 million tons amounting to 365 kg of urban waste per Algerian. The total deposit is 1.33 million TOE/year. Despite the important potential, exploitation is still minimal and need to be enhanced. Moreover, a pre-survey showed the feasibility of electricity production by modals of 2 MW that can reach a peak of 6 MW from the discharge of Oued Smar in Algiers [15].

2.2.5. Hydropower energy potential in Algeria

Hydropower represents the second largest share or energy production from renewable resources, the technology is mature and has been used for a very long time. Algeria benefits from important water flows estimated at 65 billion cubic meters, but these are underexploited due to restrained rainfall days, high evaporation and quick evacuation to the sea. The surface resources decrease from north to south, and only about 25 billion cubic meters are deemed useful for energy production. Records show 103 dam sites of which more than 50 dams are currently operational. The largest 13 dams have a capacity of only about 269 MW shown in the table below [15].

Table 2.3: Largest hydropower dams in Algeria [15]**.**

Plant	Installed power (MW)
Darguina	71.5
Ighil Emda	24
Mansouria	100
Erraguene	16
Souk El Djemaa	8.085
Tizi Meden	4.458
Ghrib	7
Ighzernchebel	2.712
Gouriet	6.425
Bouhanifia	5.7
Oued Fodda	15.6
Beni Behdel	3.5
Tessala	4.228
Total	269.208

2.3. Case Study of Adrar

Adrar is the second largest province in Algeria after Tamanrasset, it is situated in the heart of the Algerian desert with a huge area of roughly 427368 km², it has been selected for this study due to its potential in both wind and solar energies. The district of Adrar is located precisely at 27.52° north of latitude and 0.17° west of longitude, it occupies 663 km² of the whole province and has a population of about 65000 inhabitants. Although it is a vast district, the inhabitants live mainly in the city of Adrar with a population density estimated in January 2011 at 1.01 Inh/km² [16]. The climate in Adrar is a Saharan arid one. As for the topography, Adrar is characterized by a relatively flat terrain with the highest point reaching 421 meters. The following figure is a map of the province with its districts.

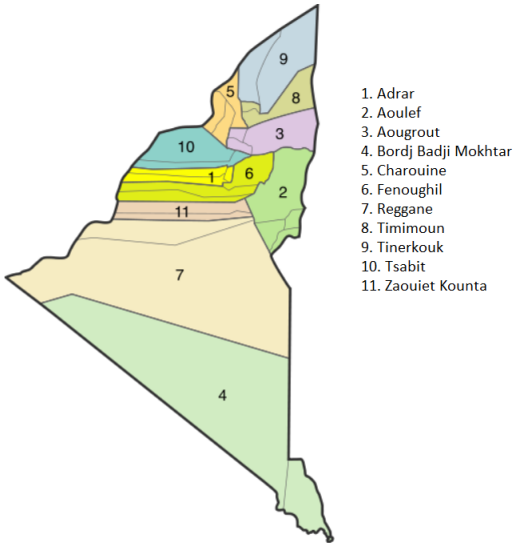

Figure 2.7: Map of Adrar province [17]**.**

Algeria is covered by the national grid and Adrar makes no exception, the network in the region consists of two power lines of lengths of 190 and 274 km, linking the district to other cities. Locally, the network houses 4542 km of lines of which 3142 km are medium voltage lines and 1400 km are low voltage lines. The network is mainly supplied by the central gas turbine power plant of Adrar with a capacity of 115 MW, other small power plants help with a capacity of 13.26 MW. The population has been growing significantly lately, which in turn, lead to a growth of 5% per year in electricity demand [16].

2.3.1. Solar energy potential in Adrar

Algeria is adequate for the use of solar energy systems, since it has a high solar potential, particularly in the southern regions. Based on hourly global irradiation data on a horizontal surface, the region of Adrar is distinguished with a higher average daily irradiation of up to 5.7 kWh/m^2/day as shown in Figure 2.8. Winter is characterized by less solar potential where the average global radiation on a daily basis varies between 3 kWh/m^2/day and 4 kWh/m^2/day. However, from March to October, solar radiation becomes very important and the average daily global radiation varies between 5.5 kWh/m^2/day and 7.5 kWh/m^2/day [18].

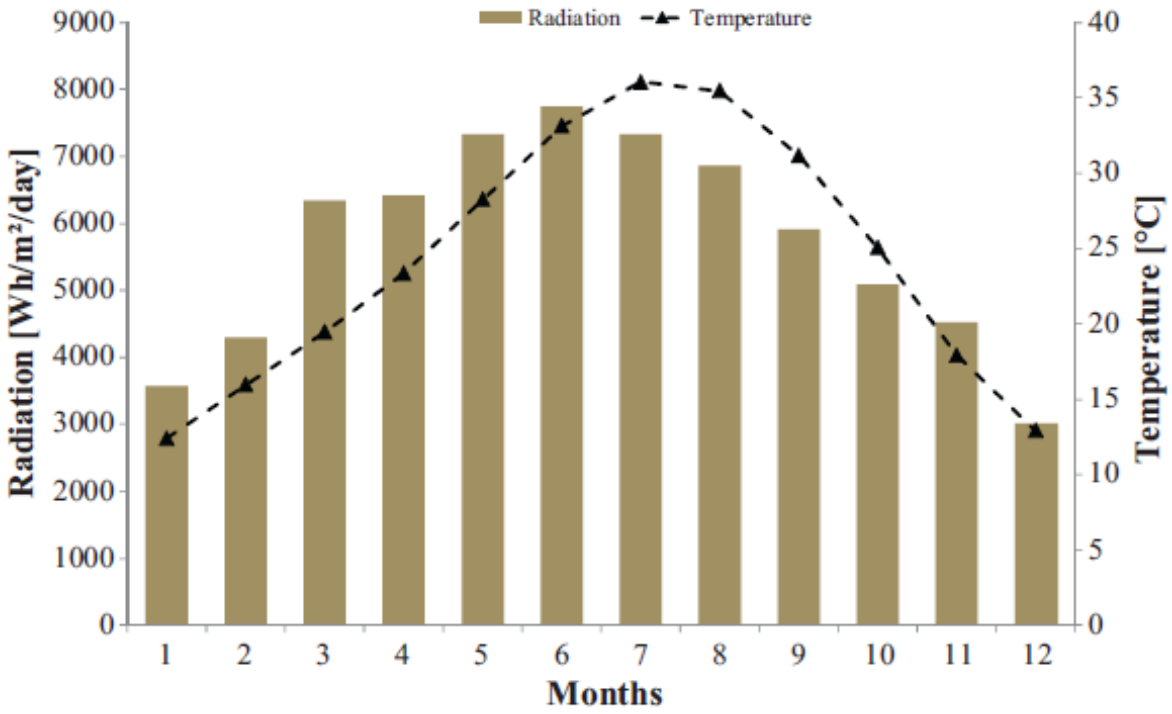

Figure 2.8: Average daily radiation and monthly temperature in Adrar [18]**.**

In a study conducted by (B. Bouzidi, 2011), it was shown that the tilt angle of a PV array plays an important role in terms of received irradiance as seen in Figure 2.9 below. The hourly global irradiance received by a tilted PV array is much more important compared to the hourly global irradiance on a horizontal plane. The values vary significantly between 600 and 1000 Wh/m^2 for the month of January [18].

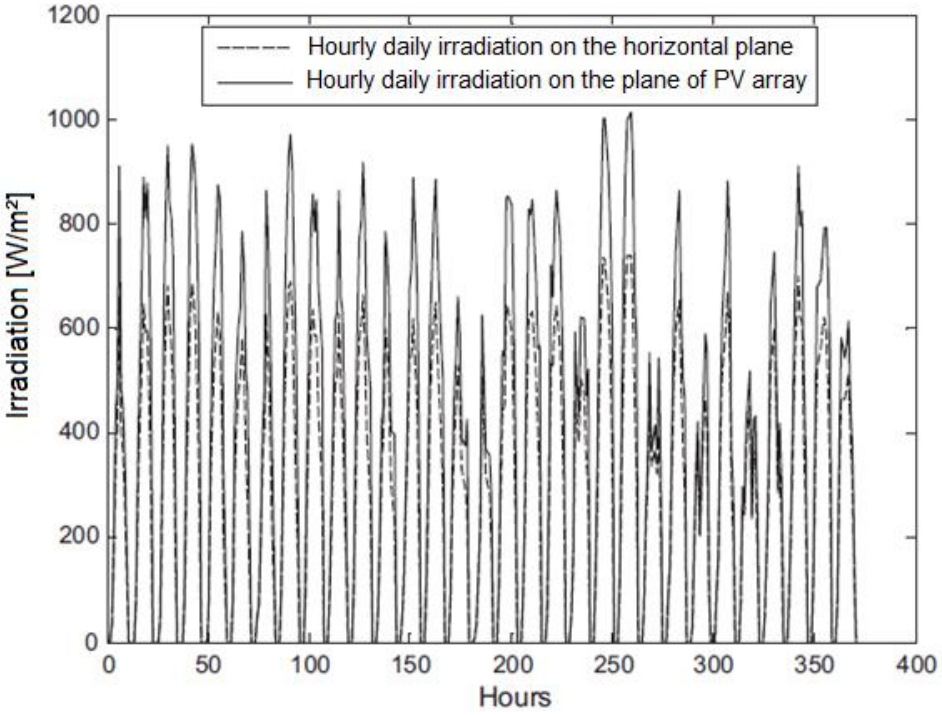

Figure 2.9: Hourly global irradiation on a horizontal\tilted plane in Adrar (January) [18]**.**

The government aims to generate 27% of its energy from renewables by the year 2030 and has already commissioned six grid-connected solar power plants having a capacity of 48 MW in the province of Adrar. A 20 MW solar power plant near Adrar city, and three other plants in the southern part, one of (6 MW) and two of (5 MW) in the communes of Zaouiet Kounta, Reggane and Aoulef respectively. Two more solar power plants of (9 MW), and (3 MW) were commissioned as well in the communes of Timimoune and Tsabit respectively [19].

In addition to solar power plants, many more installations have been realized so far, namely 28 solar pumping stations, 20 solar water heaters, and beacons covering 820 km of track [20].

2.3.2. Wind energy potential in Adrar

The region of Adrar is favorable for the installation of wind energy systems, judging by the available wind speeds. As observed in Figure 2.10, the wind speed distribution of Adrar shows that nearly one fifth of wind speeds are 4 m/s or less, while a big proportion of speeds, precisely 62.5% are between 5 and 9 m/s. The rest of wind speeds are above 10 m/s [18].

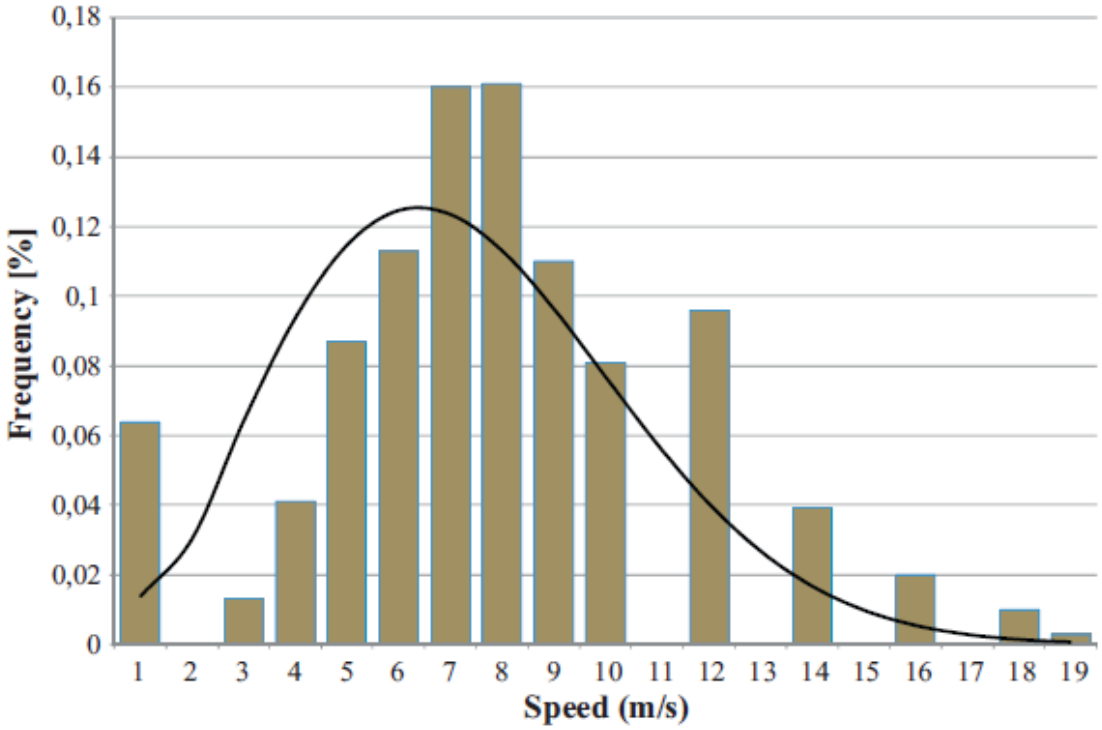

Figure 2.10: Wind speed distribution in Adrar [18]**.**

Based on the published data in the Wind Atlas of Algeria [18], average speeds are the lowest from around 8 pm to 5 am at merely 5 m/s. The maximum speed of almost 6.9 m/s is reached in the morning around 10 am and a medium of 6 m/s is maintained throughout the day.

2.3.3. Climate condition in Adrar

Though it has a traditional system of irrigation the "Foggara", Adrar is considered as an agricultural zone. The region is characterized by a hot and very arid Saharan climate, cold nights in winter, very poor rainfall and seasonal sand storms. July marks the hottest month with a minimum mean temperature of 26.8 °C, and maximum mean temperature of 44.9 °C. On the other hand, the coldest month is January, in which mean minimum and maximum temperatures reach 4.5 °C and 20.3 °C respectively [21]. Table 2.4 shows some important weather parameters based on a study conducted by (R. Dabou e*t al., 2016*) [22].

Table 2.4: Monthly average of daily weather parameters in 2014 [22]**.**

Months	H (kW h/m^2)	T_{max} (°C)	RH (%)
January	4.36	22.67	38
February	5.49	26.06	26
March	6.64	27.98	21
April	7.73	32.72	14
May	7.8	39.76	12
Jun	8.1	42.42	11
July	7.48	47.39	8
August	6.96	45.86	13
September	6.16	43.93	15
October	5.48	37.15	18
November	4.23	27.28	35
December	4.26	20.68	43
Mean Monthly	6.22	34.49	21.16

In addition to low humidity rates (RH), Adrar is also known for having high water potential from underground continental intercalary layer.

2.4. Solar Photovoltaic Systems

A photovoltaic system is defined as a power system that is designed to supply electricity by means of photovoltaics. Several components make up the system, starting from solar panels all the way to cables. The hardware responsible for regulating and controlling the output of a PV system, including inverters, is known by balance of system (BOS). PV systems have a wide range of applications, from very small units to large plants of the order of MWs.

Solar Photovoltaics had a small contribution in power production worldwide. However, a different trend has emerged lately, and a rapid growth is observed in the installation of solar PV systems, both grid-connected and standalone, and it is predicted to continue in the upcoming years. It is expected that solar PV will generate over 26 times as much power in 2035 as was generated in 2010, expanding from 32 TWh to 846 TWh [23]. As is the case in the whole world, photovoltaic systems in Algeria are also increasingly being used in electricity production in the last years, this has been encouraged by the new policies of the Ministry of Energy and Mines with the aim of reducing fossil fuel dependency by exploiting the available renewable sources.

2.4.1. Photovoltaics working principle

The sun's radiation ranges from ultraviolet (200 nm wavelength) to infrared (2.5 μm wavelength). The annual solar energy received by the earth is 1.6 million TWh. About 30% of this energy is reflected and another 45% is re-emitted by heat radiation to space, some of the solar energy is exploited after being converted into different forms [8]. When a semiconductor is struck by a beam of light, it reflects part of it and absorbs another part. This absorption of light is a quantum process in which light imparts enough energy to some electrons and move them to higher energy levels.

If the energy of the photon is greater than the energy gap of the semiconductor (the energy which separates the conduction band from the valence band as shown in Figure 2.11), the electron migrates from the valence band to the conduction band forming an electron-hole pair.

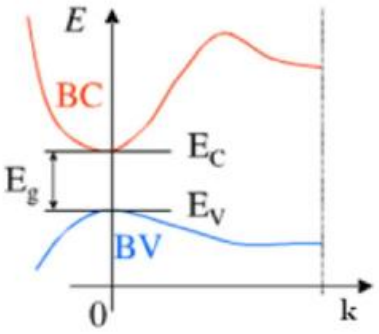

Figure 2.11: Energy gap in a semiconductor [8]**.**

PV cells consist of semiconductor material which allows the transformation of light energy into electrical energy. This is possible by combining an N-doped semiconductor material to another P-doped semiconductor, the most used dopants are Phosphorous and Boron. As mentioned earlier in the photon-semiconductor interaction, the energy produced by the absorption of a photon in a material results in the creation of an electron-hole pair (Figure 2.12). This reaction causes a difference in the distribution of charges thus creating the PV effect; a difference in electric potential.

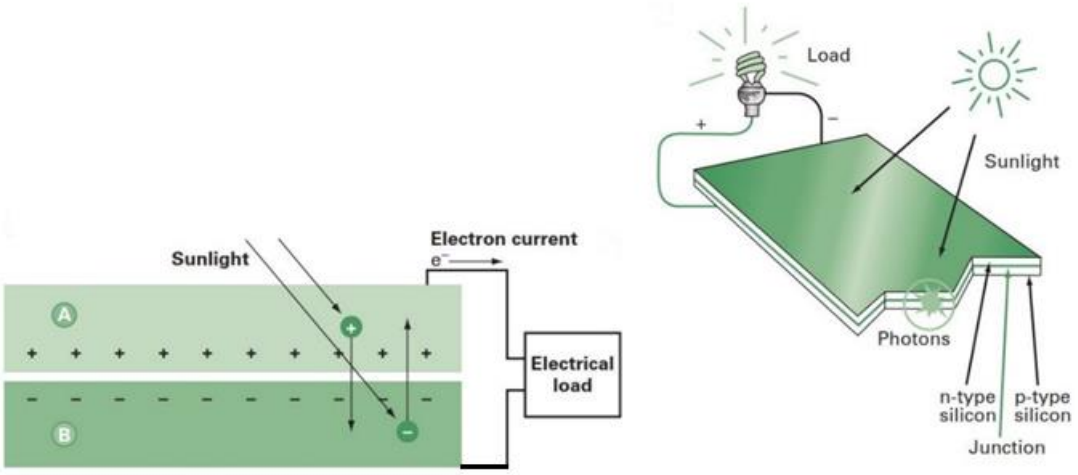

Figure 2.12: PN junction in a PV cell [24]**.**

The combination of the two types of materials creates a PN junction which facilitates the recovery of the resulting charges before they recombine in the material. The presence of the PN junction thus allows a current flow to be maintained at its terminals. The PV cell has a non-linear I-V characteristic as demonstrated in Figure 2.13, This curve sweeps three quadrants out of four [19]. In quadrant two and four, the PV cell acts as a receiver and is prone to destruction by local heating phenomenon (hotspot), which is why a series protection diode is used to prevent this. The normal operation is in quadrant one where the cell acts as a generator producing energy.

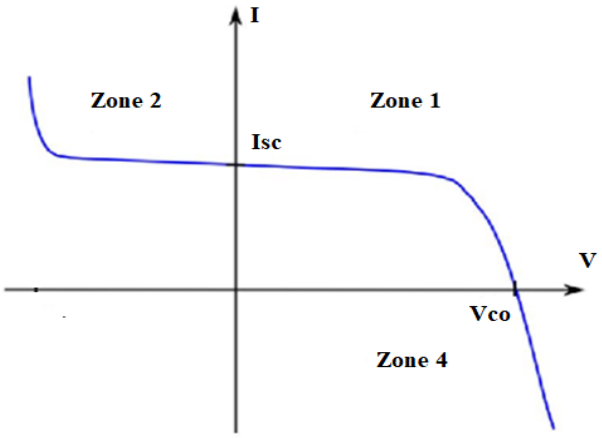

Figure 2.13: PV cell I-V characteristic [25]**.**

2.4.2. Photovoltaic cell technologies

The PV market is largely dominated by crystalline silicon solar cells with a rate of almost 80%, either monocrystalline or polycrystalline. Despite that, many other technologies are already available or under research. For example, thin film solar cells are making their way to the PV market due to the low cost of manufacturing and ease of production. As shown in Figure 2.14, the best efficiency of silicon cells obtained so far is 26.1%, while multi-junction solar cells have a much higher efficiency of 46% at laboratory level. Moreover, Cadmium Telluride (CdTe) and Perovskite PV cells have seen an increase in efficiency, reaching 22.1% and 22.7% respectively [26].

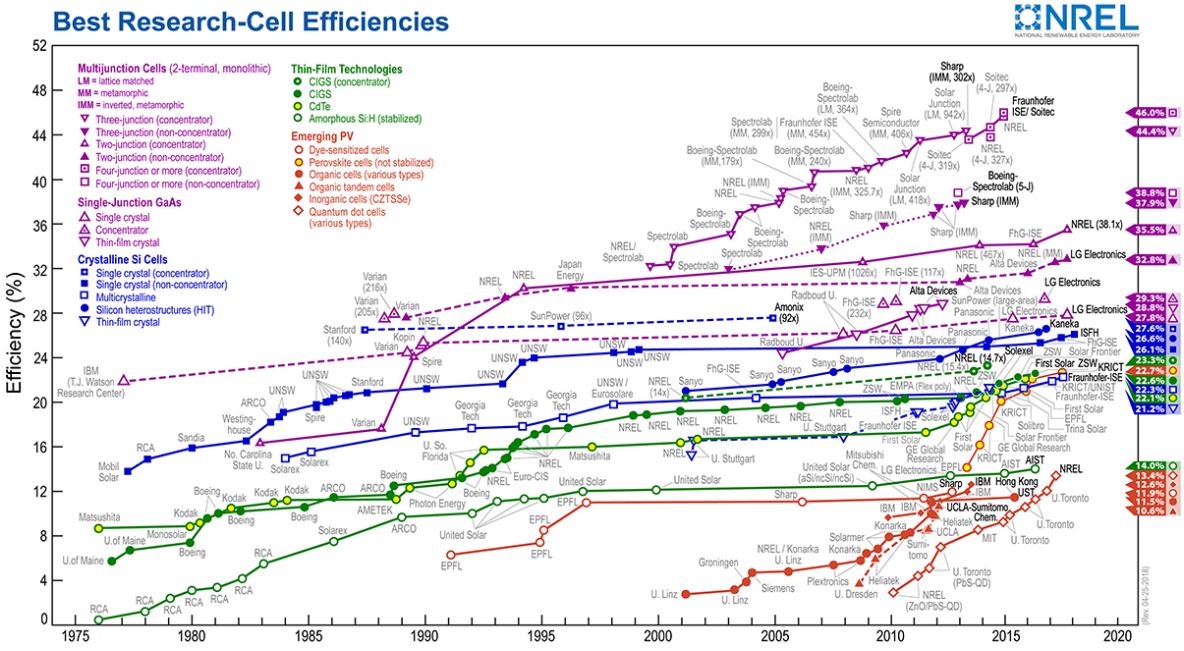

Figure 2.14: Efficiency evolution of PV cell technologies [26]**.**

2.4.2.1. Crystalline silicon-based solar cell

Crystalline silicon was developed in 1953 in the bell lab, its efficiency was about 6% at that time. The availability and low cost of silicon make it a prominent choice of material. In addition, it is characterized by its low coefficient of absorption and low energy band gap. Crystalline silicon is divided into monocrystalline and polycrystalline (see Figure 2.15).

Monocrystalline silicon is the base material used in all electronic equipment today, its cells are characterized by a high purity and obtained by the Czochralski process and zone melting methods, the silicon used is cut from one large crystal. Thus, the internal structure is highly ordered, which allows electrons to

move easily through it. This type of silicon makes it possible to produce high efficiency PV cells (26.1% in laboratory) [8].

Polycrystalline silicon is cheaper since it is of a lower quality, and it is generally obtained by directional or progressive solidification of silicon ingots. The latter contains more impurities (metal impurities, O, C, etc.) and is composed of several grains of sizes ranging from a few millimeters to one centimeter. The efficiency of polycrystalline silicon cells is at 19.8% in the laboratory [8].

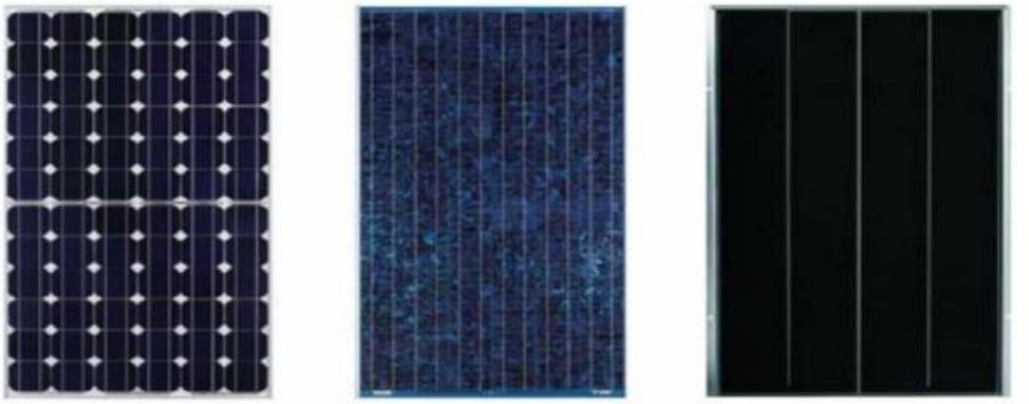

Figure 2.15: Main commercial PV modules [27]**.**

2.4.2.2. Organic solar cells

Organic cells are built from organic materials based on carbon, hydrogen and nitrogen. They are known by third-generation cells and are light, flexible and customizable on the molecular level. They have the advantage of being inexpensive and simple to manufacture on a large scale, they are fit for multiple applications and have less adverse environmental impacts. However, the main disadvantage is the low efficiency (11%) due to the non-separation of charges in addition to the considerably bad aging [28].

2.4.2.3. Thin film solar cells

This kind of cells is known as second generation PV cells. The technology relies on using less material in the manufacturing process of the PV cell (Figure 2.16), since the cost of the material represents up to 30% of the final price of a solar panel.

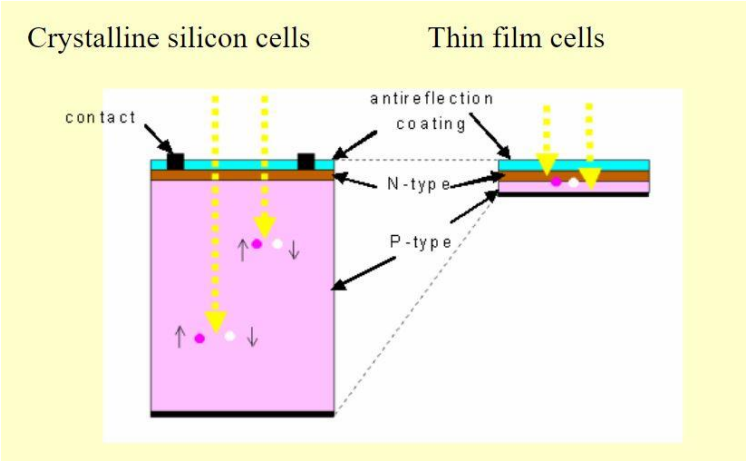

Figure 2.16: Crystalline silicon versus thin film cells [29]**.**

Several materials are used for thin film cells:

- The amorphous silicon.
- The polycrystalline semiconductor CdTe (Cadmium telluride).
- The (Copper-Indium\Gallium-Selenium) alloy noted CIGS in the literature.

Thin film cells have a rather low efficiency due to the multiple interfaces that separate the different layers. These interfaces contain many defects which increases the rate of recombination of the charge carriers resulting in a reduced life span [8].

2.4.2.4 Tandem multi-junction solar cells

As the name suggests, these solar cells have multiple PN junctions of different semiconductor materials as seen in Figure 2.17. The junction multiplicity enables electricity production from different light wavelengths, which means a wider range of wavelengths is absorbed, and thus the conversion efficiency is improved [30].

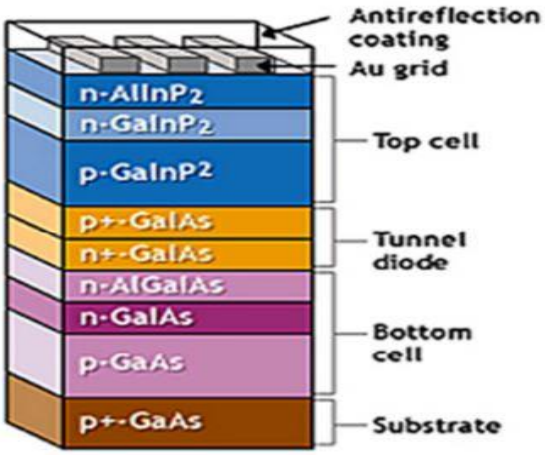

Figure 2.17: Multi-junction cell [30]**.**

Multi-junction cells also have the advantage of being resistant to radiation and mechanical impacts. The output of commercial current multi-junction modules is around 30% for a spectrum AM0 (global solar spectrum). The downside of these cells is the fact that they are still far too expensive for domestic applications. research suggests that using solar concentrators can lower the price since concentration would require less cell area. The maximum efficiency of a concentrator-free triple-junction cell of GaInP/GaAs /Ge is around 32%, the same cell would arrive at an efficiency of 40.7% if equipped with a concentrator [31].

2.4.2.5. Perovskite solar cells

This type of solar cells has a perovskite compound, the most common compound is a hybrid organic-inorganic material like methylammonium lead trihalide. The term "perovskites" itself describes a set of compounds characterized by the formula ABX3, and have the same crystalline structure like calcium titanium oxide (CaTiO3) [32]. Perovskite cells are simple and cheap to manufacture, they have a high absorption coefficient which allows for ultrathin films to absorb all the visible solar spectrum. In addition, the efficiency of perovskite cells has improved from 3.8% in 2009 to 22.7% in 2017, this huge improvement makes it the fastest advancing technology [26]. However. The downside of this technology is that the cells degrade rapidly in moist environments, but researchers demonstrated in [33] the possibility to fix the degradation problem in large scale modules.

2.4.3. PV system components

Grid-connected PV systems inject directly the output energy into the grid and these systems mainly include:

- PV generator: a set of PV modules that convert solar energy into DC energy, the modules can be connected in parallel or in series and sometimes in both ways depending on the desired output.
- Inverter: a device that transforms DC power from the PV modules into 60 or 50 Hz AC power. There are voltage inverters and current inverters, the choice depends on the input source. However, the voltage inverter technology is more mature and widely used in most industrial systems ranging from few Watts to several MWs [8].
- DC-DC converter: these are used to step up or down the DC voltage allowing the choice of solar array voltage to be independent from that of the load.
- Utility Meter: a device responsible for computing how much power is either consumed from or injected to the grid, at night and during the day when the demand exceeds the solar electric power production, the meter spins backwards and vice versa.

Stand-alone systems require additional components:

- Storage device: batteries are commonly used in many types of PV systems to supply power at low sun conditions. In addition, the fluctuating nature of the PV output necessitates the use of batteries and their size and capacity are selected according to the load.
- Charge controller: such device manages the flow of electricity from and to the storage device (batteries). The appropriate charge control algorithm and charging currents need to be matched for the batteries (or other energy storage devices) used in the system. The charge controller aims at protecting the battery from damage and preventing overcharging or excessive discharging.

2.4.4. Configuration and model of PV modules

The PV cell has very similar physics to that of a classical PN junction diode formed by semiconductor material. Interconnected PV cells form a PV module; the connections can be made either in parallel or in series. The general mathematical model for the solar cell has been studied over the past three decades, and the equivalent electric circuit consists of a photocurrent, a diode, parallel and series resistors as shown in the Figure 2.18 below [34].

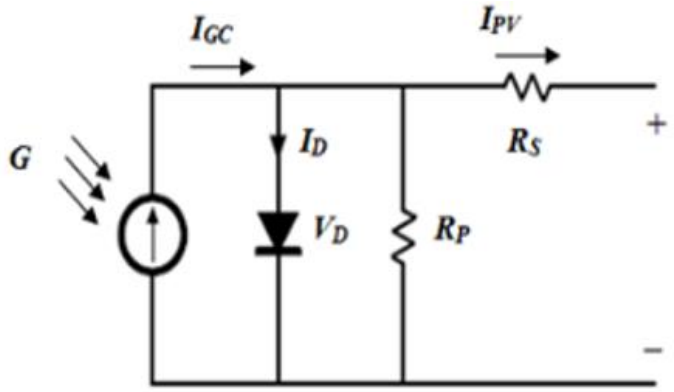

Figure 2.18: PV cell equivallent circuit [34]**.**

Based on the PV cell circuit and Kirchhoff's circuit laws, the photovoltaic current is determined by the following equation [34]:

$$I_{pv} = I_{gc} - I_0 \left[exp^{\left(\frac{e\, v_d}{K\, F\, T_c}\right)} - 1 \right] - \frac{v_d}{R_p} \qquad (2.1)$$

Where:

- I_{gc} represents the light generated current.
- I_0 is the dark saturation current which depends on the temperature of the cell.
- *e* is the electric charge = 1.6 x 10^{-19} Coulombs.
- *K* is the Boltzmann's constant = 1.38 x 10^{-23} J/K.
- *F* is the cell idealizing factor.
- T_c is the cell's absolute temperature.
- v_d is the diode voltage.
- R_p is the parallel resistance.

The photocurrent (I_{gc}) is governed by the solar irradiation and cell temperature through the following equation [20]:

$$I_{gc} = [\mu_{sc}(T_c - T_r) + I_{sc}]G \qquad (2.2)$$

Where:

- μ_{sc} is the temperature coefficient of the cell's short circuit current.
- T_r is the cell's reference temperature.
- I_{sc} is the cell's short circuit current under STC.
- *G* is the solar irradiation in kW/m².

The saturation current (I_o) varies with the cell temperature as well, this is described by equations (2.3) and (2.4):

$$I_0 = I_{0a}\left(\frac{T_c}{T_r}\right)^3 \; exp\left[\frac{e\, v_g}{K\, F}\left(\frac{1}{T_r}-\frac{1}{T_c}\right)\right] \tag{2.3}$$

$$I_{0a} = \frac{I_{sc}}{exp^{\left(\frac{e\, v_{oc}}{K\, F\, T_c}\right)}} \tag{2.4}$$

Where

- I_{0a} is the cell's reverse saturation current at reference solar radiation and temperature.
- v_g is the band-gap energy of the semiconductor used in the cell.
- v_{oc} is the cells open circuit voltage.

The behavior of PV cells depends on the type of connection. In a series group, the cells are crossed by the same current and the resulting characteristic is obtained by adding the voltages for a given current. The properties of the parallel grouping of the cells are dual to those of the series grouping. Thus, in a group of cells connected in parallel, the cells are subject to the same voltage and the resulting characteristic of the group is obtained by adding the currents for a given voltage. The comparison of the resulting I-V characteristics of parallel and series sets of identical PV cells is presented in Figure 2.19.

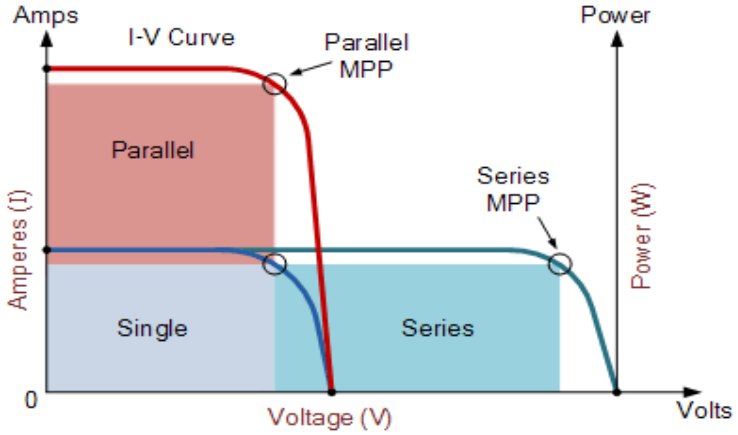

Figure 2.19: I-V characteristic of parallel vs series connection of PV cells [35].

In summary, to plot the equivalent characteristic of a group of PV cells:

- In parallel, it is necessary to be placed at a given voltage and summing the currents of each cell. This operation must be repeated for all voltages between zero volts and V_{oc}.
- In series, it is necessary this time to be placed at a given current and sum the voltages of the different cells to this current.

2.4.4.1. Some relevant terms

Each PV module has its own characteristics; these are briefly presented in the following subsections.

A) Open circuit voltage

The open-circuit voltage (V_{oc}) defines the maximum voltage that a solar cell can provide, this voltage is at zero current. V_{oc} is attributed to the forward bias on the solar cell due to its junction bias with the light-generated current. V_{oc} is determined by nullifying the net current and it is given by the following equations:

$$V_{oc} = \frac{nkt}{q} \ln\left(\frac{I_{gc}}{I_0} + 1\right) \tag{2.5}$$

$$V_{oc} = \frac{kT}{q} \ln\left[\frac{(N_A + \Delta n)\Delta n}{n_i^2}\right] \tag{2.6}$$

The second equation is based on the carrier concentration where:

- kT/q represents the thermal voltage.
- N_A is the doping concentration.
- Δn defines the concentration of excess carrier.
- n_i is the concentration of intrinsic carrier.

B) Short circuit current

The short-circuit current (I_{sc}) is the largest current that can be drawn from the solar cell and is obtained when the solar cell is short circuited, i.e., at zero voltage. It is the outcome of the generation and the collection of carriers generated by light. The short-circuit current depends on the generation rate G and the diffusion lengths L_n and L_p as indicated by the following equation:

$$I_{sc} = q.G.(L_n + L_p) \tag{2.7}$$

C) Maximum output power

The power produced is the product of the current and the voltage (P=I.V), it is equal to zero at I_{sc} and V_{oc}. At maximum output power, the voltage and current are denoted as V_{mp} and I_{mp} respectively.

D) The fill factor

The fill factor serves as a measure of the junction quality and series resistance of a solar cell, the closer it is to unity the better is the quality of the cell. The fill factor is defined by:

$$FF = \frac{I_{mp}V_{mp}}{V_{oc}I_{sc}} \tag{2.8}$$

For example, silicon cells have a FF of 0.88.

E) Efficiency

Efficiency is determined as the ratio of the power output to the power input. Solar cells usually operate at maximum power which means that the power output can be taken as the maximum power:

$$\eta = \frac{P_{out}}{P_{in}} \Rightarrow \eta_{MAX} = \frac{P_{MAX}}{P_{in}} \tag{2.9}$$

The input power is the product of irradiance (W/m^2) with the area of the solar cell (m^2)

2.4.4.2. Installation of PV panels

When connecting multiple solar panels, there are three options: parallel, series, or combining the two. In parallel circuits there are multiple paths for the current to follow. That means if an item in the circuit breaks down, the current will keep flowing in the other paths. This type of circuit is used for most household electrical wiring. Figure 2.20 illustrates parallel and series wiring of PV modules.

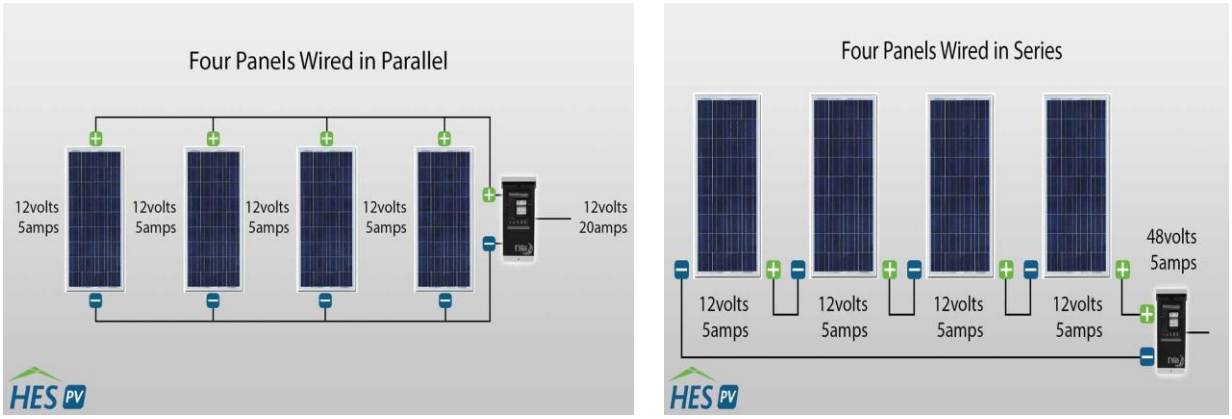

Figure 2.20: Parallel and series wiring of PV panels [36]**.**

Much like the connection of cells discussed in the previous section, when wiring solar panels in parallel, the current is additive, but the voltage remains unchanged. In series circuits there exists only one path for the current to flow. Therefore, the current flows through all the loads, so breaking the circuit at any point stops the entire system from operating.

2.4.4.3. Performance of PV modules

The performance of PV modules depends on many factors, and based on the nature of the module's components, some parameters have a direct and more important impact on the output of the PV module. The two most significant parameters are the cell's temperature and the irradiation with the latter being proportional to the output current.

A) Effect of irradiance and temperature

The characteristics of the cell are directly influenced by both solar irradiation (G) and ambient temperature (T). The irradiation G (W/m^2) affects directly the short circuit current (I_{sc}) of the PV cell (see Figure 2.21), however it has little to no impact on the open circuit voltage (V_{oc}). Thus, output power is almost linearly proportional to incident solar irradiation. On the other hand, as the temperature increases the open circuit voltage of the photovoltaic cell decreases and the short circuit current slightly rises. This is to say that cold weather is more favorable for solar cells performance than hot weather. With panels being rated at 25˚C, which is quite different from real situations, each degree rise in temperature above 25˚C results in about a 0.4% to 0.5% drop in output for crystalline cells [37]. During the summer season, the panel temperature can easily reach 70˚C or more meaning that the output will be 25% less compared to the 25˚C rating.

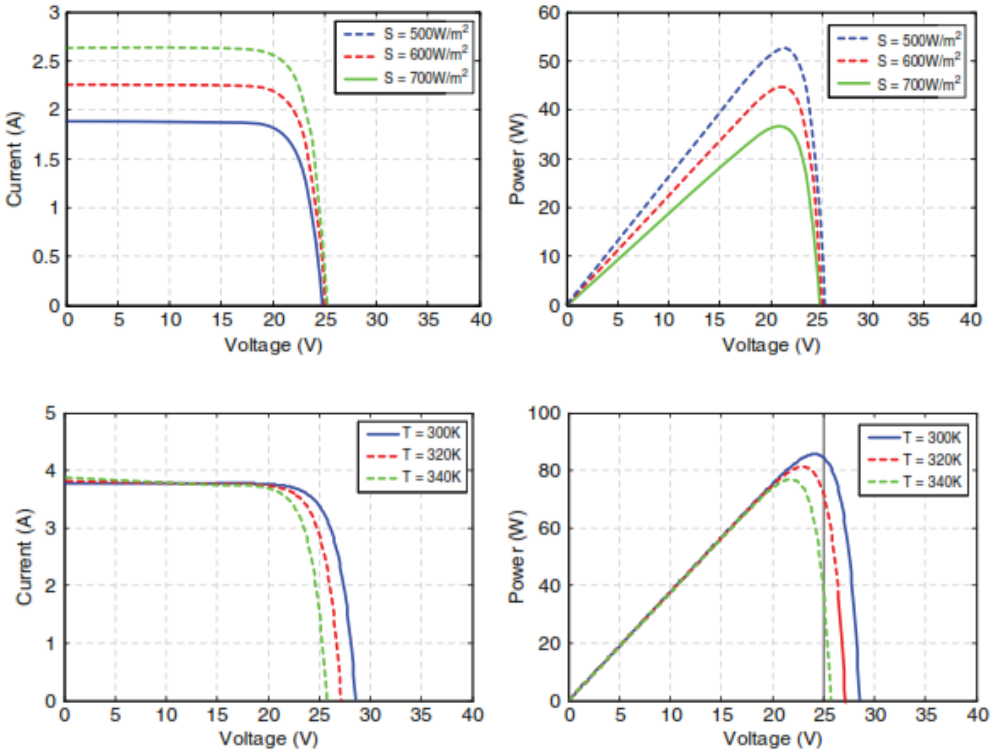

Figure 2.21 The impact of irradiation and temperature on I-V curve and P-V curve [37]**.**

B) Effect of humidity

The efficiency of the PV module is affected by the relative humidity, the latter has an impact on the current, voltage and thus the power output. Based on previous studies done in [37], when the relative humidity drops, the power and efficiency increase. Furthermore, monocrystalline panels, compared to other technologies, deliver the highest efficiency in situations where relative humidity decreases.

C) Effect of dust accumulation

As illustrated in [38], the presence of dust on the surface of panels has a noticeable impact on their output. This effect on the collectors depends on many factors, namely:

- The kind of material used in the panels and the size of dust particles.
- The orientation of the panels with respect to wind direction.
- The speed of wind.
- The distribution of dust on the surface of the panel (g/m^2).
- The tilt angle of the collector.

The transmittance of the panel's glass depends heavily on the density of dust deposition which is governed by the tilt angle and the orientation of the plate with regard to the direction of dominant wind. Some experiments were conducted in [38] to observe how PV modules behave in the presence of dust. It was found that dust accumulation over photovoltaic collectors reduces the short circuit current because the incident solar irradiation striking the cell is decreased, hence the power output of the PV module drops causing a reduction in the overall efficiency of the system.

2.4.5. Maximum power point tracking

The output of a PV array is nonlinear, it varies with the irradiation level, the ambient temperature and the load. For the same irradiation and temperature, a PV array can work with different output voltages, but it only generates the maximum power at a specific voltage. This voltage corresponds to the highest point of the P-V curve as shown in Figure 2.22 and it is called the maximum power point (MPP). Hence, continuous adjusting is needed to keep the operating point of the PV array around the MPP. Such process is called MPPT and can be done by adjusting the duty cycle of the DC-DC converter (boost, buck-boost, etc.) to vary artificially the load and extract the maximum power out of the PV panel [39]. Over the past decades many MPPT algorithms have been developed to find the maximum power point. These techniques differ in many aspects such as required sensors, complexity, cost, range of effectiveness, convergence speed, correct tracking, etc. However, they all require accurate current and voltage measurements and employ microcontrollers and analogue to digital converters to acquire current and voltage data and compute power, its derivative and the duty cycle.

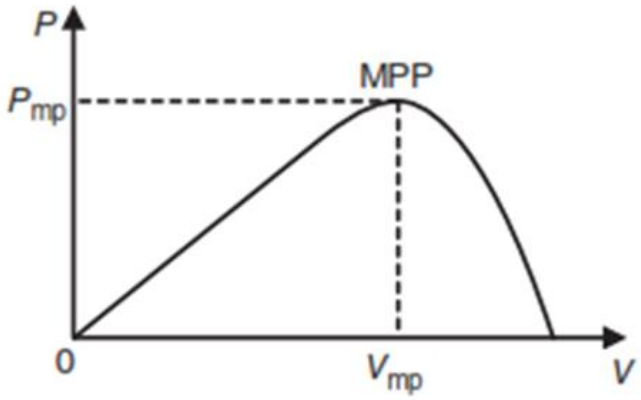

Figure 2.22: P-V characteristic curve of a PV array [39]**.**

2.4.5.1. Hill climbing/perturb and observe

The perturb and observe method is the most common algorithm used in maximum power point tracking (MPPT) since it is easy to implement. The principle of operation in such algorithms is the introduction of a perturbation in the system, which will cause the power of the module to change. If the perturbation induced increases the power of the module, then the perturbation is continued. After reaching the peak power, a decrease in the output power takes place in the following instant, and hence, the perturbation is reversed. Once the transition is done, the steady state is reached, and the algorithm oscillates around the peak point. The perturb and observe algorithm, shown below in Figure 2.23, is designed to set the reference voltage of the module according to its peak voltage. Furthermore, it is important to keep the power variation small which is why the perturbation must be kept very small as well. The drawback of this method is that the maximum power tracking is slow in situations with fast varying atmospheric conditions.

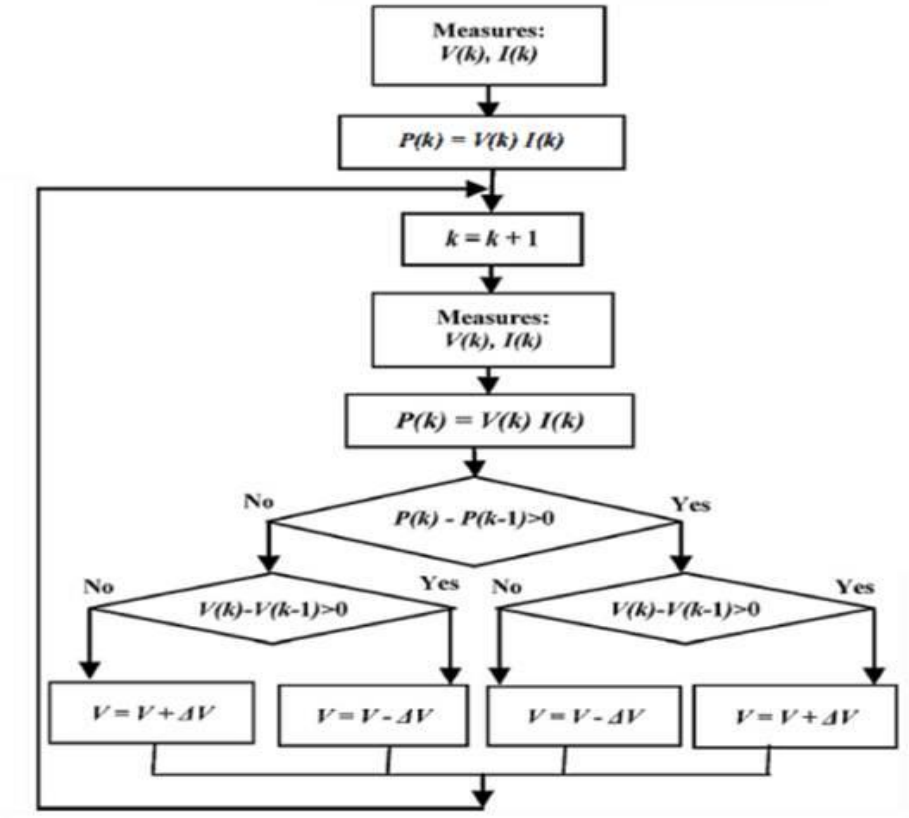

Figure 2.23: Flowchart of the P&O algorithm [40]**.**

2.4.5.2. Incremental conductance

The design of the incremental conductance MPPT tracker was based on the observation of the P-V characteristic curve. In 1993, the algorithm was developed in the hope of overcoming the drawbacks of the P&O algorithm by improving the tracking time and producing more energy in environments with variable irradiations [40]. The IC algorithm uses the relation between dI/dV and I/V shown by Figure 2.24. A negative dP/dV implies that the MPP lies on the right side of the recent position and the opposite is true as well. Unlike the P&O method, the IC method tracks the MPP well under rapidly changing atmospheric conditions, but it requires a complex control circuit [41].

The IC method is governed by the following equations:

$$\frac{\mathrm{dP}}{\mathrm{dV}} = \frac{\mathrm{d(V.I)}}{\mathrm{dV}} = \mathrm{I}\frac{\mathrm{dV}}{\mathrm{dV}} + \mathrm{V}\frac{\mathrm{dI}}{\mathrm{dV}} \tag{2.10}$$

$$= \mathrm{I} + \mathrm{V}\frac{\mathrm{dI}}{\mathrm{dV}}$$

The MPP is reached when dP/dV=0 and:

$$\frac{dI}{dV} = -\frac{I}{V}$$

$$\frac{dP}{dV} > 0 \rightarrow V_p < V_{mpp}$$

$$\frac{dP}{dV} = 0 \rightarrow V_p = V_{mpp}$$

$$\frac{dP}{dV} < 0 \rightarrow V_p > V_{mpp}$$

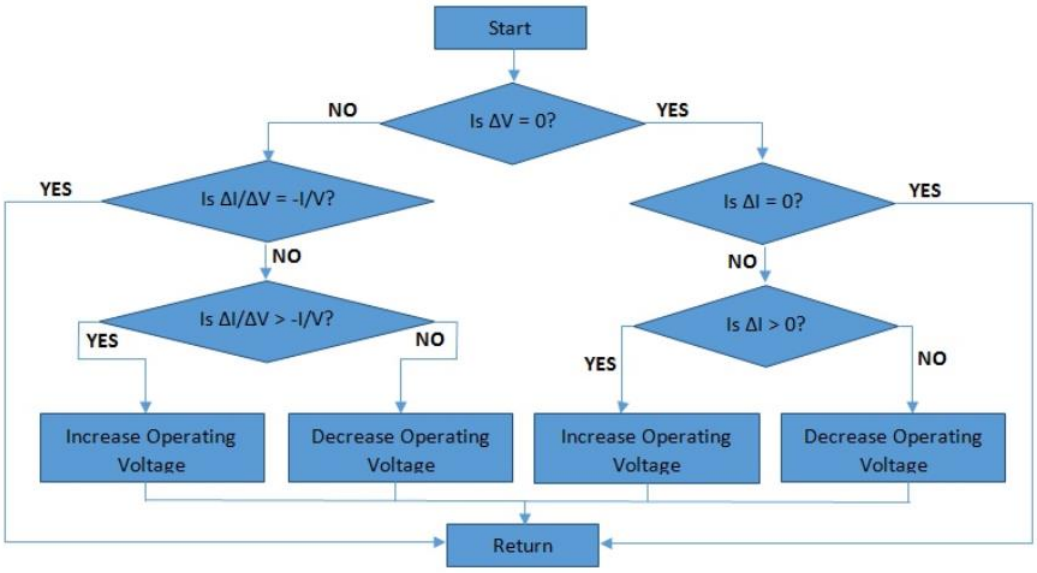

Figure 2.24: Flowchart of the incremental conductance [41]**.**

2.4.5.3. Open-circuit voltage method

The maximum power voltage of the PV array is linearly dependent on the open-circuit voltage for variable irradiation and temperature, this dependence is given by the following equation [42]:

$$V_{mpp} = m_v \times V_{oc} \qquad (2.11)$$

Where v_{mpp} is the maximum power point voltage, v_{oc} is the open circuit voltage of the PV array and m_v represents the voltage factor with a value ranging from 0.7 to 0.8. Figure 2.25 gives the block diagram of the voltage based MPPT.

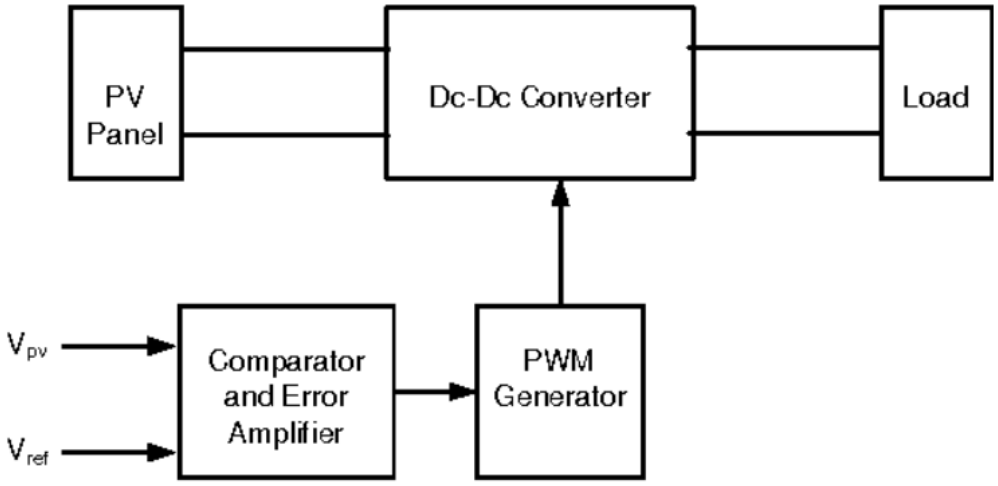

Figure 2.25: Diagram of voltage-based MPPT [42]**.**

To keep the PV panel operational at the maximum power point, a comparison is needed between the actual PV array voltage v_{pv} and the reference voltage v_{ref} which delineates v_{mpp}. The comparison gives an error signal which is then processed to obtain $v_{pv} = v_{ref}$. To get the open circuit voltage, the panel is disconnected from the load momentarily. The fraction of the open-circuit voltage corresponding to v_{mpp} is measured and kept in a hold circuit to function as v_{ref} for the control loop. It has been shown that the efficiency of this method is comparable to the P&O and IC methods under normal illumination conditions, this method proved to be the simplest and most cost effective [42].

2.4.5.4. Short-circuit current method

In this method, the PV current is compared with a constant reference current that corresponds to I_{mpp}. The resulting error signal is sent to simple controllers to be eliminated with integral action in the steady state [43]. Much like the open circuit voltage method, the maximum power point current is proportional to the short circuit current:

$$I_{mpp} = m_i \times I_{sc} \tag{2.12}$$

Where the factor m_i is always less than 1.

Previous studies showed that this method can be applied under different weather conditions. However, the main drawback of the short-circuit current method is that the load must be disconnected from the PV generator to measure the short-circuit current (I_{sc}) resulting in energy waste. In addition, the measurement of the (I_{sc}) during the operation of the system also increases the complexity of the circuit.

2.4.6. Types of PV systems

Photovoltaic systems are mainly classified into two types, and this is done based on their component configurations, the way they function and whether and how they are connected to other power sources or electrical loads. Although PV systems provide DC power, they can be tweaked to deliver AC power too. They can be interconnected with or independent from the utility grid and can be equipped with storage systems and work with other energy sources.

2.4.6.1. Stand-alone PV systems

Stand-Alone PV Systems consist of several individual photovoltaic modules with power outputs ranging from 50 to 300+ watts each. A single array combines all the PV modules to provide the desired power output. Stand-alone PV systems are used as residential systems for supplying buildings with energy or as solar home

systems. Such systems supply a single home with enough power to meet the needs for lighting and small home appliances. Other applications of stand-alone systems include water pumping as shown in Figure 2.26. They automatically produce electrical power to supply the load and charge a battery-bank during the day so that it can be used at night when there is no sunlight. These systems are ideal for remote and isolated rural areas that are not covered by the electric network, and where other energy sources are not available or not practical to provide power for the variety of domestic applications [44].

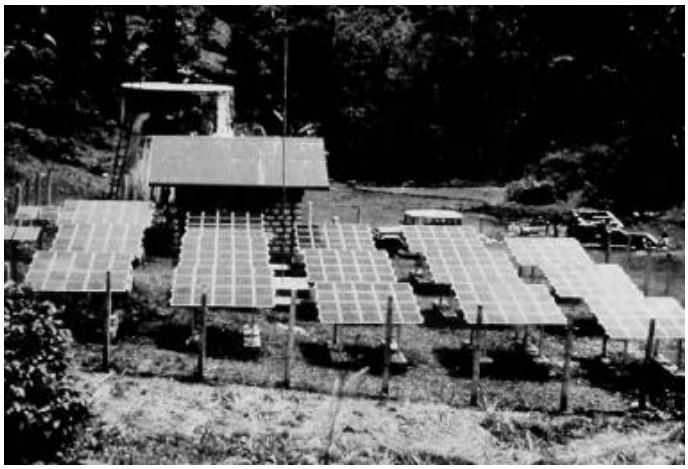

Figure 2.26: Stand-alone water pumping PV system [44]**.**

2.4.6.2. Grid-connected PV systems

This type of systems works in parallel with the utility grid, and the main component in such systems is the power conditioning unit (PCU), specifically the grid tied inverter (GTI). The GTI converts the DC power generated by the PV array into reliable AC power and synchronizes the output voltage with the grid voltage. Bi-directional interfaces are mandatory for the AC power to flow in two directions and back-feed the grid whenever the production tops the load demand, a significant drop in grid voltage or a grid disconnection result is a complete shutdown of the GTI for protection matters. Grid-connected PV systems are differentiated into decentralized and central systems:

A) Decentralized grid-connected PV systems

Decentralized grid-connected PV systems are characterized by a small power range and are often mounted on the roofs of buildings (rooftop or flat-roof installation) or integrated into building facades. Energy storage is not required in this kind of systems. Figure 2.27 shows the power output of a roof top grid-connected system installed at the University of Tlemcen, the system combines three ALPV panels and uses AP systems GTI.

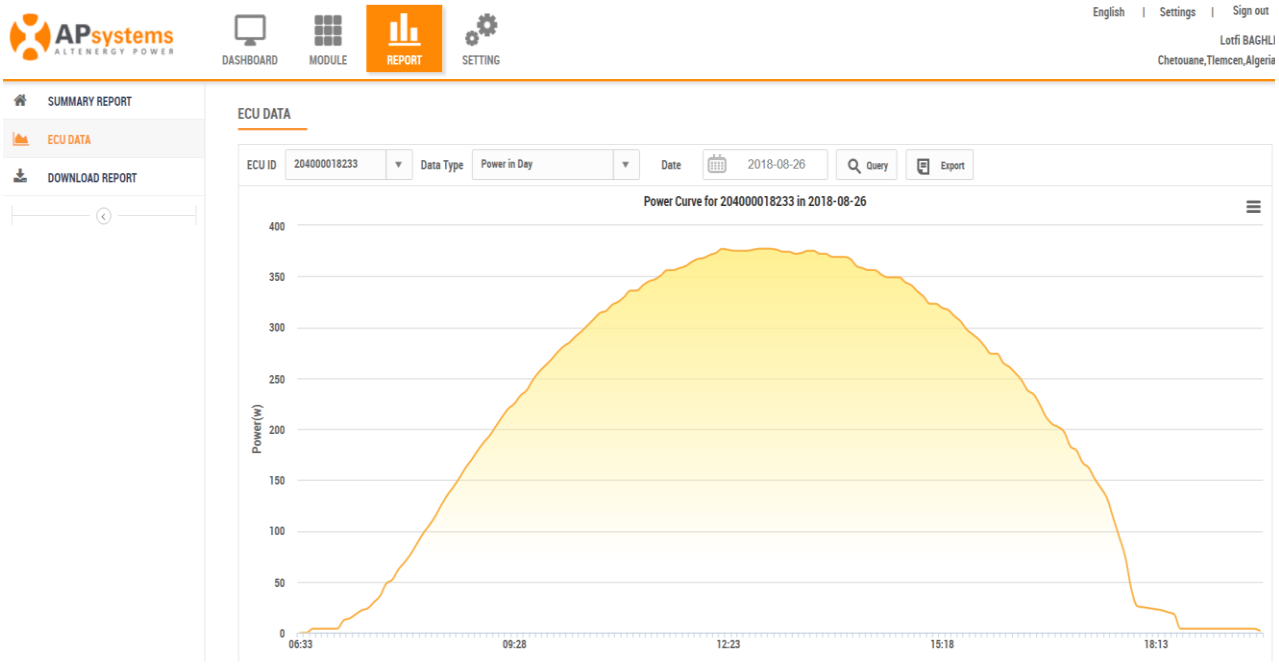

Figure 2.27: Power output of a decentralized grid-connected PV system

B) Centralized grid-connected PV systems

Central grid-connected PV systems are designed to generate large scale power, up to the MW range. Such photovoltaic power stations can feed power directly into the medium or high voltage grid. These systems are usually set up on unused land or installed on the flat roofs of very large buildings. Figure 2.28 shows a schematic diagram of a PV system connected to a three-phase network. This pattern may vary from country to country due to different national regulations and particularly safety and protection circuits.

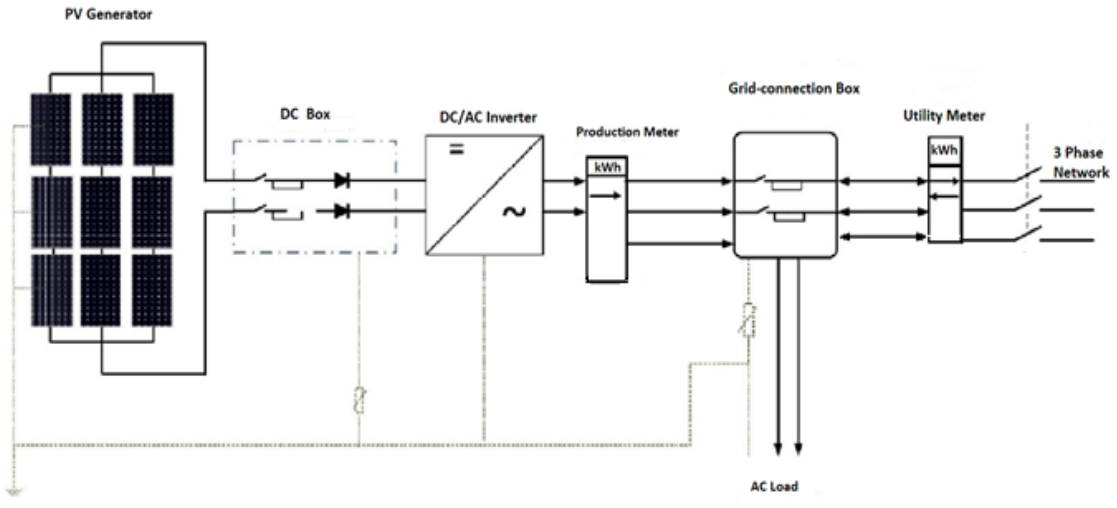

Figure 2.28: Diagram of a grid-connected PV system [8]**.**

The PV modules generate DC current, whose intensity depends on the level of irradiation. It is then converted to AC power by the inverter and used to supply AC loads and the surplus is injected into the power grid. During the night when there is no power generation, the load demand is provided by the utility. In stand-alone systems, the batteries play the role of the utility grid and supply the load acting as a reservoir of energy.

Grid-tied PV systems can be classified according to their size as the following [8]:

1. Small power: from 1 to 10 kW peak, typical applications are on the roofs of private homes, school buildings, car parks, etc.
2. Average power: from 10 to a few hundred kW peak, this kind of systems are found in the so-called building integrated PV (BIPV), roof systems or facades. They can operate at higher voltages than smaller systems.
3. Large power: from 500 kW to the MW range, usually centralized systems that are managed by electricity companies.

2.4.7. Effect of PV systems on the grid and other problems

The use of PV installations has advantages in addition to energy generation. According to the International Energy Agency, these advantages are diversified and cover electrical, architectural, socio-economic and environmental aspects. However, grid connected systems in particular have some negative effects on the grid, which will be revealed in the following paragraphs.

2.4.7.1. The imbalance between phases

In residential areas, the installed inverters are normally single-phase low power inverters. Sometimes the distribution of the PV output power in a low-voltage three-phase electric network is not done correctly between the three phases. Consequently, a phenomenon of low voltage network imbalance may occur.

2.4.7.2. Temporary overvoltage

A study in Spain [45] reports that surges have destroyed electrical equipment such as meters. Such incidents occur when a power blackout causes the isolation of the inverter from the load, this results in an overvoltage exceeding the nominal voltage by 200%. Simulations carried out as part of the Esprit project [46] have shown that during the power outage, the higher the PV output relative to the consumption, the higher the overvoltage.

2.4.7.3. Elevation and local fluctuation of the voltage level

In a distribution network, the linear resistance is greater than the linear reactance (R >> X), thus the active power injected by a PV system into the grid plays an important role in the variation of the voltage. The higher the installed PV power, the higher the voltage at the connection point. Moreover, the variable nature of irradiation causes the fluctuation of the PV power, this implies a fluctuation of the local voltage.

2.4.7.4. Current harmonics

According to the studies done in [46] and [47], multiplying inverters in the network will increase the harmonics if the inverters are of the same type while using different inverters tend to attenuate the harmonics. The new inverter technologies are working on mitigating the current harmonic problems.

2.5. Wind Energy Systems

The potential of wind energy in the world is substantial, turning wind power into a major source of renewable energy that is growing rapidly. Over the past decade, Statistics in the U.S and Europe showed a yearly increase in wind power capacity of over 20%. It is predicted that the share of wind-generated power will exceed 20% within the next twenty years, as the generation capacity has already reached 487 GW in 2016 and it is expected to surpass 760 GW by 2020 [48].

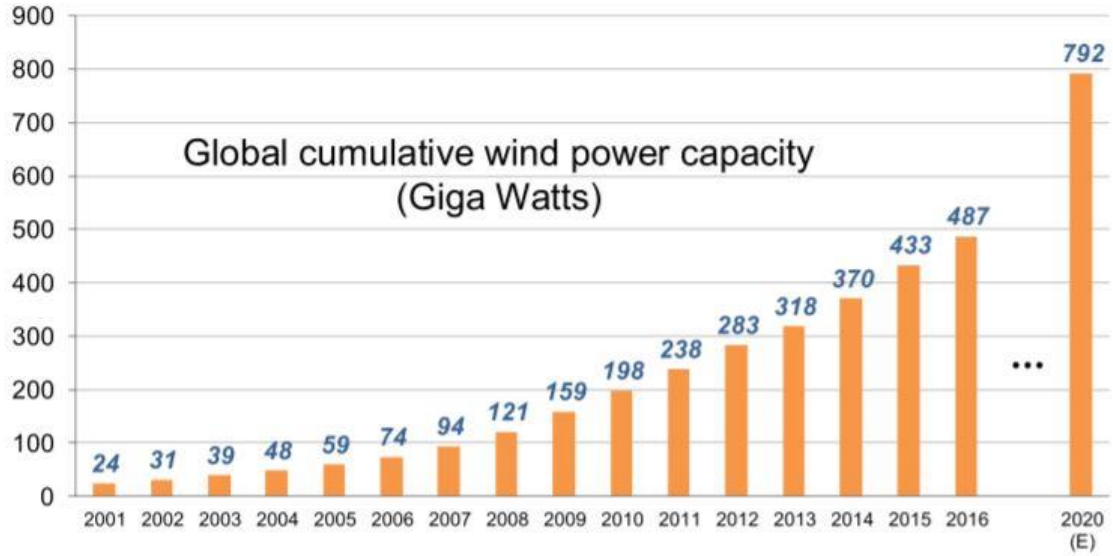

Figure 2.29: Global cumulative wind power capacity from 2001 to 2020 [48]**.**

The technology of wind energy is also advancing, and nowadays large wind turbines are widely installed all over the world with capacities of up to 8 MW. Onshore and offshore wind farms combining several wind turbines are directly connected to power transmission grids, such farms produce huge amounts of power at the scale of hundreds of megawatts. Thus, the dramatically increasing penetration of wind energy systems into the grid calls for advanced power electronics to facilitate their integration into the grid and reduce their impact on the grid system.

2.5.1. Working principle of wind energy

Wind results from expansion and convection of air as solar radiation is absorbed on earth. On a global scale, these thermal effects combine with dynamic effects from Earth's rotation to produce prevailing wind patterns. The amount of energy that can be extracted from wind is proportional to its speed, thus the choice of windy sites is important before installing wind turbines.

2.5.1.1. The Weibull distribution law

Wind is characterized by a temporal variability; this variability is important when it comes to describing a given site in terms of wind speed and frequency distribution. The Weibull distribution is the most famous method for evaluating wind energy. Although there are other statistical models such as the Lognormal and the inverse Weibull distribution [1], the Weibull function is still the most recommended because of its adequate representation of measured data. The Weibull function is given by [1]:

$$f(v) = \left(\frac{k}{c}\right)\left(\frac{v}{c}\right)^{k-1} exp\left(-\left(\frac{v}{c}\right)^{k}\right) \quad (2.13)$$

Where:

- $f(v)$ is the frequency of occurrence of velocity v.
- k is the dimensionless shape parameter.
- And c (m/s) is the scaling parameter.

In order to obtain the Weibull parameters to analyze wind energy, several methods were developed including the graphical, the empirical and the maximum likelihood methods. The most precise one is the maximum likelihood. Thus, the shape parameter (k) and the scale parameter (c) can be computed by the following equations [49]:

$$k = N\left[\frac{\sum_{i=1}^{N} v_i^k \ln(v_i)}{\sum^N v^k} - \sum_{i=1}^{N} \ln(v_i)\right]^{-1} \quad (2.14)$$

$$c = \left[\frac{1}{N}\sum_{i=1}^{N} v_i^k\right]^{\frac{1}{k}} \quad (2.15)$$

After iterative calculations of (k) in equation (2.14), it is then used in equation (2.15) to compute the scale parameter. The concentration of wind around a constant value is determined by the slimness of the distribution, and the scale factor (c) indicates if the chosen site is windy [1]. Furthermore, annual and seasonal average wind speed is estimated using hourly or three-hourly wind speed data and through the following formula:

$$\bar{v} = \int_0^{\infty} v\, f(v) dv \quad (2.16)$$

The variance is calculated by:

$$\sigma^2 = \int_0^{\infty} (v - \bar{v})^2 f(v) dv \quad (2.17)$$

With σ being the standard deviation. Based on equation (2.16), calculating the average speed requires the use of weibull parameters through the gamma function:

$$\langle v \rangle = c\,\Gamma\left(1+\frac{1}{k}\right) \tag{2.18}$$

Where Γ represents the gamma function with tabulated values.

2.5.1.2. Wind turbines

A wind turbine is a machine which converts wind power into electricity and it consists principally of a rotor, an electric generator and a gearbox. Figure 2.30 shows all the components of a HAWT (horizontal axis wind turbine).

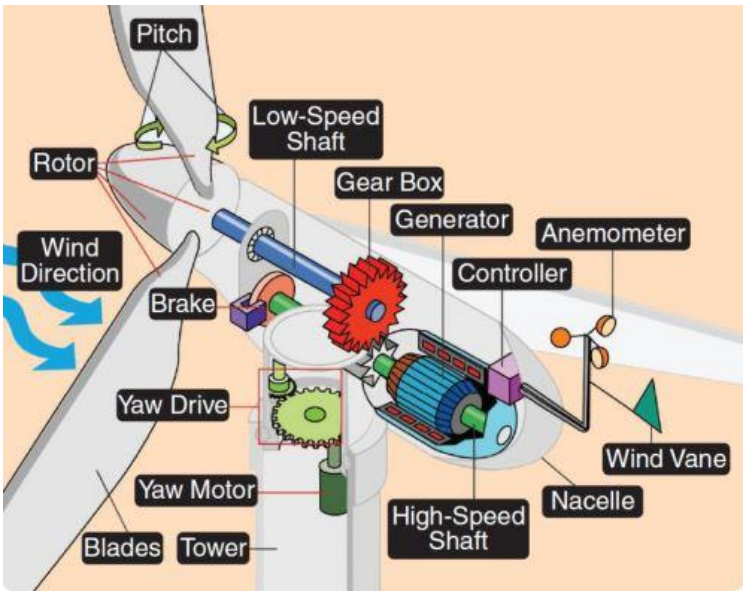

Figure 2.30: Wind turbine construction and components [50]**.**

The energy conversion in current wind turbines is done in two processes, the rotor first extracts the kinetic energy of wind by means of friction between the air and its blades. With the help of a shaft, the rotor converts the kinetic energy into mechanical torque, the generator then converts the mechanical energy into electricity. Although this working principle sounds rather straightforward, wind turbines are complex systems and require knowledge of aerodynamics, mechanical, civil, electrical and control engineering.

Given the working principle of wind turbines, the power generated is inherently dependent on the wind speed as shown by Figure 2.31. The power extracted from the wind can be calculated by the given equation [51]:

$$P_w = 0.5\ \rho\ \pi\ R^2 v^3\ C_p \qquad (2.19)$$

Where:

- P_w = extracted power from the wind.
- ρ = air density, (approximately 1.225 kg/m^3 at 20 °C at sea level).
- R = blade radius (it varies between 40-60 m).
- v = wind velocity (m/s) (velocity can be controlled between 3 to 30 m/s).
- C_p = the power coefficient which is a function of the tip-speed-ratio (λ) and the blade pitch angle (ß).

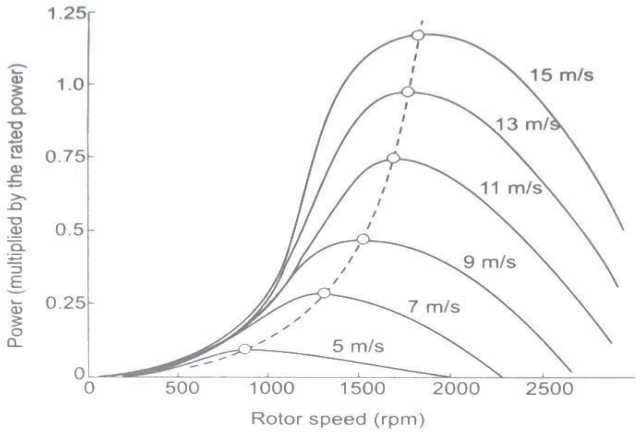

Figure 2.31: Power/Speed characteristic of a wind turbine [52]**.**

2.5.2. Wind turbine characteristics

Wind turbines are characterized by many parameters, these parameters affect their output and performance and are usually specific to different types of turbines, they are reviewed briefly in the next subsections.

2.5.2.1. Solidity

The solidity concerns the turbine's rotor, it is the ratio of the area of the blade to that of the intercepted wind, with the area of the blade being the surface met by the wind. For instance, the Savonius rotor shown in Figure 2.35 has a solidity of one, since the wind sees no free passage through it. On the other hand, the solidity of high-speed horizontal axis machines lies between 0.01 and 0.1. In general, solidity is proportionally related to torque and inversely related to speed. This is to say that high solidity is suitable for water pumping since it implies high torque and low speed, while low solidity is appropriate for electricity generation offering high speed and low torque [52].

2.5.2.2. Tip speed ratio

The tip-speed-ratio (TSR) defines the ratio between the speed of wind (V) and the tangential speed of the blade's tip and it is given by this formula:

$$\lambda = \frac{2\pi RN}{v_\infty} \tag{2.20}$$

Where:

- λ is the TSR (non-dimensional).
- R (m) represents the radius of the swept area.
- N (rps) is the rotational speed.
- v_∞(m/s) is the wind speed free from rotor interruption.

Based on the previous section, it can be said that low-solidity rotors have, in general, high TSRs and the opposite holds true.

2.5.2.3. Power coefficient

The power coefficient introduced earlier in section 2.5.1.2 and given by equation (2.21) is different from power efficiency, since it includes the losses due to mechanical transmission, electrical generation, etc. For HAWTs, the maximum power coefficient is known as the Betz limit (59.3%) [24]. Figure 2.32 shows different curves for different types of wind turbines, the three-bladed rotor offers the best performance while maintaining a reasonable TSR. Generally, the power coefficient increases with the TSR until reaching a maximum for a specific TSR, then it starts decreasing. This relation between the two depends on aerodynamic properties, namely the number of blades.

$$C_p = \frac{Power\ output\ of\ wind\ turbine}{Power\ contained\ in\ the\ wind} \tag{2.21}$$

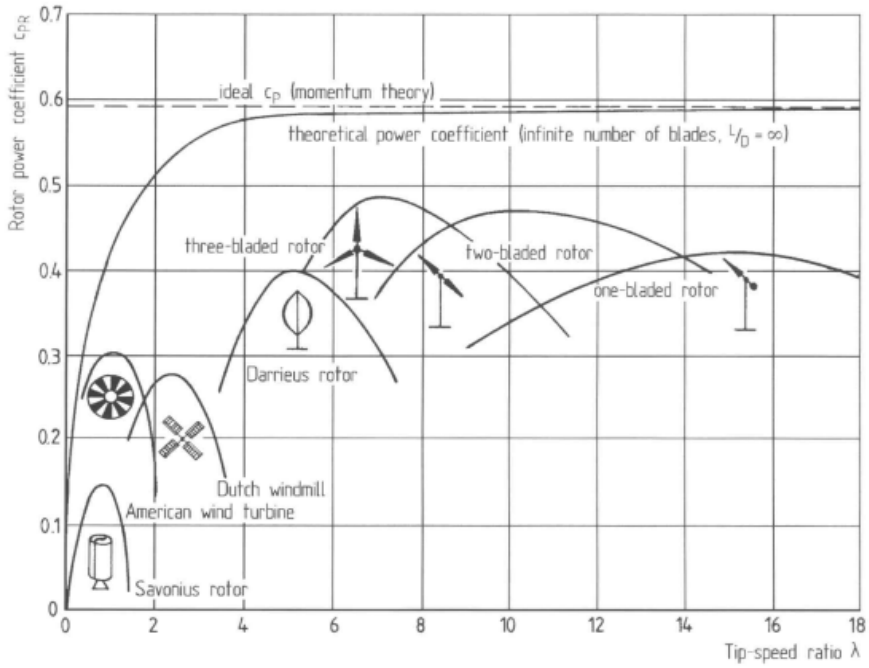

Figure 2.32: Power coefficient as a function of the TSR for different wind turbines [53]**.**

2.5.2.4. Ratings and specifications

As mentioned earlier, different wind speeds yield different amounts of electric power, hence rating different machines calls for a standard procedure. The specified rated capacity (SRC) is an index used to compare different wind turbine designs, it varies between 0.2 and 0.6 and it is defined by [52]:

$$SRC = \frac{Power\ rating\ of\ the\ generator}{Rotor\ swept\ area} \tag{2.22}$$

2.5.2.5. Capacity factor

The capacity factor delineates the capability of a wind turbine to generate power during a full year. It is calculated by dividing the actual energy output over the energy output when operated at rated power throughout the year [52]:

$$Capacity\ factor = \frac{Annual\ energy\ output}{Rated\ power \times Time\ in\ a\ year} \tag{2.23}$$

2.5.2.6. Wind power generating systems

The mechanical power is subject to the efficiency of electrical generation depending on the generating system used. Most of presently installed wind turbines employ one of the following generating systems, depicted in Figure 2.33:

- Squirrel cage induction generator.
- Doubly fed induction generator.
- Brushless generator with gear and full converter.
- Direct drive synchronous generator.

The squirrel cage induction generator is the oldest grid-coupled generating system. The amount of power generated varies according to the very small variations of the rotor speed, these variations are less than 5% which is why this type of wind turbines is called constant speed turbines. However, it is possible for squirrel cage induction generators to function at two different constant speeds by altering the number of pole pairs in the stator winding [54]. Squirrel cage induction generators consume reactive power, this is undesirable in the case of large turbines and weak grids. Therefore, to achieve a power factor close to one, capacitors are used to compensate the reactive power consumption.

The other generating systems (shown in Figure 2.33) are variable speed systems. Thus, they are used in variable speed turbines. It is important to decouple the rotor speed and grid frequency to allow variable speed operation, power electronics is used to allow such decoupling. In the doubly fed induction generator, the mechanical and electrical rotor frequency is decoupled by a back-to-back voltage source converter feeding the three-phase rotor winding. In this manner, the stator and rotor frequency are matched independently of the mechanical rotor speed [54].

In the direct drive synchronous generators, a power electronics converter is used to completely decouple the generator from the grid. The part of the converter linked to the grid is a voltage source converter, i.e., an IGBT (Insulated Gate Bipolar Transistor) bridge, while the other part linked to the generator can either be the same or a diode rectifier. The generator is excited using either an excitation winding or permanent magnets [51], [54].

Brushless generators have been around since 2005. This type of systems offers better grid-fault ride-through characteristics than the DFIG, and reduces the maintenance needed for and the failures caused by the brushes of the DFIG [51]. Several variants of this system are on the market since different generator types and different gearboxes can be used. A lot of manufacturers use permanent magnet (PM) generators, a large number

of pole pairs is need for such low speed machines which increases the overall cost of the generator. However, squirrel-cage induction generators are also used.

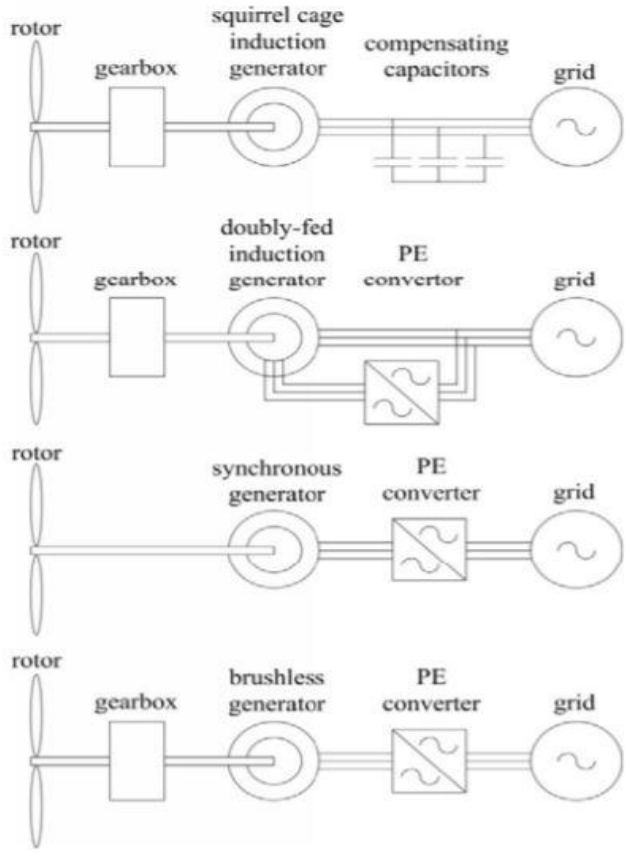

Figure 2.33: Commonly used generator systems [51]**.**

2.5.3. Types of wind turbines

Wind turbines are divided into two large families: those with vertical axis and those with horizontal axis [53]:

2.5.3.1. Horizontal axis wind turbines (HAWTs)

These machines are called HAWT because the rotor's rotation axis is horizontal, parallel to the wind direction. They generally comprise propellers with two or three blades, or multi-blade propellers for water pumping. They are the most widespread machines due to:

- Their superior performance to that of all other machines.
- They have a high efficiency.
- They are simple to design.

Two groups can be distinguished in HAWTs based on the number of blades in their propeller:

A) The slow-rotation wind turbines "multi-blade"

This kind of wind turbines is heavily used in the countryside, it has been there for a very long time. It is mainly used for water pumping.

B) The fast-rotation wind turbines

Such wind turbines have a two or three-bladed rotor, and they are mainly devoted to electricity production. They are further differentiated into two types based on the direction of the wind flow: the upstream-flow wind turbine and the downstream-flow wind turbine as shown in Figure 2.34.

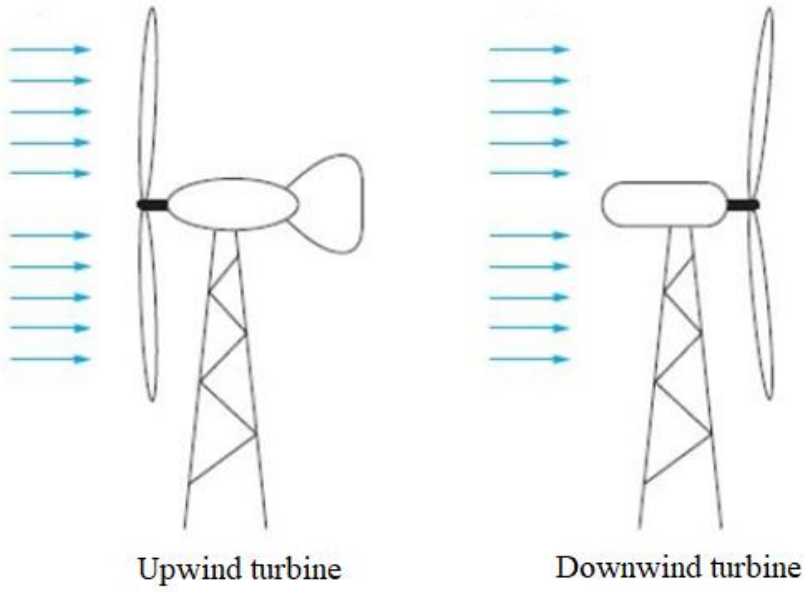

Figure 2.34: Upwind vs downwind turbine [55]**.**

C) Choice of the number of blades

Choosing properly the number of blades plays a big role in the power extraction efficiency. On the one hand, blades that are too close to each other result in little power extraction, the same applies to blades that rotate too fast, because every blade faces the turbulent air caused by the preceding one. On the other hand, blades that are far apart or move too slowly also result in low power extraction since the air stream passes through the turbine without real interaction with the blade. Hence, the number of blades is dependent on the TSR. If (t_a) is the time required for a blade to reach the position of the previous blade for an n-bladed turbine that rotates at an angular velocity (ώ), then it is given by:

$$t_a = \frac{2\pi}{n\,\acute{\omega}} \tag{2.24}$$

Now if (t_b) is the time that the disturbed wind (cause by the interference of the blade) takes to move away letting normal air be reestablished, it will depend on the speed of wind (v) and the length of the perturbed wind stream (d) by the following equation:

$$t_b = \frac{d}{v} \tag{2.25}$$

To have maximum power extraction (t_a) and (t_b) should be approximately the same:

$$\frac{\acute{\omega}}{\mathrm{v}} = \frac{2\pi}{n\,d}$$

In modern wind turbines, the empirical measurement of (d) and the requirement of a high TSR lead to a small number of blades, generally only two or three. Both two-blade and three-blade designs are popular, but the choice depends on some factors. The lighter the nacelle and the simpler the erection, the more suitable for two-bladed turbines. Though three-bladed turbines are about 33% heavier and costlier, they have about a 5% to 10% greater power coefficient, smooth power output, low blade fatigue rates and hence less prone to failure.

2.5.3.2. Vertical axis wind turbines (VAWTs)

For these turbines, the axis of rotation is vertical and perpendicular to the wind direction, they were the first to be developed for electricity production. The main advantage for VAWTs over HAWTs is having the control devices and the generator on the ground, which means that they are easily accessible. Moreover, they are suitable for all wind speeds and do not require orientation. Savonius and Darrieus are the two most known VAWTs (Figure 2.35).

A) Savonius

The Savonius wind turbine mainly comprises two half-cylinders whose axes are offset with respect to each other. Like paddle machines, it uses basically the drag to turn. This machine has two advantages:

- It is simple to manufacture.
- It starts with wind speeds of around 2 m/s.

B) Darieus

The Darrieus wind turbine was named after its inventor, it is basically a rotor whose shape is reminiscent of an egg beater. This machine is well adapted for electricity supply. However, its main drawback is the fact that it cannot start alone.

Darieus Savonius

Figure 2.35: Darieus and Savonius wind turbines [55]**.**

2.5.4. Wind turbine control systems

Wind speed is not constant and varies continuously, thus, control systems are required to keep wind turbines functional. In case of HAWTs, orientation is necessary to face the wind direction. Moreover, high speed winds cause overloading which is why it is desirable to limit the power output so as to protect the generator and the power electronics equipment. At gust speeds, the machine must stop or turn out of the wind, while power should be captured as efficiently as possible at low and moderate wind speeds.

Data sheets of wind turbines reveal the output at a particular wind speed that is considered to be nominal, this speed is generally between 9 and 16 m/s [52]. choosing the rated wind speed depends on the wind characteristics of the site, and the rated wind speed is needed for when choosing the best generator rating. Control mechanisms for wind turbines are divided into four categories as will be discussed in the following subsections.

2.5.4.1. Pitch angle control

The pitch angle control system operates the blades actuators to alter the pitch angle as the wind speed varies. The input to the pitch controller is the difference between the electrical power output and the rated power. These systems achieve high efficiencies since they continuously align the blade in the direction of the wind. When the wind speed exceeds the rated speed, the pitch angle control system turns the blades gradually about the longitudinal axis to increase the pitch angle. Thus, the rotor's aerodynamic efficiency is reduced and its power output decreases. In the same way, As the safe speed limit is exceeded, the pitch angle is again changed to reduce the power output to zero and shift the machine to the stall mode. When the gust is over, the pitch angle takes back its normal position so that the turbine restarts. At normal wind speeds, the system tries to settle the blade pitch angle to a value at which the output power and the rated power are equal [54].

2.5.4.2. Stall control

Stall control is used to restrain the power output at high wind speeds, and it is usually applied to constant-pitch turbines that are connected to the network. The network fixes the rotor speed, allowing variations of only 1% to 4%. Stall control is further divided into two types:

A) Passive stall control

For a blade rotating at a constant speed, increasing the wind speed increases the angle of attack. If this increase in the angle of attack surpasses a particular angle, the lift force starts decreasing which causes the rotor efficiency to drop. To reduce the power output at high winds, the lift force can be reduced by shaping the rotor blade profile in a way that causes turbulence on the side of the blade not facing the wind. A passive controlled machine shows a decline in power at high winds as seen in Figure 2.36.

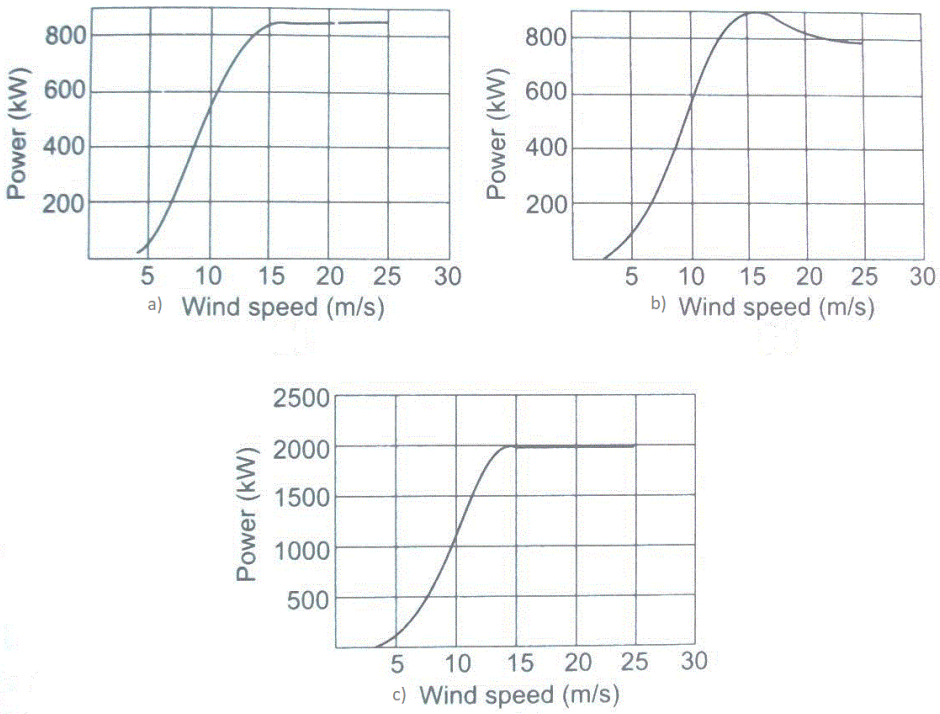

Figure 2.36: Power profile: a-pitch control, b-passive stall control and c-Active stall control [52]**.**

B) Active stall control

Active stall control is usually used in high capacity machines owing to economic reasons. The control is done by rotating the blade a few degrees in the direction opposing that of the pitch-controlled machine discussed earlier. This controls the angle of attack and keeps the output power at the rated value for all high winds that are below the furling speed. This action is sometimes referred to as deep stall.

2.5.4.2. Power electronics control

In systems with power electronics control, a power electronics interface is incorporated between the generator and the grid or the load, this interface allows the control of the delivered electrical power. The use of power electronics to control a DFIG emulator is detailed by Z. Dekkali et al in [56], the work explains how active and reactive powers are controlled under vector control by controlling the rotor current quadrature (Iqr) and direct (Idr) components respectively.

Power electronics control offers a smooth operation and does not require any mechanical action. However, the continuous control of rotor speed yields continuous fluctuation in the power output which is not desirable. In addition, the fast variation of rotation speed translates into a large difference between the input and output power which also means a large moment of inertia and hence more stress is applied on the blades.

2.5.4.3. Yaw control

Yaw represents the angle of the nacelle and the yaw system is in charge of continuously orientating the rotor towards the direction of the wind. In small turbines for instance, a tail-vane is used to achieve the yaw control. Moreover, active yaw control systems use motorized systems, which are either activated by a fan-tail, or by centralized instruments that detect the direction of wind. Passive yaw control is done without any additional mechanism, since mounting the turbine downwind allows the thrust force to automatically push the turbine in the wind's direction [57]. Since the orientation of the turbine has an effect on the rotor's rotation speed, the latter can be indirectly controlled by the yaw control mechanisms. Hence to reduce the mechanical power at high wind speeds, the yaw angle is set to make the rotor face away from the wind direction. One particular downside to the yaw control is the fact that it produces loud noises, especially in large machines, contributing more to noise pollution.

2.5.4.4. Control strategy

Wind speed has different ranges as shown in Figure 2.37. For each range a different control strategy is required. Below the cut-in speed, the machine does not generate power, although this speed range may provide sufficient torque to start rotating the machine leading to free rotor rotation. Normal wind speeds allow for maximum power extraction. The latter is achieved at a particular value of the TSR, so the rotation speed is continuously changed to keep a constant TSR, and hence, track the maximum power point. The rotor speed is limited at high wind speeds, the maximum speed attainable is dependent on the design of the mechanical components. The power coefficient C_p is kept below its maximum value and power output becomes disproportional to the cube of the wind speed. As the wind speed keeps on increasing, the power output is kept constant at the maximum value allowed by the electrical components until reaching the cut-out speed, where the power generation is shut down and the rotor is stopped for protection purposes.

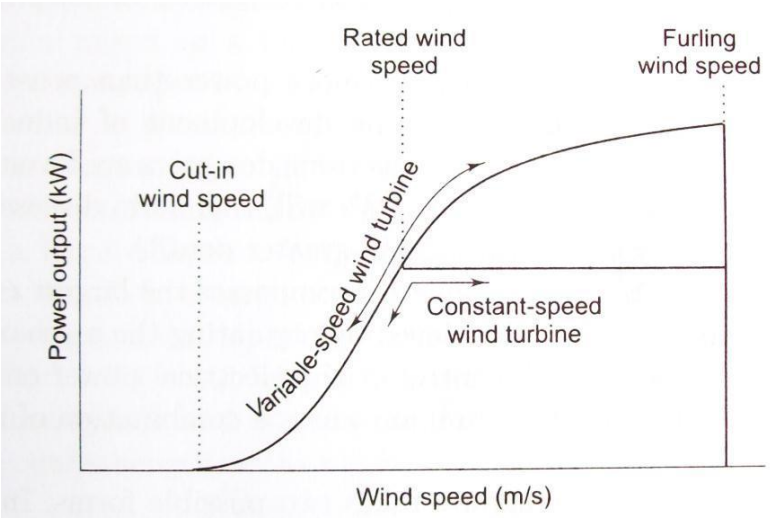

Figure 2.37: Power versus wind speed characteristic of wind turbines [52]**.**

In normal wind speeds, the control strategy is divided into two categories based on the electrical power generating system used:

- Fixed-speed generation.
- Variable-speed generation.

The constant-speed generation scheme is necessary for systems involving grid-connected synchronous generators. However, the power extraction cannot be maximized in fixed-speed generating systems as the extraction of maximum power requires a constant TSR. This means that the rotational speed must be proportional to the wind speed. Thus maximum power extraction is possible only with variable speed generating systems, such systems yield 20% to 30% more power than constant-speed generation systems [52].

In order to maintain a constant TSR, pitch control is employed to regulate the mechanical power input, and power electronics control is used to regulate the electrical power output. There are two ways to apply the control:

In the first method, the TSR corresponding to maximum C_p is saved in a microprocessor to be compared to the operating TSR which is obtained from the measured wind and rotational speeds. Whenever there is a difference between the optimal and operating TSR, an error signal is generated. A positive difference implies that the TSR is greater than the optimum, and the rotational speed is reduced as the power electronics converter increases the power output. In case of a negative difference, the opposite action is performed. The disadvantages of this method are the fact that measured wind speed in the vicinity of a wind turbine gives unreliable values due to the shadowing effect. In addition, the value of the TSR for maximum C_p changes during the lifetime of a wind turbine, and thus it is difficult to determine.

The second method relies on the fact that the curve of C_p versus TSR has a single maximum point to continuously track the maximum power point (MPP). In this method, small speed variations are introduced and the power output is measured for each variation to evaluate $\frac{\Delta P}{\Delta \omega}$. A positive ratio means that increasing the speed yields more mechanical power. To achieve that, the power electronics control decreases temporarily the electrical power output and as the mechanical power increase the electrical power is again raised to a higher value. The process continues until the optimum speed is reached. A large difference between mechanical and electrical power results in a large torque which means more stress on the rotor components, this should be considered while controlling the rotational speed and the acceleration and deceleration rates must be limited.

2.5.5. Effect of wind energy systems on the grid

2.5.5.1. Local level effects

On a local grid level, wind power systems impact the following aspects [54]:

- Branch flows and node voltages.
- Protection schemes, fault currents and switchgear ratings.
- Harmonics.
- Flicker.

The first two aspects are generally to be investigated before linking the power supply system with new generation capacities. These issues apply to all cases where a generator is connected to a grid. The third aspect is present when power electronics converters are used to couple the generators with the grid, this is to say that it applies to variable speed turbines, mainly where high speed synchronous generators are connected to the grid via power electronics. The flicker though is specific for constant speed wind turbines.

Wind turbines affect the voltages at neighboring nodes, and the form of this effect is dependent on whether it is a constant speed or variable speed turbine. In constant speed turbines, particularly the squirrel cage induction generator, there is a constant relation linking the rotor speed, terminal voltage, the active and reactive powers. Therefore, its terminal voltage cannot be affected by changing the reactive power exchange with the grid. Hence for voltage control, capacitor banks and SVCs (Static Var Compensators) are necessary.

Variable speed turbines are able to vary the reactive power over a range determined by the size of the power electronics converter:

- Direct drive variable speed turbines often have a large converter and offer the possibility to add extra capacity which allows more control of reactive power at a low cost.

- Turbines equipped with doubly fed induction generators have generally small converters since the rotor capacity is just about one third that of the stator.

The contribution to the fault current is different for the three main types of wind turbines. Constant speed wind turbines, with grid coupled squirrel cage induction generators, contribute to the fault current. DFIG turbines also cause fault current but for very short durations thanks to the sensitivity of power electronics to overcurrent. Wind turbines based on direct drive generators have no contribution to fault current since their power converters cannot carry fault currents [54].

Power electronics is the main source of harmonics; thus, the third aspect is present only in variable speed turbines. Though this is not an in issue in modern converters as they are equipped with advanced control algorithms at high switching frequencies and robust filtering techniques. the harmonics issue should not be a major problem.

The last aspect is a typical problem for wind turbines as wind is never constant. Constant speed turbines translate the wind fluctuations directly into output power fluctuations which results, depending on the grid connection, in grid voltage fluctuations. This problem is known by flicker. On the other hand, variable speed turbines do not suffer from flicker problems, because the set point for active power is derived from the rotor speed. The latter acts an energy buffer or a low pass filter due to its inertia, and thus, rapid fluctuations of wind speed are hardly noticed in the power output.

Table 2.5 shows a summary of the local impacts for different kinds of wind turbines:

Table 2.5: Local impacts of wind turbines [54]**.**

Local impact	**Constant speed**	**Doubly Fed**	**Direct Drive**
Changes in node voltages	Yes, compensation only possible with additional equipment like capacitor banks and SVCs	Yes, compensation theoretically possible, but dependent on converter rating	Yes, compensation theoretically possible, but dependent on converter rating
Harmonics	Hardly of interest	In theory of interest, but should not be a major problem	In theory of interest, but should not be a major problem
Flicker	Important, particularly in weak grids	Unimportant because the rotor acts as an energy buffer	Unimportant because the rotor acts as an energy buffer
Contribution to fault currents	Yes	Yes, but turbine is normally quickly disconnected	No, converter not capable of carrying fault current, turbine is quickly disconnected

2.5.5.2. System wide level effects

Wind energy systems affect widely the overall stability of the grid, they have an impact on the grid dynamics, voltage and frequency control and the generation of reactive power. Wind turbine generation systems do not use conventional synchronous generators, this has an impact on the overall stability and dynamics of the power system. In fact, the way wind turbine generating systems respond to voltage and frequency changes are a mere reflection of their working principle. The impact of wind systems on the stability of the power system can only be determined with the help of adequate wind turbine models [52].

There are many reasons for wind power to affect both voltage control and reactive power generation. One impact on voltage control is the fact that not all wind turbines can vary their reactive power output. Apart from this, wind power plants are not flexible like conventional power plants in terms of location, because they affect the scenery and are resource-dependent. Hence, the choice of location may not favor grid voltage control. Another factor that impacts voltage control is the relative weak coupling between the turbine and the electric system as wind turbines have rather low output voltages. Moreover, the prime mover of wind power cannot be controlled which also has an impact on system balancing (i.e., frequency control and dispatch of the other conventional units). Thus, the power generated by wind turbines is also uncontrolled and does not contribute to frequency regulation. It is worth mentioning that such controllability would technically be possible, but it would reduce the energy yield resulting in income reduction [52].

Furthermore, it is complicated to dispatch the other conventional units that supply the load due to the variability of wind and especially on the longer term lasting from 15 minutes to hours. This variability causes a mismatch between the demand and the power coming from conventional units (load minus generated wind power). Short term (seconds) output power fluctuations are generally not problematic especially in the case of a large number of wind turbines. The impact of wind power is proportional to the wind power penetration, so more penetration means a more important impact which requires a strongly-connected grid.

2.6. Hybrid Energy Systems

Hybrid Renewable Energy Systems (HRES) have many terms and definitions, they can operate in distributed generation (DG) or centralized generation (CG). In such systems, at least two or more energy sources are hybridized to generate electricity, of which at least one source is renewable (Photovoltaic, Biomass, Wind, Hydrogen). Storage systems are also present in HRES, especially in stand-alone systems [58]. Storage technologies are diverse and depend on their application, their capacity and the duration of storage:

- Electrochemical batteries (Pb, Li, etc.).
- Heat pumps.
- Hydrogen fuel cells.
- Compressed air energy storage (CAES).
- Flywheels.
- Capacitors.
- Superconducting magnetic energy storage (SMES).

Table 2.6 below summarizes the storage technologies in terms of their applications and duration.

Table 2.6: **Storage technolgies and their applications** [59]**.**

Full power duration of storage	Applications of storage and possible replacement of conventional electricity system controls	Biomass	Hydrogen Electrolysis + Fuel Cell	Large Hydro	Compressed Air Enegry Storage (CAES)	Heat or cold store + heat pump	Pumped Hydro	Redox Flow cells	New and Old Battery Technologies	Flywheel	Super Conducting Magnetic Energy Storage	Supercacitor	Conventional Capacitor and Inductor
4 Months	Annual smoothing of loads PV, Wind, and small Hydro		*	*									
3 Weeks	Smoothing weather effects: load, PV, Wind , Small Hydro	*	*	*									
3 Days	Weakly smoothing of loads and most weather variations	*	*	*	*	*	*	*					
8 Hours	Daily load cycle PV, Wind, Tranmission line repair	*	*	*	*	*	*	*	*				
2 Hours	Peak load lopping, standing reserve, wind power smoothing. Minimization of NETA or similar trading penalties	*	*	*	*	*	*	*	*				
20 Minutes	Spinning reserve, wind power smoothing, clouds on PV.		*	*	*	*	*	*	*	*			

3 Minutes	Spinning reserve, wind power smoothing of gusts		*				*	*	*	*			
20 seconds	Line or local faults, Voltage and frequency control. Governor controlled generation							*	*	*	*	*	*

However, storage is sometimes optional as is the case for grid-connected systems. HRES exploit local renewable resources to reduce conventional fuel consumption, their capital cost is high compared to conventional technologies but the long-term fuel savings and the environmental benefits outweigh it [60].

2.6.1. Types of hybrid energy systems

There are many ways to classify hybrid energy systems, they are commonly distinguished based on their connection to the grid which comes down to the application and financial cost.

2.6.1.1. Off-grid systems

In such topology, there is no link between the system and the grid, this means the load demand is met by the system all the time. This topology faces issues with reliability and performance as resources are limited and may not suffice, or overproduction might occur and the excess has to be discarded. Thus, this configuration is only suitable for locations without or with very expensive grid connection. Figure 2.38 illustrates an off-grid system.

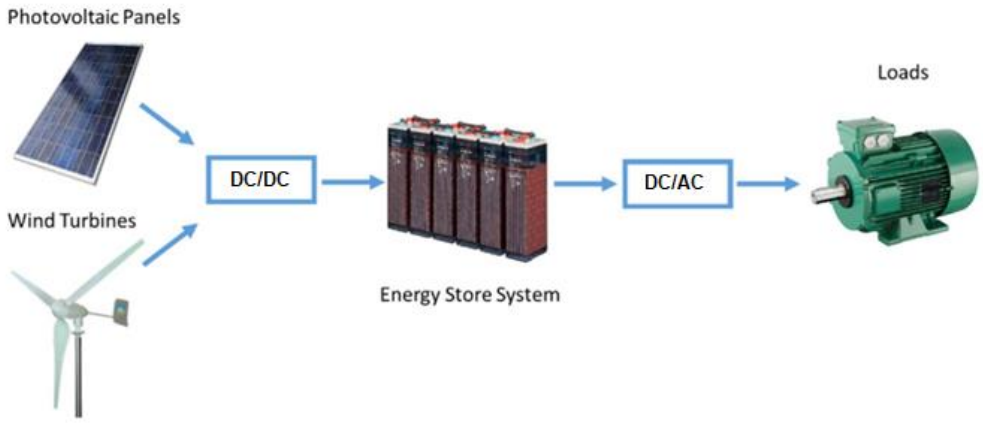

Figure 2.38: Stand-alone hybrid energy system [61]**.**

2.6.1.2. On-grid systems

Such systems are interconnected with the grid as seen in Figure 2.39 below, which insures that the demand is always met even in energy deficit situations. Unlike off-grid systems, on-grid systems are more performant and provide the possibility to sell and distribute the excess of energy in the market. Consequently, this configuration calls for new production models depending on the consumption and distribution which also requires new energy management strategies [61].

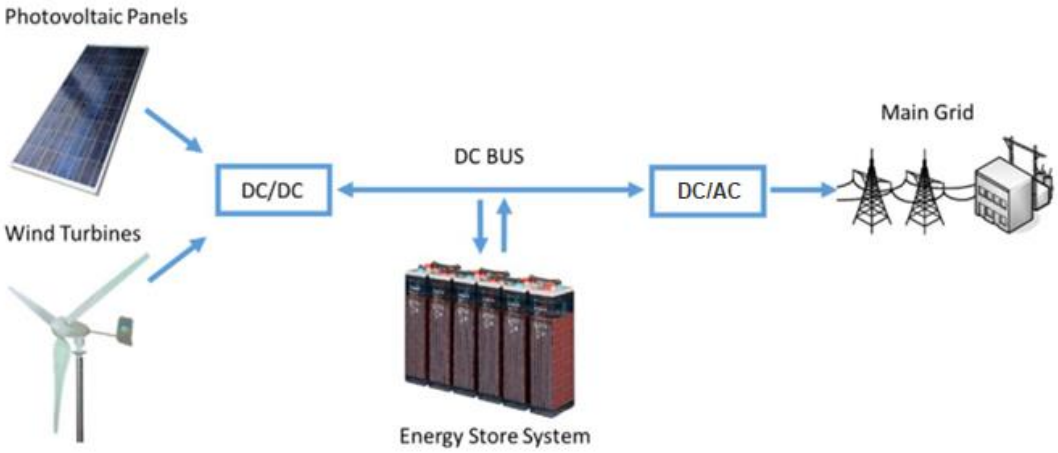

Figure 2.39: Grid-connected hybrid energy system [61]**.**

2.6.1.3. Grid-tied inverters

Grid-connected inverters are required to convert DC power into AC power with specific voltage magnitudes at proper frequencies that match the utility grid. There are many types of grid-connected inverters as shown in Figure 2.40. In line-commutated inverters, the communication process is dictated by the utility grid [62].

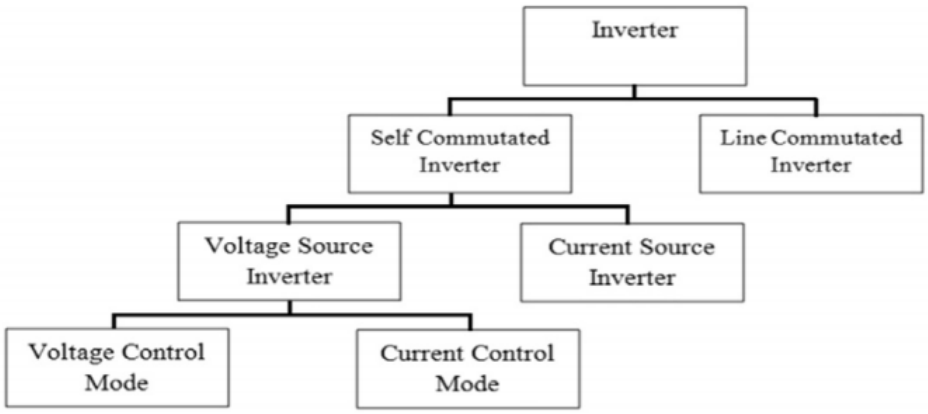

Figure 2.40: Classification of grid-tied inverters [62]**.**

The self-commutated inverters use power switching devices that transfer the current in a controlled way. This kind of inverters uses power MOSFETs (Metal Oxide Semiconductor Field Effect Transistors) for powers less than 10 kW and high-frequency switching (20–800 kHz). For medium to high power exceeding 100 kW and switching frequencies limited to 20 kHz, they use Insulated Gate Bipolar Transistors (IGBTs). Self-commutated inverters use pulse width modulation (PWM) to generate AC waveforms and they can control the output voltage and current waveforms as well. In addition, they are resistant to grid disturbances and can adjust the power factor and suppress current harmonics [62].

2.6.1.4. Grid-tied inverter topologies

The different grid-tied inverter topologies are briefly discussed in the following subsections and presented in Figure 2.41 [62].

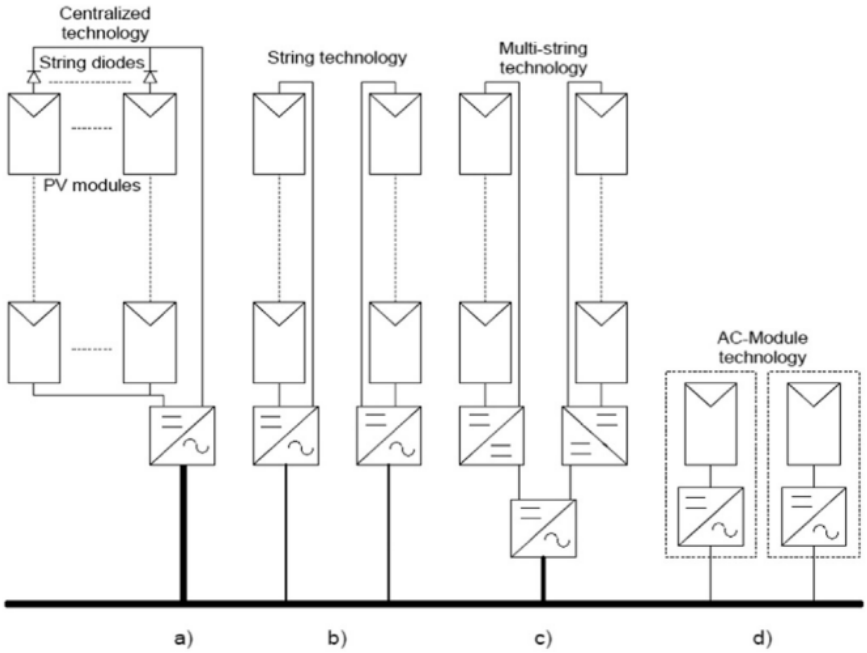

Figure 2.41: Topologies of grid-connected inverters

A) Centralized inverters

Line-commutated inverters were the first grid-connected inverters (see Figure 2.41 (a)) with power ratings of several kilo watts. They were unreliable, heavy and difficult to install with poor power factors and high harmonic content. Nowadays, self-commutated inverters are more commonly used in centralized inverters as thyristors are replaced by advanced transistor switching devices.

B) String inverter

String inverters, depicted in Figure 2.41 (b) are a short version of centralized inverters and they are the most common in present days. The inverter is connected to a single string of PV modules which translates into a low output power range. There are no losses in the single string inverter and thus they have 1% to 3% higher efficiency compared to the previous type [63].

C) Multi-string inverter

Multi-string inverters, shown in Figure 2.41 (c), retain the advantages of single-string inverters (like efficiency and reliability) but offer a higher power level. In the multi-string inverter, PV strings are linked to low power DC-DC converters equipped with MPPTs. A DC bus connects all DC-DC converters to the grid through a single high-power inverter.

D) AC module

AC modules consolidate the inverter and the PV module into a single system called module integrated system as seen in Figure 2.41 (d). In this kind of inverters, the mismatch losses are removed since there is only one PV module. Functions like voltage amplification, MPPT and DC-AC conversion are all performed in a single stage. However, the circuit topologies are complicated [63].

2.6.2. Topologies of hybrid energy systems

The topologies are based on the type of the interconnection bus, which physically links all the elements of the system. Three types can be distinguished as: DC, AC and hybrid.

2.6.2.1. DC Bus

The DC bus topology is used in low power applications because it is simple to use and offers reduced losses, these technical advantages facilitate its use and eliminates power quality problems. On the other hand, a large number of converters is needed since most loads require AC power. Figure 2.42 gives an example of a DC bus topology [64].

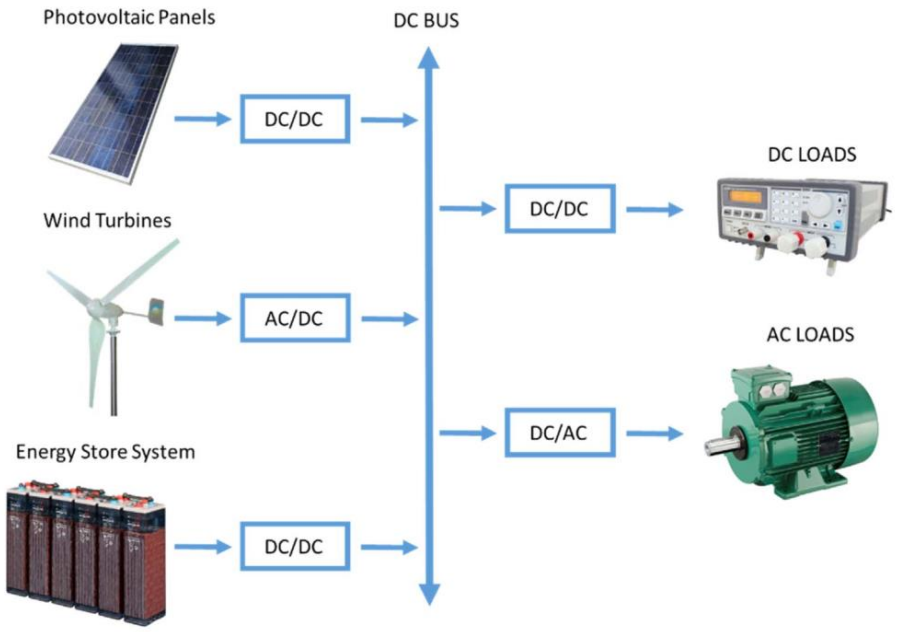

Figure 2.42: PV-wind system with DC bus topology [61]**.**

2.6.2.2. AC bus

AC buses are suitable for medium and high production applications because operating AC power is simpler at higher voltages compared to DC and insures a reduction in the system's internal losses. However,

this topology requires elements for power quality correction, without which, the stability and integrity of the system can be endangered [64]. An example of an AC bus-based topology is shown in Figure 2.43.

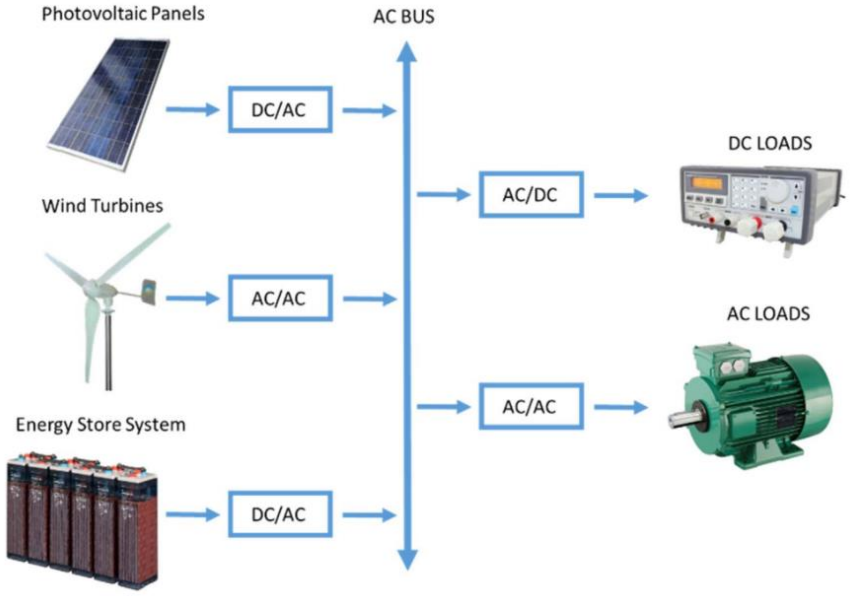

Figure 2.43: Hybrid energy system with AC bus topology [61]**.**

Furthermore, this configuration powers inductive loads that reduce the power factor, and electronic ones that produce harmonics. Hence, filtering and compensation is necessary, and so the system becomes more complex and expensive.

2.6.2.3. Hybrid bus

In this configuration, both DC and AC buses interconnect generators with loads of the same nature as demonstrated in Figure 2.44. The main benefit of such topology is the reduction of power converters. But this is compromised with the complexity of its control, since the system is operated on two different networks ensuring power balance at all times [61].

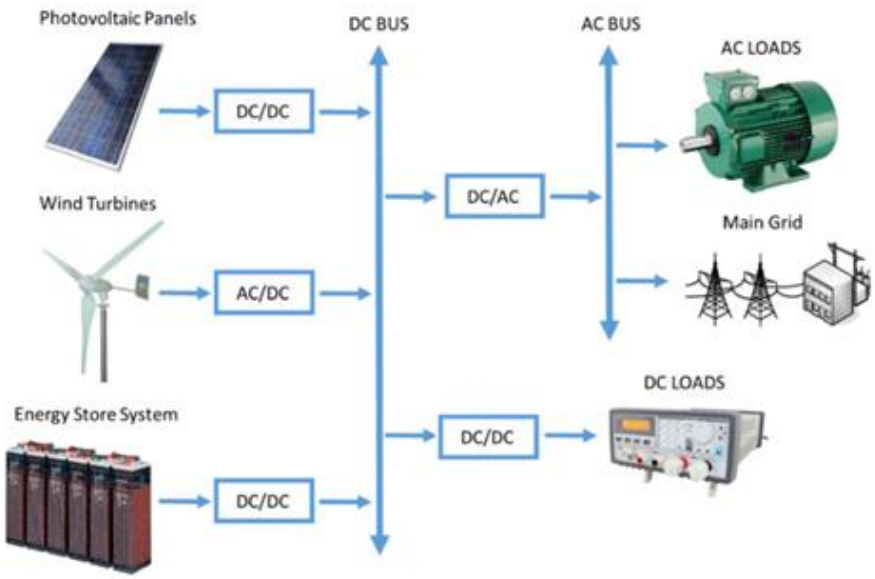

Figure 2.44: Hybrid-bus based system with storage [61]**.**

CHAPTER THREE: METHODOLOGY

Outline

3.1. Introduction

In this chapter the different software tools used for the simulation will be described, and the weather and load profile of the case study will be examined. The hybrid system will be designed and sized according to the available energy potential and electricity consumption rates. Afterwards the designed system will be modelled in MATLAB and simulated. For economic and environmental analysis, the system will be modelled in HOMER and simulated with the same data. Finally, a review of project economics is also provided at the end of the chapter.

3.2. Software

In this work three software tools were used to first obtain the weather file of the location under study, and then perform the modelling and simulation of the designed system, and finally conduct the economic and environmental study of the system.

3.2.1. METEONORM

Real weather data of the studied region is rare and very difficult to obtain. Therefore, for simplicity, METEONORM version 7.1 was used to generate the weather file of Adrar. The software is developed by METEOTEST institute, and it is a widely accepted data source. It was released in 1985 and has a database of 8350 weather stations around the world [65]. In order to generate weather files, METEONORM uses weather stations and satellite images of the location on an hourly or three-hourly basis. The software interpolates data of close by locations (10 to 30 km in Europe and Africa) to generate weather files for areas without weather stations and where data is not available. Thus, the generated weather files contain some uncertainties that range from 2% to 10% [65]. METEONORM generates data for one typical year representing the average of the years with available data.

3.2.2. MATLAB

The modelling of the system in this work was done in MATLAB, which is a numerical computation and simulation environment. The interface of MATLAB is user friendly with plenty of documentations, and it is based on numerical libraries that where developed in FORTRAN like EISPACK and LINKPACK.

MATLAB contains the Simulink toolbox, which is used for creating simulation models in the form of graphical interfaces much like block diagrams. Simulink includes C libraries of linear, non-linear, continuous, and discrete functions that are in the form of blocks [23]. Besides Simulink, MATLAB has a lot of other

toolboxes for power systems, control systems, signal processing and many more. It is used by millions of engineers worldwide.

3.2.3. HOMER

HOMER is a famous software that is heavily used for designing renewable energy systems worldwide. In 1993 the NREL (National Renewable Energy Laboratory) developed the software and in 2009 executed a commercial license [8]. The main use of HOMER is to evaluate the performance of energy systems. HOMER performs three tasks; hourly simulation, optimization and then sensitivity analysis. The software also provides detailed technical feasibility and life cycle cost study. To optimize the proposed system, HOMER uses different configurations to find the one that is technically feasible with minimum life cycle cost. The software is programed under C++, and runs under windows operating system.

3.3. Simulation Data

To see the performance of the system, the simulation was performed for two months; August representing the summer period where the peak loads appear accompanied with high temperatures, and January for the winter period where the wind energy potential and the load are the lowest.

3.3.1. Weather data of Adrar

Data of solar irradiation, wind speed and temperature were extracted from the generated weather file (see appendix Figure A.2). The data in the weather file is in an hourly form and covers many parameters. The typical year is 2005 and it covers the average of ten years starting from the year 1995. The relevant extracted data is represented in Figure 3.1, 3.2 and 3.3.

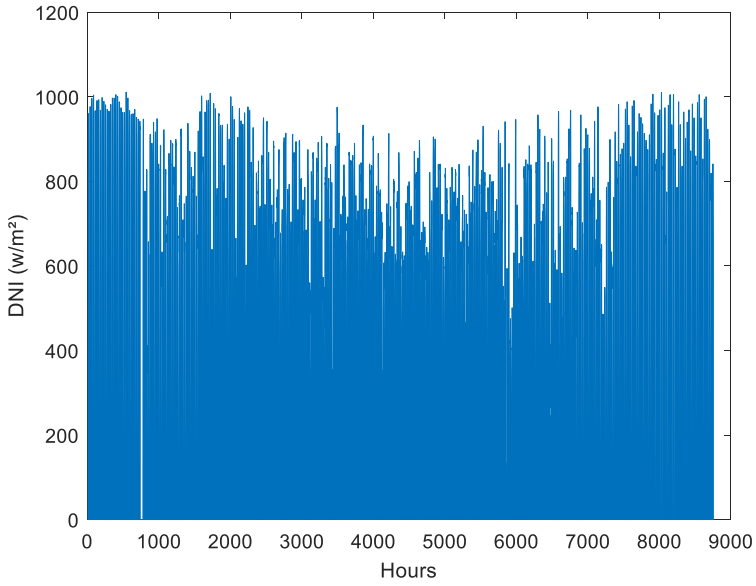

Figure 3.1: Hourly direct normal irradiation for one year.

The figure above shows very high direct normal irradiation content, especially in winter and autumn, and the software indicates an error of 10%. The DNI levels tend to decrease in the hot season.

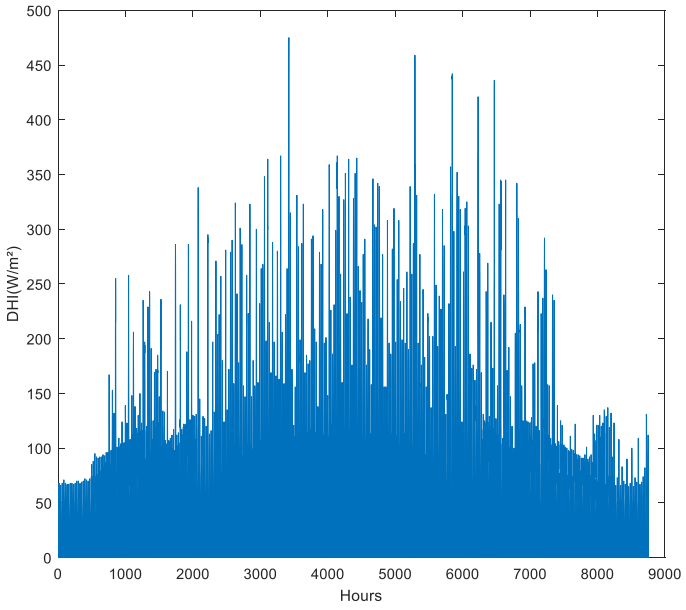

Figure 3.2: Hourly diffuse horizontal irradiation for one year

Unlike DNI; the diffuse horizontal irradiation (DHI) reaches its highest levels during summer, however it rarely surpasses 350 w/m².

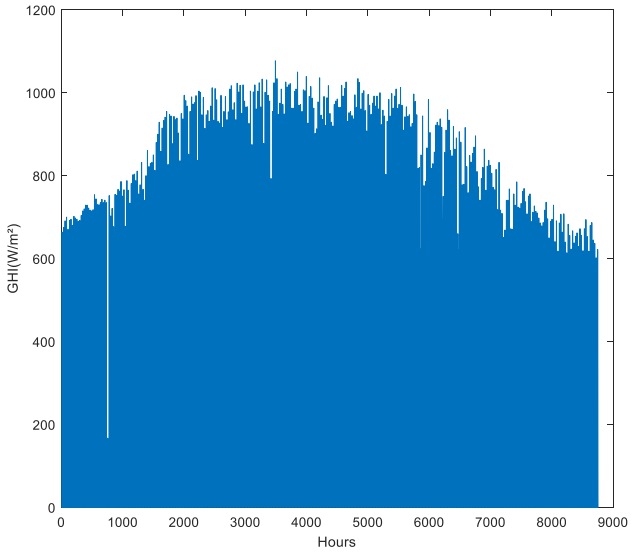

Figure 3.3: Hourly global horizontal irradiation for one year

The global horizontal irradiation shows a different trend from its predecessors with the highest levels of GHI extending from spring to autumn.

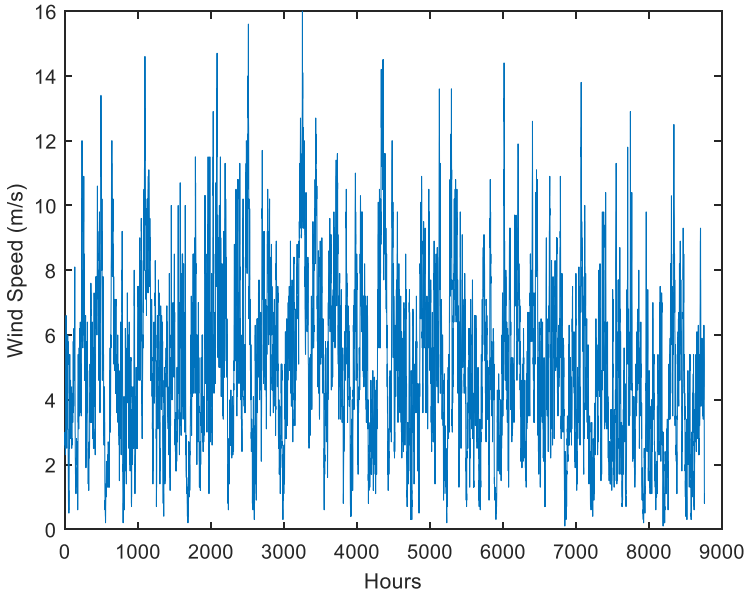

Figure 3.4: Hourly wind speeds for one year.

Wind speed data show and average speed of around 6 m/s, and the maximum speed is around 16 m/s which very suitable for wind energy systems considering wind turbines with high hub heights.

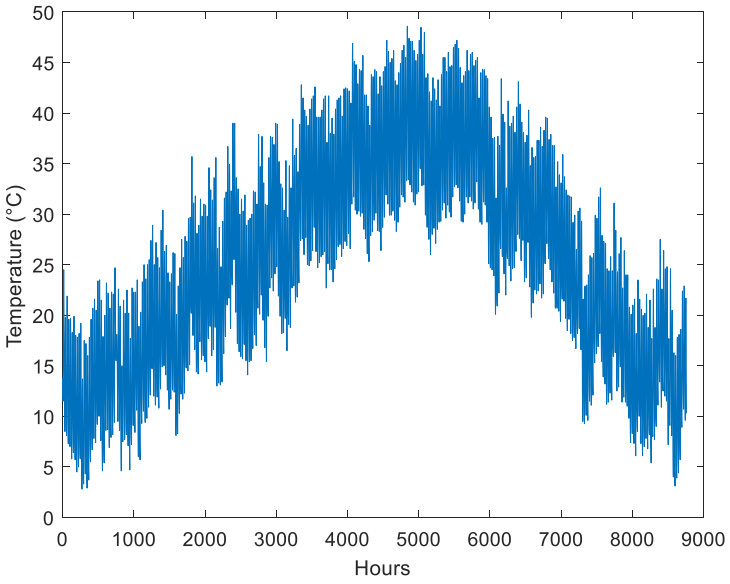

Figure 3.5: Hourly temperature for one year.

The trend for temperature shows a noticeable increase in the summer season, this would slightly decrease the efficiency of the PV generator but for the other seasons it is much cooler and more favorable. Again, the error in temperature data is at 0.3 °C.

3.3.2. Load Profile of Adrar

The load profile of Adrar covers the amount of power consumed by the different sectors in the town. Hourly data was not available at Sonelgaz (the national electricity distribution company), however, daily data was used to determine the peak demand in the region. For representing the load, hourly power production data of the Adrar's central power plant was used instead, due to its availability. It is worth mentioning that the central power plant not only supplies entirely the commune of Adrar, but part of its production goes to the neighboring communes as well. The figure below depicts the power produced from the plant for the year 2017, in fact the real load of Adrar is much less than this.

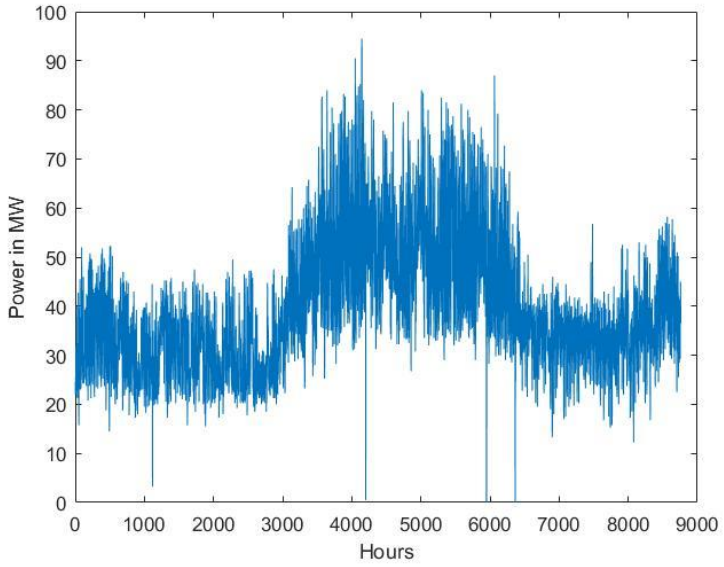

Figure 3.6: Power output of Adrar's central power plant in 2017

It can be easily seen from the presented data that the peak demand occurs during summer, this is justified by the cooling load since the place has a Saharan climate and the temperature skyrockets at this period. Although consumption rates in August are the highest, the peak demand in Adrar for the year 2017 occurred in June and reached 63 MW, this represents an increase of about 6.5% compared to 2016. Table 3.1 shows peak demand data obtained from Sonelgaz.

Table 3.1: **Summer peak demand in Adrar.**

Installed capacity (MVA)	Summer peak 2016 (MVA) (09-08-2016) (1)	Summer peak 2017 (MVA) (11-07-2017) (2)	Rate (%) (2)/(1)	Maximum summer peak (MVA) (29/06/2017) (3)	Increase (MVA) (3)-(2)
Adrar 80 MVA	**59.27**	**62.31**	**5.1**	**63.1**	**0.8**

3.4. System Design and Sizing

The sizing of the system is based on the production capacity and the energy potential of Adrar, while the design addresses the performance and capital cost of the overall system. Thus, the system is sized so as to meet at least half of the peak demand in Adrar, opting for a higher capacity is not viable since the capital cost will be too high and a vast area will be required. This has so many drawbacks, for instance, it will be too cumbersome to clean PV panels from dust depositions. In addition, the design employs certain topologies to maximize the power output, minimize losses and reduce the upfront investment needed.

3.4.1. The PV system

The PV generator produces 5 MW and comprises a total of 14320 panels, with each panel having a rated power of 350 watts. To provide higher power levels, the multistring inverter topology has been adopted. Each DC-DC boost converter is linked to an inverter, while connecting five PV-panel sets in parallel. Each PV-panel set contains eight panels in series. The PV system as a whole contains 358 inverters, 358 boost converters and a total of 14320 panels distributed over the 358 strings.

To minimize the surface needed for panels, the two sets of each string face the south with a spacing distance of three meters between the panels to avoid shading. The strings are then placed side by side as shown in Figure 3.7, with this configuration the area is minimized to about 0.064 km².

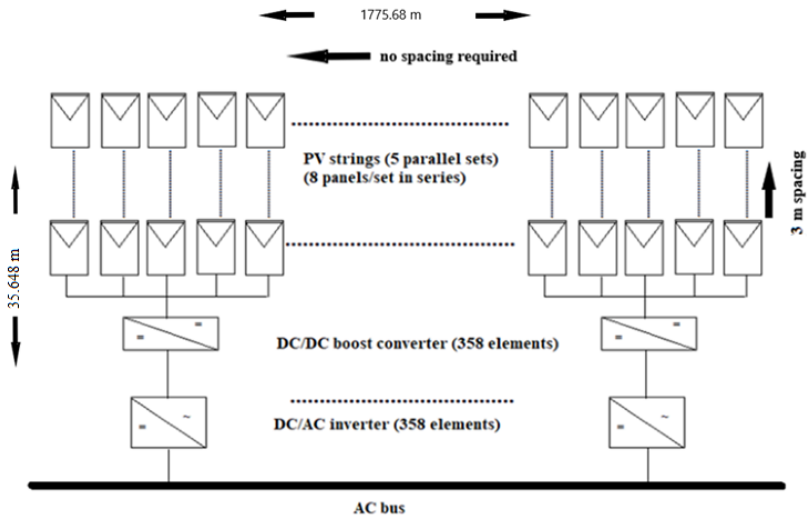

Figure 3.7: PV plant scheme

The PV panels face southwards with an optimal tilt angle of β=25°. The choice of (β) is based on the latitude (Ø) of Adrar. Since (25° < Ø=27.52° < 50°), then according to [66], the optimal fixed tilt angle is defined as : ($\beta = 0.76 \times \emptyset + 3.1$).

3.4.2. The wind system

The wind system consists of 10 large wind turbines, each one has a rated power of 3 MW. As mentioned in the literature review, Adrar is in a region of pressure difference close to the Atlantic Ocean. Wind patterns show that wind blows from the west, and for this reason the wind turbines face westwards. Considering the general rule-of-thumb for wind farm spacing that speculates a spacing distance of about five to seven rotor diameters between two turbines [67], and to avoid turbulence and ensure maximum power extraction, a spacing distance of 450 meters is to be maintained. The 10 turbines are divided into three sets.he first set comprises four aligned turbines, while the other two sets contain three turbines each. The scheme shown in Figure 3.8 shows the configuration of the wind turbines. The estimated surface required for the wind system is roughly 1.8 km².

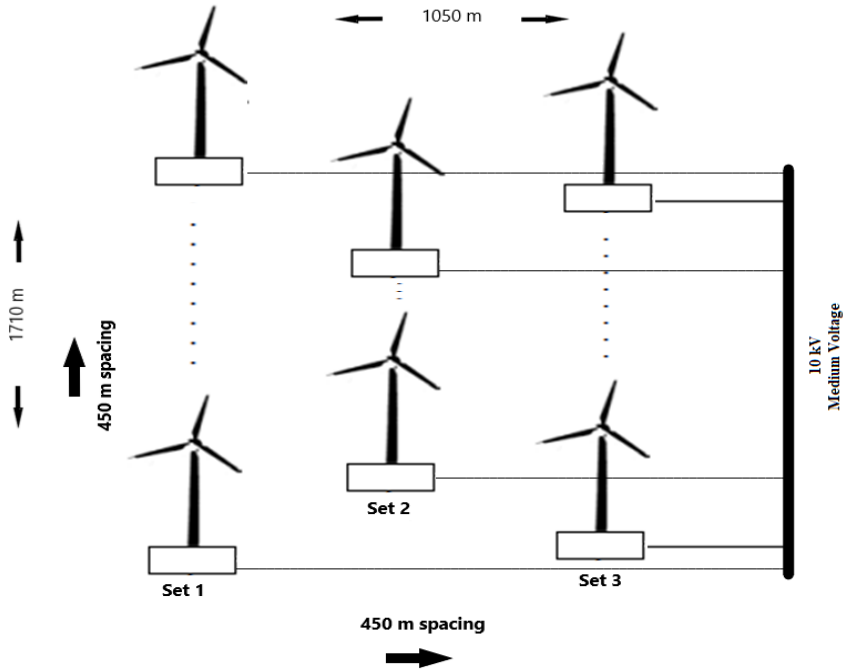

Figure 3.8: Wind farm scheme

3.4.3. Grid connection

The wind generators are linked to medium voltage lines (10 kV), a step-up transformer is used to match the output voltage with that of the medium voltage lines and allow grid connection. The total system has a rated power of 35 MW, but this is rarely maintained due to the fluctuations of irradiation levels and wind speeds. However, the system should undoubtedly improve the grid performance and eliminate power outages during peak demands.

3.5. Modelling of the System in MATLAB

The modelling is based on mathematical equations, it is often realized through Simulink mathematical blocks or through program files. There are a variety of predefined functions and blocks in Simulink library, therefore, some parts of the system were used directly from the Simulink library like the Phase lock loop, park's transformations and PI regulators.

3.5.1. Modelling of the PV system

3.5.1.1. PV generator

The PV array was modelled based on four equations that govern the output current [68]. These are listed below:

- Photo-current: $$I_{ph} = [I_{sc} + k_i.(T - 298)].\frac{G}{1000} \quad (3.1)$$

- Saturation current: $$I_0 = I_{rs}.\left(\frac{T}{T_n}\right)^3.\exp\left[\frac{q.E_{g0}.\left(\frac{1}{T_n} - \frac{1}{T}\right)}{n.K}\right] \quad (3.2)$$

- Reverse saturation current: $$I_{rs} = \frac{I_{sc}}{\exp\left(\frac{q.V_{oc}}{n.N_s.K.T}\right) - 1} \quad (3.3)$$

- Output current: $$I = I_{ph} - I_0.\left[\exp\left(q.\frac{(V + I.R_s)}{n.K.N_s.T}\right) - 1\right] - \frac{V + R_s.I}{R_p} \quad (3.4)$$

The monocrystalline Amerisolar AS-6M PV panel was picked thanks to its high efficiency of 18.04%, competitive price of 0.3 $\kW and good performance in hot climates. Moreover, monocrystalline solar cells proved better performance in desert climates then other types of solar cells according to M. Mosalam et al in his study [69]. The data sheet of the panel is provided in the appendix (Figure A.5) and the main specifications used in the modelling are given in Table A.1 in the appendix.

The calculation of the series and shunt resistances is detailed in [68], the same approach has been used to find R_p and R_s. The Simulink model is given in the figure below, where math functions were used to calculate the different currents. The inputs to the module are the irradiation and the temperature data, and the outputs

are the current and voltage. Gains are used to multiply the output current and voltage representing the number of modules connected in parallel and in series respectively.

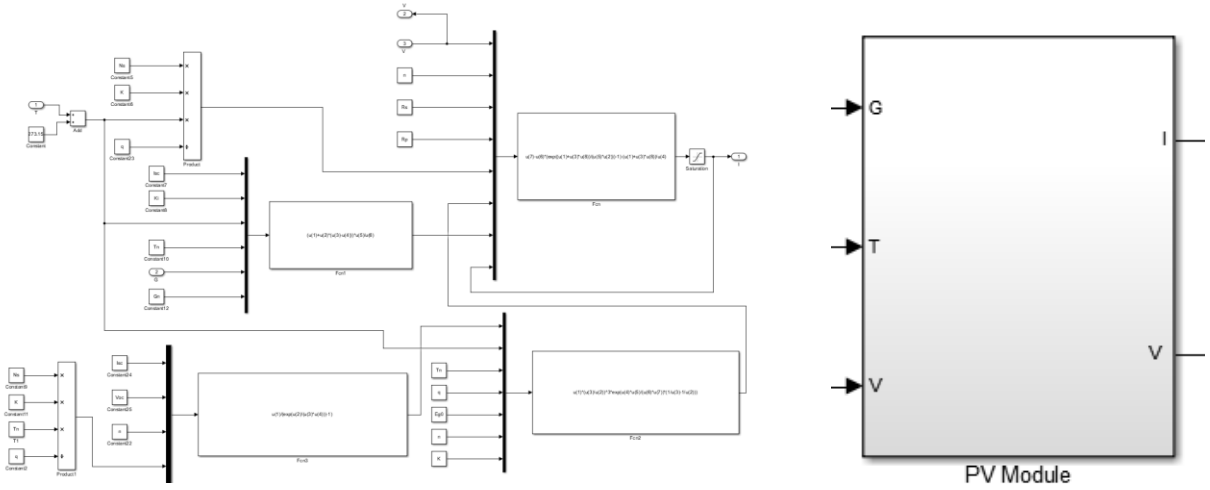

Figure 3.9: Simulink model of the PV module

3.5.1.2. Maximum power point control

In order to keep the PV generator working at maximum power, an MPPT tracker has been programmed in the model through a MATLAB file. Perturb and observe algorithm has been chosen, because of its precision and simplicity and ease of implementation. The hill climbing algorithm is based on the introduction of perturbations to the voltage and the observation of power output change. The signs of the last perturbation and the last power increment are used to decide the next perturbation, this continuous loop keeps the output power at its maximum. The output voltage of the array is injected directly to a DC-DC converter. Figure 3.10 shows the model of the MPPT tracker and the perturb and observe algorithm.

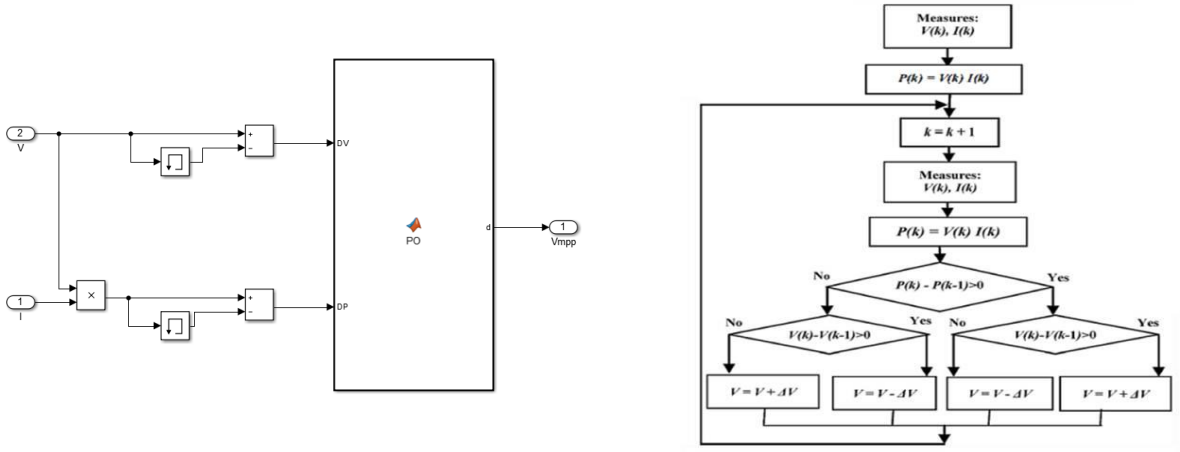

Figure 3.10: Perturb and observe MPPT tracker

3.5.1.3. DC-DC converter

The DC chopper that has been chosen for this system is a boost converter, the reason behind this choice is the high efficiency and robustness of this kind of converters and the advantage of stepping up the output. As an input, it receives the fluctuating DC output voltage of the PV array and converters it into a fixed stepped up DC voltage. The equivalent electrical circuit is shown in Figure 3.11 and the equations used for modelling are listed below [70]:

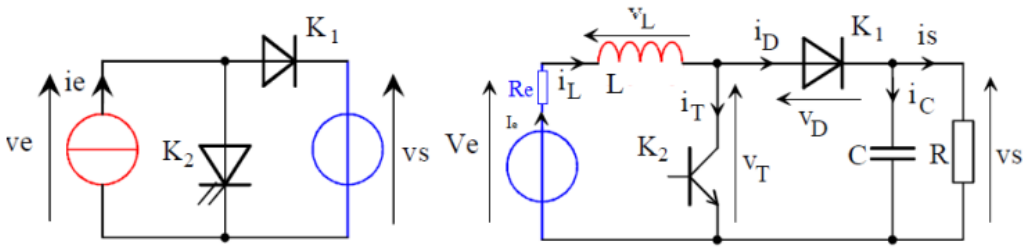

Figure 3.11: DC-DC boost converter [70]**.**

Loop 1:
$$L\frac{di_L}{dt} = V_e - V_c(1-\alpha) \tag{3.5}$$

Loop 2:
$$C\frac{dV_c}{dt} = i_L(1-\alpha) - \frac{V_c}{R} \tag{3.6}$$

Here, a represents the duty cycle obtained from the MPPT and used to generate the PWM (Pulse width modulation) signal which then controls the opening and closing of the switch (represented by K_2 in the circuit). The Simulink model is illustrated in Figure 3.12 and the values of the circuit elements have been determined previously in [70].

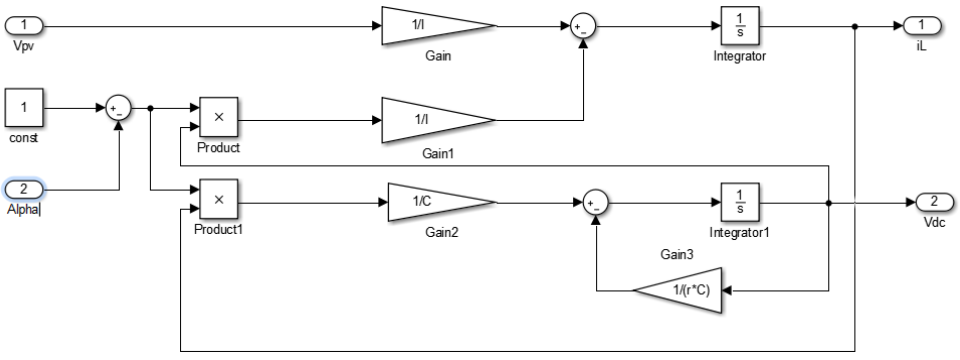

Figure 3.12: Simulink model of the boost converter

3.5.1.4. Three-phase inverter

The connection of the PV system to the AC bus is done via a voltage source inverter. The output of the boost converter is a fixed DC voltage, it is fed into a grid-tied three-phase inverter. Such inverters are used only in high power applications and their output is a three-phase voltage (Va, Vb and Vc), the latter is controlled by PWM signals. Pulse Width modulation is the process of changing the width of pulses in a pulse train in direct proportion to a small control signal. The electrical circuit of the inverter with the RL filter is shown in Figure 3.13 and the Simulink model is given in Figure 3.14.

Three-phase inverters can be controlled in three types of frames, the synchronous rotating frame (d-q), the stationary reference frame (α-β) and the natural frame (a-b-c). In d-q frame control, three-phase voltages and currents are transformed by Park's transformation into the d-q reference frame that rotates synchronously with the grid voltage. Thus, three-phase variables become DC quantities [71]. As the control variables are DC, different filtering methods can be used, and PI controller achieves good performance in this reference frame control. The model of the inverter determined by the following equations [71]:

a-b-c

$$V_{k0} = L\frac{di_k}{dt} + Ri_k + V_{gk} + V_{n0} \tag{3.7}$$

$$V_{n0} = \frac{1}{3}(V_{a0} + V_{b0} + V_{c0}) \tag{3.8}$$

$$V_{k0} = S_k\, V_{dc} = \begin{cases} V_{dc} & S_k = 1 \\ 0 & S_k = 0 \end{cases} \tag{3.9}$$

Where:

- k represents the phase of inverter, k ∈ {a, b, c}.
- *S* defines the state of upper switches.
- R is the equivalent filter series resistance.
- L is the value of the filter inductance.
- V_n is the voltage difference between neutral point of the grid and negative V_{dc}.

In each phase of the inverter, the two switches are supposed perfect and work simultaneously this allows us to write equation (3.10) and considering the voltages between a, b, c and the ground (0), we can express the model of the inverter by equation (3.11) [72]:

$$\begin{bmatrix} v_{a0} \\ v_{b0} \\ v_{c0} \end{bmatrix} = \frac{V_{dc}}{2} \times \begin{bmatrix} S_a \\ S_b \\ S_c \end{bmatrix} \tag{3.10}$$

$$\begin{bmatrix} v_a \\ v_b \\ v_c \end{bmatrix} = \frac{1}{3} \times \begin{bmatrix} 2 & -1 & -1 \\ -1 & 2 & -1 \\ -1 & -1 & 2 \end{bmatrix} \times \frac{V_{dc}}{2} \times \begin{bmatrix} S_a \\ S_b \\ S_c \end{bmatrix} \tag{3.11}$$

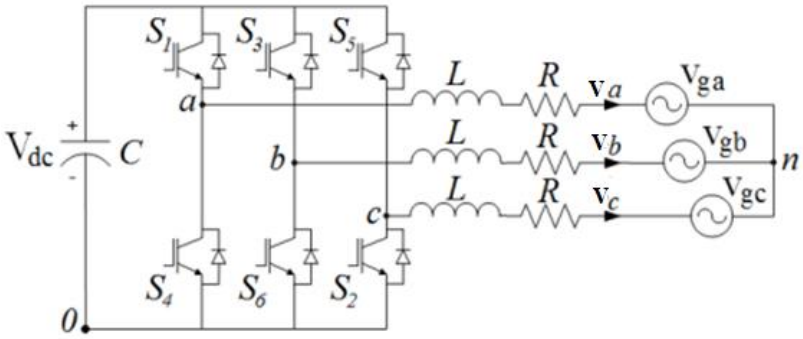

Figure 3.13: Equivalent electrical circuit of the three-phase inverter [71]**.**

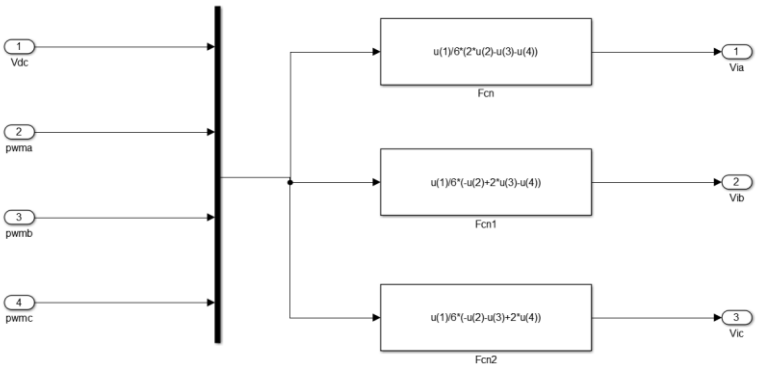

Figure 3.14: Simulink model of the three-phase inverter.

3.5.1.5. Phase lock loop

In order to control the inverter, the grid voltages are measured and used to determine the grid angle θ by means of PLL (phase lock loop). Esen et al, explains the PLL method in details in [71], Simulink has a predetermined PLL block that was used to generate the grid angle θ.

3.5.1.6. Park transformation

The grid angle is then used in Park's transformation to transform the grid voltages (Vga, Vgb and Vgc) from a-b-c reference frame to d-q frame which simplifies the control, the result is Vgd and Vgq (the d-q components of the grid voltages). Following the same transformation method, Vid and Viq (the d-q inverter components) are generated from the output voltages of the inverter. There is a dedicated block for Park's transformation in Simulink, and the transformation is given as follows [71]:

$$\begin{bmatrix} Vd \\ Vq \end{bmatrix} = \frac{2}{3} \begin{bmatrix} \cos\theta & \cos\left(\theta - \frac{2\pi}{3}\right) & \cos\left(\theta - \frac{4\pi}{3}\right) \\ -\sin\theta & -\sin\left(\theta - \frac{2\pi}{3}\right) & -\sin\left(\theta - \frac{4\pi}{3}\right) \end{bmatrix} \begin{bmatrix} V_a \\ V_b \\ V_c \end{bmatrix} \tag{3.12}$$

3.5.1.7. RL Filter

The d-q voltage components of both the inverter and the grid are used in a vector control mechanism implemented within an RL filter to generate active (P) and reactive (Q) powers. The control is modelled in Simulink as shown in Figure 3.15 and 3.16.

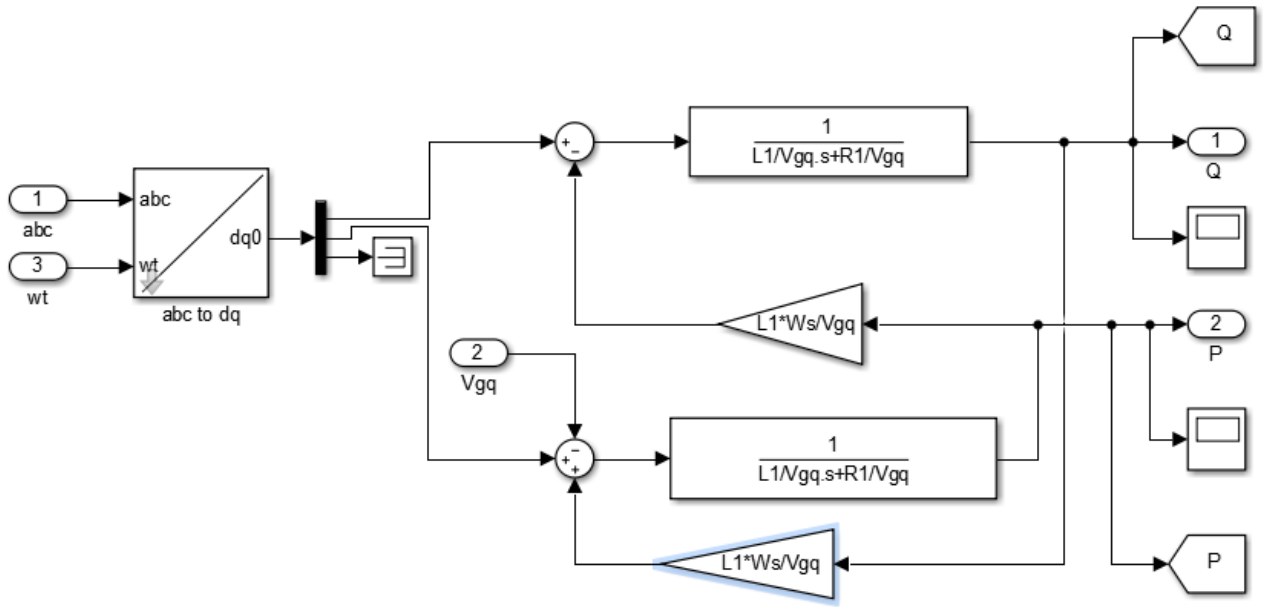

Figure 3.15: Simulink model of the RL filter.

The RL filter model, shown in Figure 3.15, is based on the following mathematical equations [73]:

a-b-c

$$V_a = -R_f . i_a - L_f \frac{di_a}{dt} + V_{ga} \quad (3.13)$$

$$V_b = -R_f . i_b - L_f \frac{di_b}{dt} + V_{gb} \quad (3.14)$$

$$V_c = -R_f . i_c - L_f \frac{di_c}{dt} + V_{gc} \quad (3.15)$$

d-q

$$V_d = -R_f . i_d - L_f \frac{di_d}{dt} + L_f \omega i_q + V_{gd} \quad (3.16)$$

$$V_q = -R_f . i_q - L_f \frac{di_q}{dt} - L_f \omega i_d + V_{gq} \quad (3.17)$$

Where:

- L_f represents the inductance of the filter.
- R_f is the resistance of the filter.

The RL filter is used to connect the inverter to the grid because they have different voltage amplitudes and different phases, it maintains a voltage difference between the grid and the inverter which allows power to flow towards the grid. In addition, the RL filter reduces the harmonics that are generated by the electronic components of the system. The measured active and reactive powers are then directly compared to reference values (P*) and (Q*), Q* is always set to zero to eliminate reactive power generation, this ensures zero phase angle between voltage and current leading to unity power factor. On the other hand, P* is set based on the output of the PV generator. The resulting errors are regulated by PI controllers and yield reference d-q inverter voltages (Vd* and Vq*). The PI controller gains are determined from the open and closed control loops through identification method. The control mechanism responsible for finding (Vd* and Vq*) was modelled in Simulink also and it is shown in the figure below:

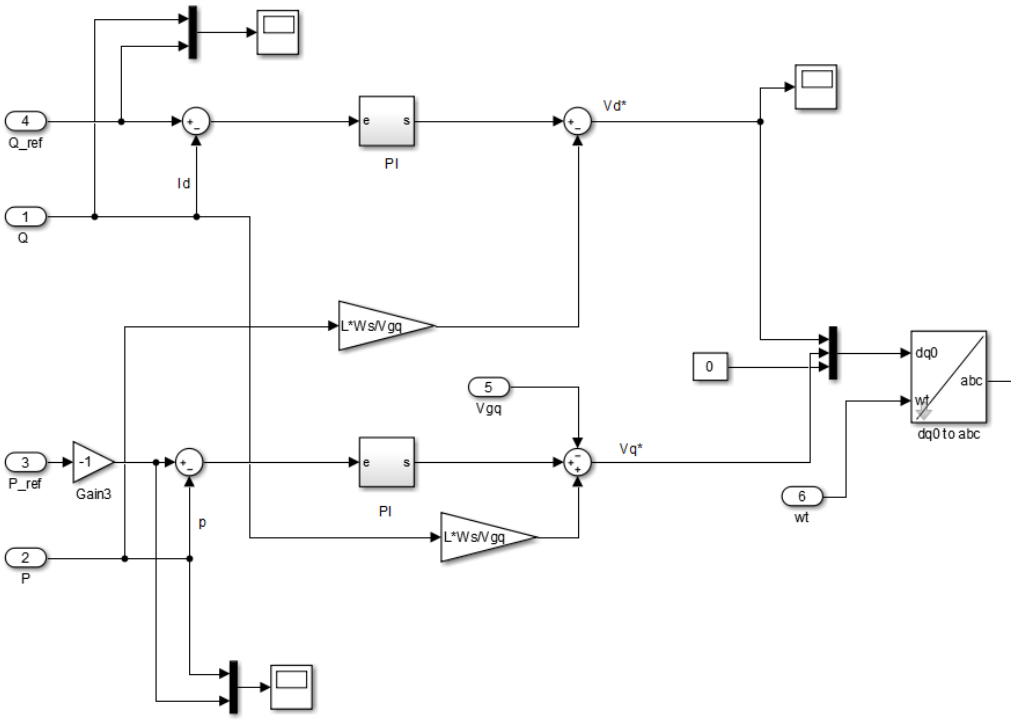

Figure 3.16: Simulink model of the inverter control

With the help of Park's inverse transformation, the obtained voltages are transformed back into three-phase reference inverter voltages (Va*, Vb* and Vc*) to be compared with a repetitive MATLAB sequence which in turn generates PWM signals that control the switches of the inverter. The PWM signals represent the state of the upper switches given in equation (3.9) above.

Park's inverse transformation, known as d-q to a-b-c transformation, exists also as predetermined Simulink block, and it is given by the following equation[71]:

$$\begin{bmatrix} V_a \\ V_b \\ V_c \end{bmatrix} = \begin{bmatrix} \cos(\theta) & -\sin(\theta) \\ \cos\left(\theta - \frac{2\pi}{3}\right) & -\sin\left(\theta - \frac{2\pi}{3}\right) \\ \cos\left(\theta - \frac{4\pi}{3}\right) & -\sin\left(\theta - \frac{4\pi}{3}\right) \end{bmatrix} \begin{bmatrix} V_d \\ V_q \end{bmatrix} \tag{3.18}$$

The PWM signal generation Simulink block is shown in Figure 3.17, where the three-phase voltage output is normalized and compared to a sequence repeating itself at a frequency of 5 kHz, the comparison generates the states of the upper switches of the inverter S_k.

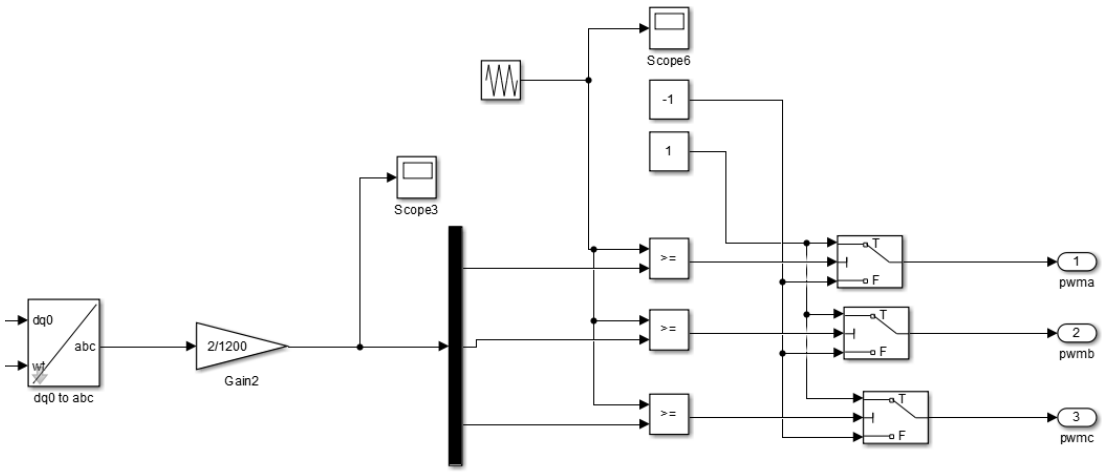

Figure 3.17: Simulink model of the PWM generation block

3.5.2. Modelling of the wind system

The wind system contains a set of wind turbines, these are divided into dynamic and mechanical models, in addition to the electrical model of a doubly fed induction generator linked to the turbine via a gearbox. The stator of the DFIG is directly connected to and synchronized with the grid, while the connection of the rotor is ensured by a back to back converter comprising a three-phase rectifier, a three-phase inverter, a DC bus in between, and an RL filter as seen in the figure below.

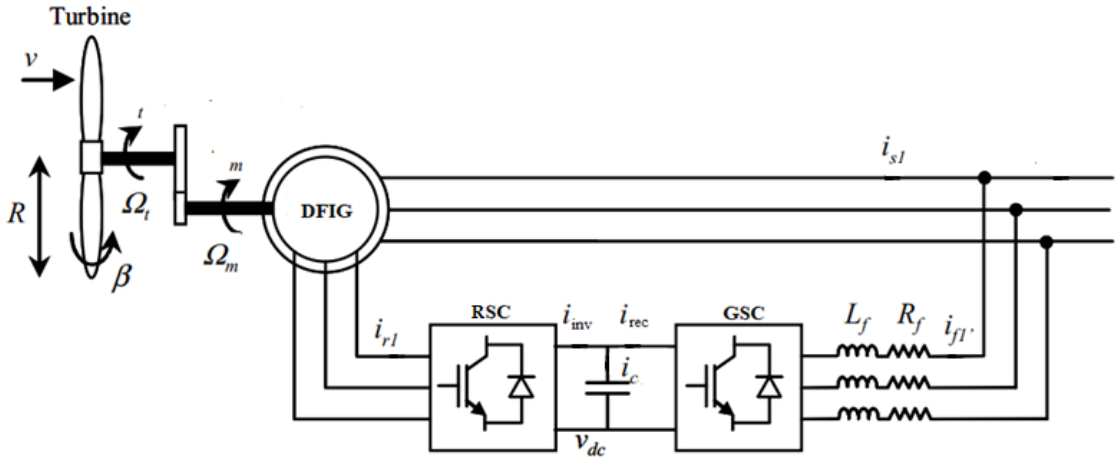

Figure 3.18: DFIG-based wind system [73]

In the following subsections, the generator will be modelled in Park's reference frame, and the vector control model of the RSC (Rotor-side converter) and GSC (Grid-side converter) will be presented.

3.5.2.1. Dynamic model of the wind turbine

As seen in the literature review, the mechanical power extracted from wind is characterized by the following equation:

$$P_t = \frac{1}{2}\rho Cp(\lambda,\beta)\pi R^2 V^3 \tag{3.19}$$

And the tip speed ratio is defined by:

$$\lambda = \frac{\Omega_t . R}{V} \tag{3.20}$$

The maximum power coefficient, on the other hand, is a function of λ and β and for a 3 MW wind turbine it is approximated by [73]:

$$C_p = C_1 \times \left(C_2 \times \frac{1}{\lambda_i} - C_3 \times \beta - C_4\right) \times \exp\left(-\frac{C_5}{\lambda_i}\right) + C_6 \times \lambda \tag{3.21}$$

Where:

$$\frac{1}{\lambda_i} = \frac{1}{\lambda + 0.08 \times \beta} - \frac{0.035}{\beta^3 + 1}$$

C_1	C_2	C_3	C_4	C_5	C_6
0.5176	116	0.4	5	21	0.0068

3.5.2.2. Mechanical model of the turbine

In order for the speed (Ω_m) of the generator to be evaluated, (T_m) and (T_t), the torques of the generator and the turbine respectively, are needed. The classical rotational dynamics equation (given below) delineates the behavior of the mechanical system.

$$\left(\frac{J_t}{G^2} + J_m\right)\frac{d\Omega_m}{dt} + f_v \times \Omega_m = T_t - T_m \tag{3.22}$$

Where:

- J_t and J_m are the turbine's and generator's moments of inertia.
- f_v is the generator's coefficient of friction.

Figure 3.19 shows the mechanical model where G represents the gearbox.

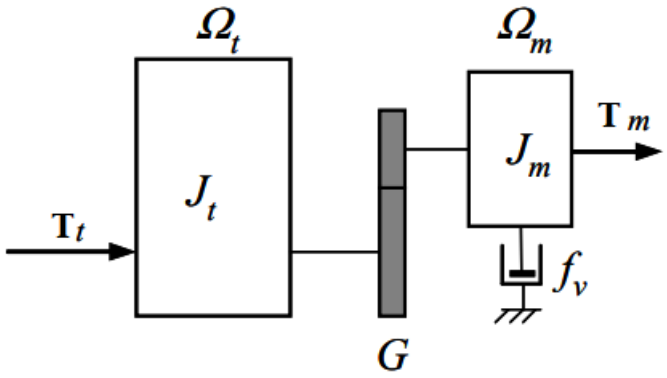

Figure 3.19: Mechanical model of the wind turbine [73]

3.5.2.3. MPPT control for the mechanical model

The MPPT technique relies on controlling the rotational speed of the generator to ensure maximum power extraction, this is achieved by imposing a reference torque on the machine. Thus, the TSR must be maintained at its optimal value (λ_{opt}) to maintain the power coefficient at it maximum value C_{pmax} as well. The MPPT technique is demonstrated in Figure 3.20 and the equivalent Simulink mechanical model is shown in Figure 3.21.

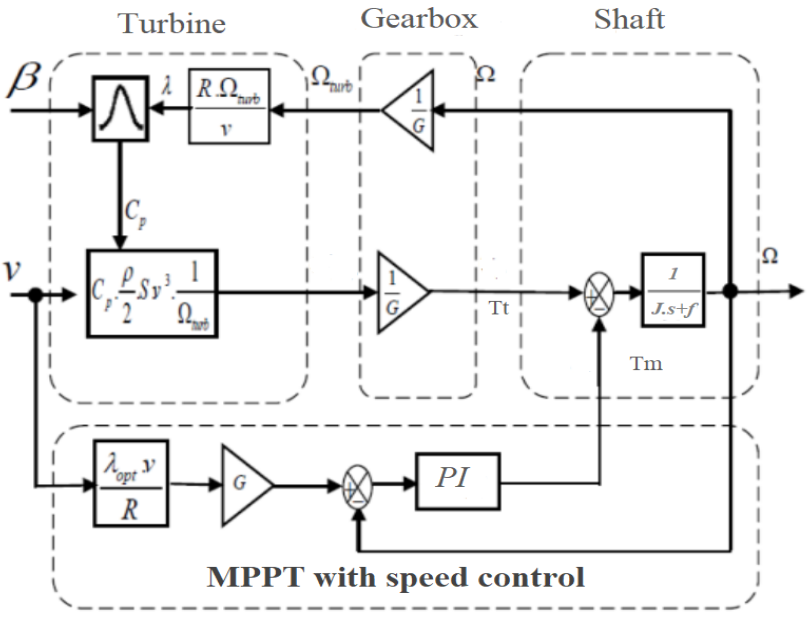

Figure 3.20: MPPT control mechanism [74]

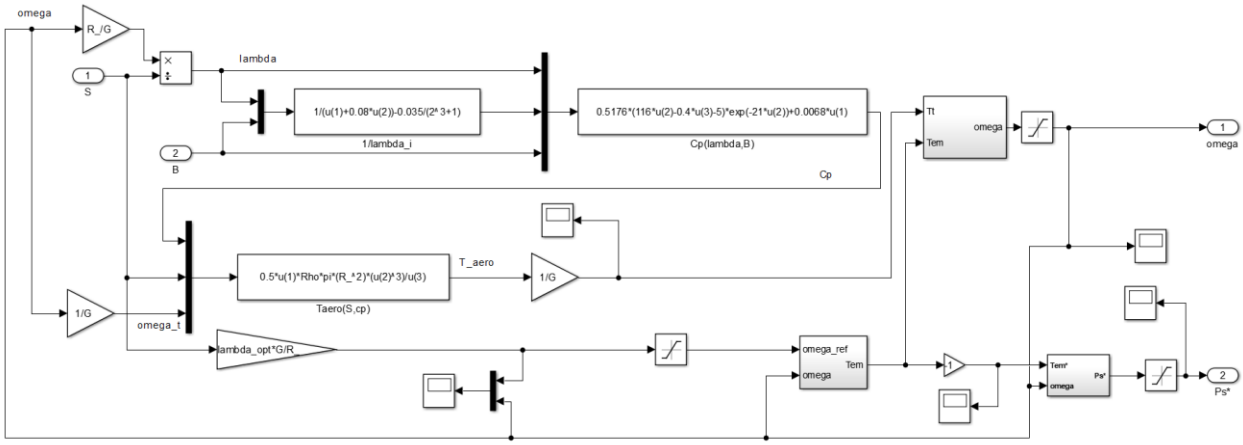

Figure 3.21: Equivalent Simulink mechanical model of the wind turbine

3.5.2.4. Model of the doubly fed induction generator

The DFIG is modelled in Park's reference frame to facilitate the implementation of the vector control method, the model described in [73] is simplified and so, the fluxes are additive and the inductances are constant with a mutual sinusoidal variation between the rotor and stator windings as a function of the electrical angle θ_e and their axes.

The equations governing the stator and rotor voltages in Park reference frame are given by [73] :

$$V_{sd} = R_s . i_{sd} + \frac{d\varphi_{sd}}{dt} - \dot{\theta_s} . \varphi_{sq} \tag{3.23}$$

$$V_{sq} = R_s . i_{sq} + \frac{d\varphi_{sq}}{dt} + \dot{\theta_s} . \varphi_{sd} \tag{3.24}$$

$$V_{rd} = R_r . i_{rd} + \frac{d\varphi_{rd}}{dt} - \dot{\theta_r} . \varphi_{rq} \tag{3.25}$$

$$V_{rq} = R_r . i_{rq} + \frac{d\varphi_{rq}}{dt} - \dot{\theta_r} . \varphi_{rd} \tag{3.26}$$

Where:

- V_{sd} and V_{sq} are the stator d-q voltages.
- V_{rd} and V_{rq} are the rotor d-q voltages.
- i_{sd} and i_{sq} are the stator d-q currents.
- i_{rd} and i_{rq} are the rotor d-q currents.
- φ_{sd} and φ_{sq} are the stator d-q fluxes.

- φ_{rd} and φ_{rq} are the rotor d-q fluxes.
- R_r and R_s are the rotor and stator resistances.
- θ_r and θ_s are rotor and stator angles.

The stator and rotor flux d-q components are given by:

$$\varphi_{sd} = L_s.i_{sd} + m.L_m.i_{rd} \quad (3.27)$$

$$\varphi_{sq} = L_s.i_{sq} + m.L_m.i_{rq} \quad (3.28)$$

$$\varphi_{rd} = L_r.i_{rd} + m.L_m.i_{sd} \quad (3.29)$$

$$\varphi_{rq} = L_r.i_{rq} + m.L_m.i_{sq} \quad (3.30)$$

$$L_s = L_{fs} + L_m \quad (3.31)$$

$$L_r = L_{fr} + m^2.L_m \quad (3.32)$$

Where:

- L_s is the stator cyclic inductance.
- L_r is the rotor cyclic inductance.
- $L_m$is the magnetising inductance.
- L_{fs} is the stator leakage inductance.
- L_{fr} is the rotor leakage inductance.
- m is the transformation ratio.

The electrical angle between the stator and rotor windings θ_e (see Figure 3.22), is given by:

$$\theta_s = \theta_e + \theta_r \quad (3.33)$$

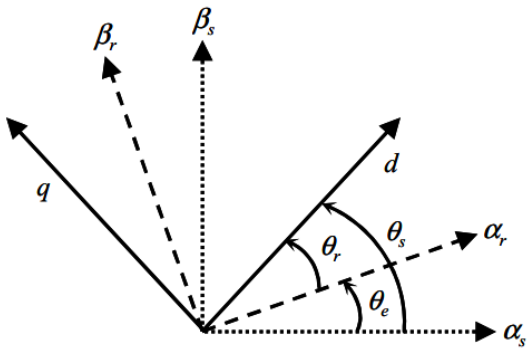

Figure 3.22: Park's angles [73]

The formulas to calculate the stator and rotor active and reactive powers are as follows:

$$P_S = V_{sd}.i_{sd} + V_{sq}.i_{sq} \tag{3.34}$$

$$Q_s = V_{sq}.i_{sd} - V_{sd}.i_{sq} \tag{3.35}$$

$$P_r = V_{rd}.i_{rd} + V_{rq}.i_{rq} \tag{3.36}$$

$$Q_r = V_{rq}.i_{rd} - V_{rd}.i_{rq} \tag{3.37}$$

The electromagnetic torque T_m can be expressed as:

$$T_m = p.(\varphi_{sd}.i_{sq} - \varphi_{sq}.i_{sd}) \tag{3.38}$$

$$T_m = p.\frac{m.L_m}{L_s}.(\varphi_{sq}.i_{rd} - \varphi_{sd}.i_{rq}) \tag{3.39}$$

Where p represents the number of pole pairs.

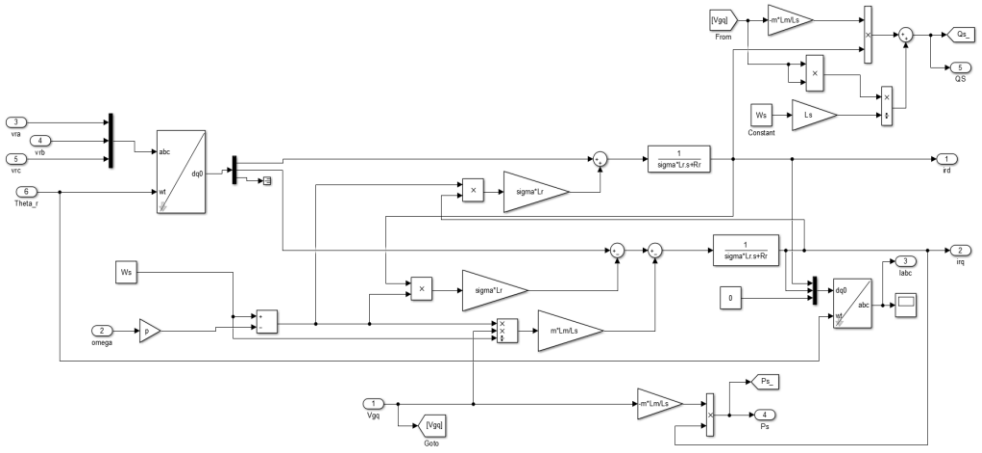

Figure 3.23: DFIG Simulink model

3.5.2.5. DFIG Control

By neglecting the resistances of the stator windings, the simplified model of the DFIG in the d-q reference frame is obtained as:

$$V_{sd} = 0 \tag{3.40}$$

$$V_{sq} = U_s = \omega_s . \varphi_{sd} \tag{3.41}$$

$$V_{rd} = R_r . i_{rd} + \frac{d\varphi_{rd}}{dt} - \omega_r . \varphi_{rq} \tag{3.42}$$

$$V_{rq} = R_r . i_{rq} + \frac{d\varphi_{rq}}{dt} - \omega_r . \varphi_{rd} \tag{3.43}$$

The stator currents are obtained from the stator and rotor flux equations as:

$$i_{sd} = \frac{\varphi_{sd} - m . L_m . i_{rd}}{L_s} \tag{3.44}$$

$$i_{sq} = -m . \frac{L_m}{L_s} . i_{rq} \tag{3.45}$$

Thus, rotor flux equations become as the following:

$$\varphi_{rd} = \left(L_r - \frac{(m . L_m)^2}{L_s} \right) . i_{rd} + m . \frac{L_m}{L_s} . \varphi_{sd} = \sigma . L_r . i_{rd} + m . \frac{L_m}{L_s} . \varphi_{sd} \tag{3.46}$$

$$\varphi_{rq} = L_r . i_{rq} - \frac{(m . L_m)^2}{L_s} . i_{rq} = \sigma . L_r . i_{rq} \tag{3.47}$$

With σ being the leakage coefficient:

$$\sigma = 1 - \frac{(m . L_m)^2}{L_s . L_r} \tag{3.48}$$

By replacing the direct and quadrature components of the rotor fluxes we obtain:

$$v_{rd} = R_r . i_{rd} + \sigma . L_r \frac{di_{rd}}{dt} + e_{rd} \tag{3.49}$$

$$v_{rq} = R_r . i_{rq} + \sigma . L_r \frac{di_{rq}}{dt} + e_{rq} + e_{\varphi} \tag{3.50}$$

Where:

$$e_{rd} = -\sigma . L_r . \omega_r . i_{rq}$$

$$e_{rq} = \sigma . L_r . \omega_r . i_{rd}$$

$$e_{\varphi} = \omega_r . m . \frac{L_m}{L_s} . \varphi_{sd}$$

The electromagnetic torque becomes :

$$T_m = -p . \frac{m . L_m}{L_s} . \varphi_{sd} . i_{rq} \tag{3.51}$$

Hense, the active and reactive powers are expressed as:

$$P_S = -v_{sq} . m . \frac{L_m}{L_s} . i_{rq} \tag{3.52}$$

$$Q_S = \frac{v_{sq} . \varphi_{sd}}{L_s} - v_{sq} . m . \frac{L_m}{L_s} . i_{rd} \tag{3.53}$$

From these expressions it is obvious that the choice of the d-q frame makes power produced from stator proportional to the rotor q current component, while the reactive power is not proportional to the rotor d current component. This implies that independent control of the stator active and reactive power is possible through the rotor d-q current components. For controlling the rotor d-q current components, reference d-q rotor currents are needed. These are obtained from the stator flux, which is estimated by the following formula:

$$\varphi_{sd-est} = L_s . i_{sd} + m . L_m . i_{rd} \tag{3.54}$$

The reference rotor current components are then generated as follows:

$$i_{rq}^* = -\frac{L_s}{p . m . L_m . \varphi_{sd-est}} . T_m^* \tag{3.55}$$

$$i_{rd}^* = \frac{\varphi_{sd-est}}{m . L_m} - \frac{L_s}{m . L_m . v_{sq}} . Q_s^* \tag{3.56}$$

The control of the DFIG, ensured by the rotor side converter (RSC), is modelled in Simulink as Figure 3.24 illustrates.

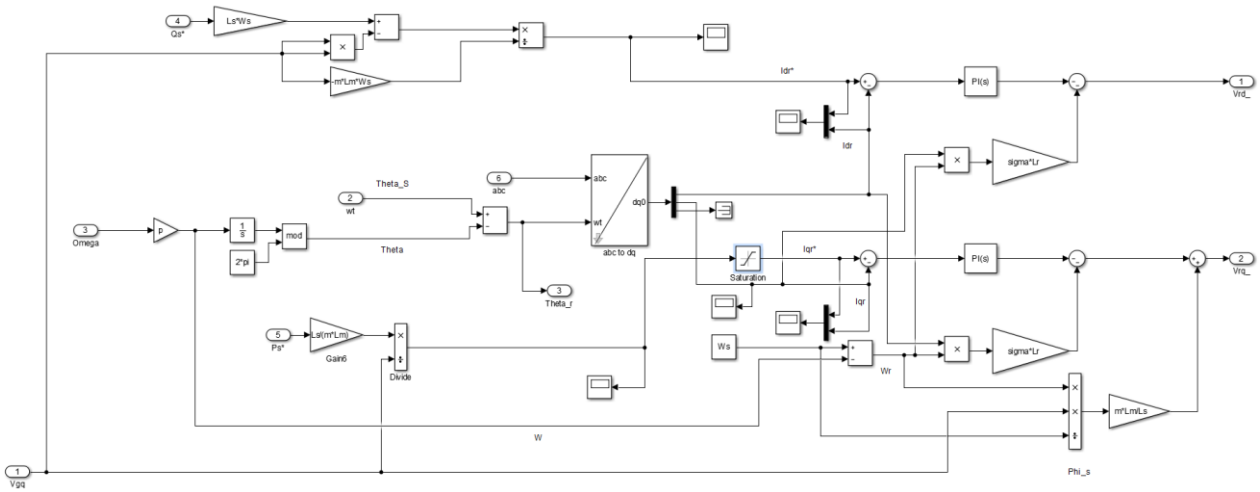

Figure 3.24: Simulink model of the DFIG control.

The output voltages are then used to generate the PWM signal which controls the converter.

3.5.2.6. Filter and grid side converter (GSC)

As presented in Figure 3.25, the GSC is linked to the grid through an RL filter, it allows the control of the DC bus voltage and the reactive power injected to the grid. Unity power factor is ensured by setting the reactive power to zero (Q=0).

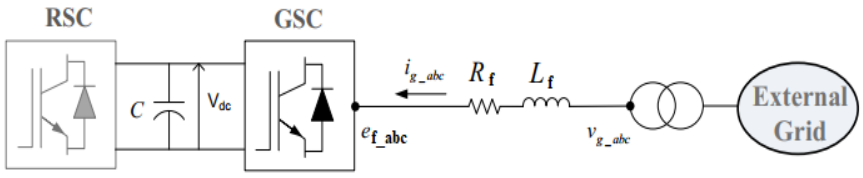

Figure 3.25: Connection between the back to back converter and the grid

The three-phase equations of the grid-side circuit can be found as:

$$v_{ga} = R_f . i_{ga} + L_f \frac{di_{ga}}{dt} + e_{fa} \tag{3.57}$$

$$v_{gb} = R_f . i_{gb} + L_f \frac{di_{gb}}{dt} + e_{fb} \tag{3.58}$$

$$v_{gc} = R_f . i_{gc} + L_f \frac{di_{gc}}{dt} + e_{fc} \tag{3.59}$$

Transforming the equations to the synchronous rotating frame, the d-q representation can be derived as:

$$v_{fd} = -R_f . i_{fd} - L_f \frac{di_{fd}}{dt} + e_{fd} \quad (3.60)$$

$$v_{fq} = -R_f . i_{fq} - L_f \frac{di_{fq}}{dt} - e_{fq} \quad (3.61)$$

Where:

$$e_{fd} = \omega_s . L_f . i_{fq} \quad (3.62)$$

$$e_{fq} = -\omega_s . L_f . i_{fd} + v_{gq} \quad (3.63)$$

The GSC allows the control of the RL filter currents i_{fd} and i_{fq} independently, the latter is done by PI controls based on the reference value i_{fd}* and i_{fq}*. Knowing that the active and reactive powers from the GSC are given by:

$$P_f = V_{fd} . I_{fd} + V_{fq} . I_{fq} \quad (3.64)$$

$$Q_f = V_{fq} . I_{fd} + V_{fd} . I_{fq} \quad (3.65)$$

And by neglecting the losses due to the RL filter resistance while considering that the voltage vector is aligned with the q-axis of the synchronous rotating frame. Hence, the d-q voltage components are:

$$v_{sd} = 0, v_{sq} = \widehat{v_g}.$$

The active and reactive powers become:

$$P_f = V_{sq} . I_{fq} \quad (3.66)$$

$$Q_f = V_{sq} . I_{fd} \quad (3.67)$$

Thus, the reference active and reactive powers are given as:

$$P_f^* = I_{fq}^* . V_{sq} \quad (3.68)$$

$$Q_f^* = I_{fd}^* . V_{sq} \quad (3.69)$$

The power in the DC bus is divided into:

$$P_{RSC} = V_{dc} . I_{RSC} \quad (3.70)$$

$$P_C = V_{dc} . I_c \quad (3.71)$$

$$P_{GSC} = V_{dc} . I_{GSC} \quad (3.72)$$

And the three powers are linked by the following equation:

$$P_{RSC} = P_c + P_{GSC} \tag{3.73}$$

By neglecting power losses due to the joule effect in the capacitor, the converters and the RL filter, P_{RSC} and P_f becomes equal, and hence controlling P_f means controlling P_c which also translates into controlling the DC bus voltage (V_{dc}).

As seen in the GSC Simulink model (Figure 3.26), the dc-link voltage is controlled by the rotor q current component.

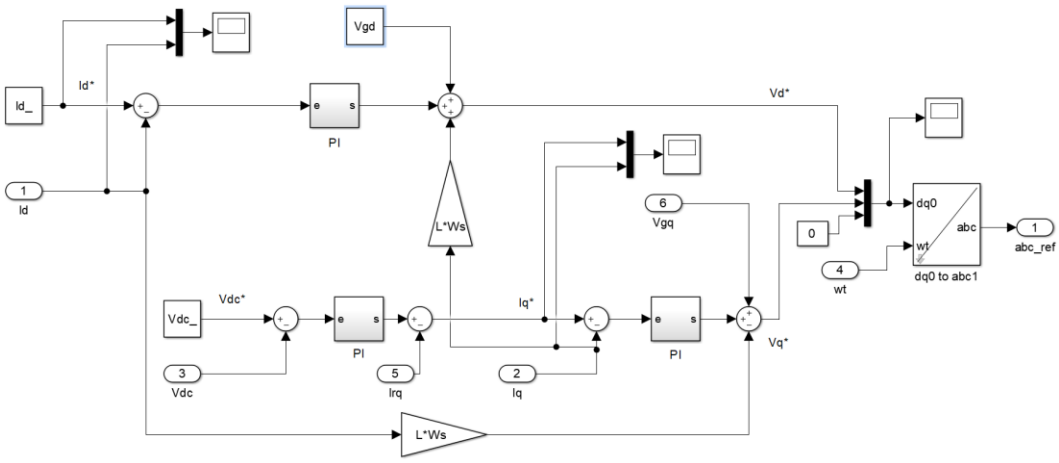

Figure 3.26: Simulink model of the GSC control.

3.6. Simulation of the system

To evaluate the performance and see how much power can be extracted, the system is simulated for two specific months using hourly data that was generated by METEONORM. The result is hourly power output and is to be compared to hourly power production of the central power plant of Adrar. The inputs to the PV system are global horizontal irradiation, direct normal irradiation, diffuse horizontal irradiation and the number of hours. The outputs are active and reactive powers. On the other hand, the wind system receives hourly wind speeds, and outputs active and reactive powers as well.

3.6.1. PV cell temperature

PV modules are rated under STC conditions, but in real life situations the cell temperature is never 25 °C, and irradiance is always less than 1000 W/m². The cell temperature depends on the solar irradiance, ambient temperature and the nominal operating condition temperature (NOCT) as expressed by the following equation [75]:

$$T_{cell} = T_{air} + \frac{NOCT - 20}{80} \times S \tag{3.74}$$

Where the NOCT is given by the PV manufacturer and S represents irradiance in (mW/cm²).

A Simulink block has been dedicated to compute the PV cell temperature based on the previous equation, this should allow the modelled PV system to be as close to real life situations as possible.

3.6.2. Solar irradiance on the PV generator

The solar irradiance G_m on the PV module is given by:

$$G_m = G_m^{dir} + G_m^{dif} + G_m^{ground} \tag{3.75}$$

Where G_m^{dir} is the direct irradiance on a module, for cases of no shading and soiling, given by [76]:

$$G_m^{dir} = I_e^{dir} \cos\gamma \tag{3.76}$$

Where

- $I_e^{dir} = DNI$ (Direct Normal Irradiance).
- γ is the angle of incidence of solar irradiance onto the module, expressed as [77]:

$$\cos\gamma = \cos\alpha \cos(\emptyset_s - \emptyset_m) \sin\theta_m + \sin\alpha \cos\theta_m \tag{3.77}$$

- α Altitude angle of the sun.

- $\emptyset_s$ Solar azimuth angle.
- $\emptyset_m$ Solar module azimuth angle.
- θ_m Solar module tilt angle.
- n Number of days from the beginning of the year.

G_m^{ground} is the received radiation by the module that is reflected from the ground and is given by:

$$G_m^{ground} = GHI \times \rho \times (1 - SVF) \tag{3.78}$$

Where GHI is the global horizontal irradiance, expressed as:

$$GHI = DNI \times \cos\theta_z + DHI \tag{3.79}$$

DNI and DHI can be measured in meteorological stations with a pyrheliometer and a pyranometer, respectively.

- ρ albedo of the ground usually provided in the weather data file ($\alpha \approx 0.2$).
- θ_z Solar zenith angle.

SVF sky view factor, which is the portion of the sky from which the module can receive diffuse radiation dependent of module tilt angle θ_m, and it is given by [78]:

$$SVF = \frac{1 + \cos\theta_m}{2} \tag{3.80}$$

G_m^{dif} is the diffuse component of solar irradiance on a module and is proportional to the SVF [77].

$$G_m^{dif} = C \times DHI \times SVF \tag{3.81}$$

Where (C) is the sky diffuse factor expressed as:

$$C = 0.095 + 0.04 \sin\left[\frac{360}{365}(n - 100)\right] \tag{3.82}$$

3.6.2.1. Solar geometry

The solar azimuth angle ϕ_s is measured from the North, where it is 0° through East to 360° and can be calculated at a specific latitude using the following expressions [79].

$$\text{Cos}\,\emptyset_s' = \frac{\cos\emptyset\sin\delta - \cos\delta\sin\emptyset\cos\omega}{\cos\alpha} \tag{3.83}$$

Where if $\omega \leq 0$ then $\emptyset_s = \emptyset_s'$. Otherwise, $\emptyset_s = 360 - \emptyset_s'$.

The zenith angle θ_z is expressed as:

$$\cos\theta_z = \sin\emptyset\sin\delta + \cos\emptyset\cos\delta\cos\omega \tag{3.84}$$

Where α is the solar altitude, expressed as [80]:

$$\sin\alpha = \sin\delta\sin\emptyset + \cos\delta\cos\emptyset\cos\omega \tag{3.85}$$

- δ is the sun declination angle expressed as:

$$\delta = 23.45° \sin\left[\frac{360}{365}(n-80)\right] \tag{3.86}$$

- ω is the hour angle expressed as:

$$\omega = 15(t-12)^{\circ} \tag{3.87}$$

Where t is the solar time in 24 hour clock expressed as follows [81]:

$$t = UT + ET \pm 4(L_{st} - L_{loc}) + C \tag{3.88}$$

Where:

- L_{loc}, Longitude of the location under consideration.
- L_{st}, Standard meridian for the local time zone. The meridians used for reckoning standard time are though that whose longitude is exactly divisible by 15°.
- C, Daylight savings time correction, it is equal to zero if there is no daylight saving, otherwise C is equal to the number of hours that the time is advanced for daylight saving.
- UT, Universal Time (standard time) expressed as:

$$UT = t_{local} - t_{offset} \tag{3.89}$$

- t_{local}, Local time of the location in 24-hour clock.
- t_{offset}, Time difference between Greenwich time and location time.
- ET, Equation of time, the correction for time difference (minutes) between solar time and local clock time, and it is expressed as [81]:

$$ET = 229.2(0.000075 + 0.001868\cos B - 0.032077\sin B - 0.014615\cos 2B - 0.04089\sin 2B) \tag{3.90}$$

$$B = (n-1)\frac{360}{365} \tag{3.91}$$

Where n represents the day of the year.

To determine the local time of sunrise and sunset at the latitude $\emptyset$ and sun declination angle δ, the following expression is used:

$\cos\omega = -\tan\emptyset\tan\delta$ for $-180° < \omega < 0°$ for sunrise and $0° < \omega < 180°$ for sunset.

For the simulation, a MATLAB algorithm was programmed to calculate the irradiance received by the PV module whilst considering the conditions and equations mentions above. The program is attached to the appendix (Figure A.6).

3.6.3. Wind speed at hub height

The output of the wind turbine depends on the wind speed at the machine's hub height, the latter is calculated from hourly wind speed using [82]:

$$V_{hub\_h} = v\frac{\ln\left(\frac{Z_{hub}}{Z_0}\right)}{\ln\left(\frac{Z_{data}}{Z_0}\right)} \tag{3.92}$$

Where Z_{hub}(m) represents the hub height of the turbine, Z_{data} is the height at which the wind speed is measured, Z_0 is the surface roughness length and v is the wind speed.

Adrar is mostly a desert, and hence, it falls under the category of open flat terrain with few to no obstacles. According to [83] , this translates into Z_0 = 0.03 m. The figure below shows the Simulink model that was used to calculate the wind speed at hub height. The input is wind speed data measured at 10 meters.

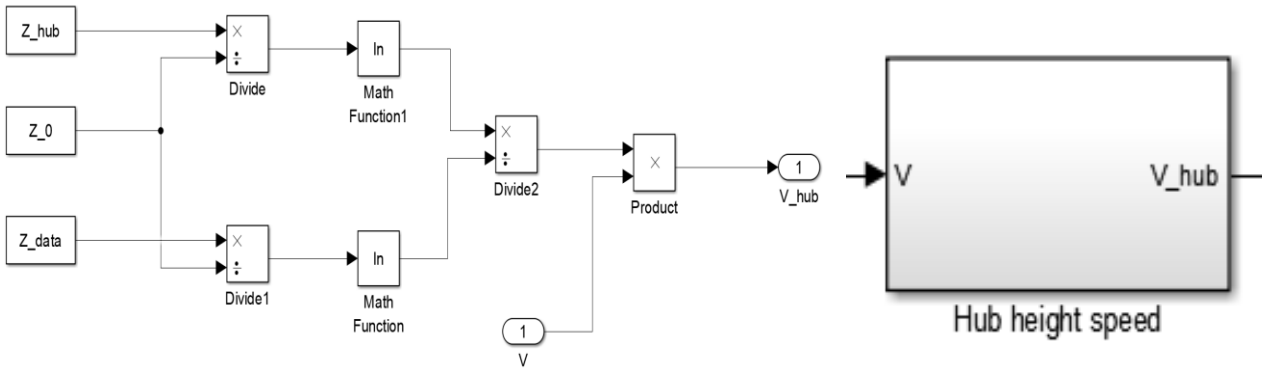

Figure 3.29: Hub height wind speed calculation model

3.7. Economic and Environmental Analysis

In this study, the hybrid system is of large scale and injects power directly to the grid. Such systems have very high initial investments but pay off in the long run. The size of the system is important in determining the feasibility and cost effectiveness of the whole project. In general, the cost of any system is composed of capital costs, replacement costs and operating and maintenance costs.

3.7.1. Main costs of the system

The capital cost is fixed and includes the prices for components of the system, transportation, packaging, installation, etc. It is calculated by the following formula [84]:

$$Capital\ cost = (1 + K).N.C \tag{3.93}$$

Where:

- C is the cost of one component (PV panel, wind turbine, etc.).
- K is the cost related to engineering, logistics, installation, etc.
- N is the number of components (100 PV panels, 30 converters, etc.).

On the other hand, the replacement and operating and maintenance costs are known as variable costs. The operating and maintenance costs include the expenses of insurance, salary of operators, taxes, recurring costs and maintenance. They are expressed as a percentage of the initial capital cost. The replacement costs are the expenses needed to change components as these have different lifetimes and some of them requires to be replaced a number of times during the lifespan of the system.

3.7.2. Levelized cost of electricity

When conducting economic analyses of energy systems, the levelized cost of electricity is usually the main factor used for judging the feasibility of a system. The latter is defined as the cost of generated energy units during the lifespan of the selected system. As given in equation 3.82, The LCOE is calculated summing the capital costs and operating and maintenance costs and dividing by the total energy generated from the system. The net present value approach is used for the calculation of the LCOE. In this method, the total expenses and the incomes of the system are determined based on discounting from a starting date [85].

$$LCOE = \frac{I_0 + \sum_{t=1}^{n} \frac{A_t}{(1+i)^t}}{\sum_{t=1}^{n} \frac{M_{t,el}}{(1+i)^t}} \quad (3.94)$$

Where:

- $LCOE$: Levelized cost of electricity ($/kWh).
- I_0: Investment expenditures ($).
- A_t: Annual total costs ($) in year t.
- $M_{t,el}$: Produced quantity of electricity (kWh) in the respective year.
- i: Real interest rate in %.
- n: Economic operational lifetime in years.
- t: Year of lifetime (1, 2, …, n).

3.7.3. The net present value

The net present value (NPV) is a measure of the net profit plus the actual value of the project, it is calculated by subtracting the cash outflows (including initial cost) from the actual values of cash inflows over a period of time. The NPV includes all benefits and cost streams occurring at different points in time and converts them into present value equivalents. The total of these values gives the overall worth of the project. the NPV is given by the following formula [85]:

$$NPV = \sum_{t=1}^{n} \frac{R_t - C_t}{(1+i)^t} - I_0 \quad (3.95)$$

Where:

- R_t is the revenue in year t.
- C_t represents the costs in year t.
- i is the discount rate.
- I_0 is the initial investment.

3.7.4. The payback period

The payback time is the time needed to amortize the initial investment through cash inflows of a project, the shorter the payback time the quicker the recovery of the investment funds. However, the distribution of cash flow is not considered beyond the payback period. The payback time is calculated by the following equation [85]:

$$Payback\ period = \frac{Initial\ Investment}{cash\ inflow\ per\ period} \tag{3.96}$$

3.7.5. System model in HOMER

The same system that was modelled in MATLAB has been modelled again in HOMER so as to perform an economic and environmental analysis. No load has been added to the system, since the latter injects all its power into the grid. Thus, all produced electricity will be sold to the utility. The different system components are shown with the respective costs in Figure 3.28 and a summary of all the costs is given in Table 3.2.

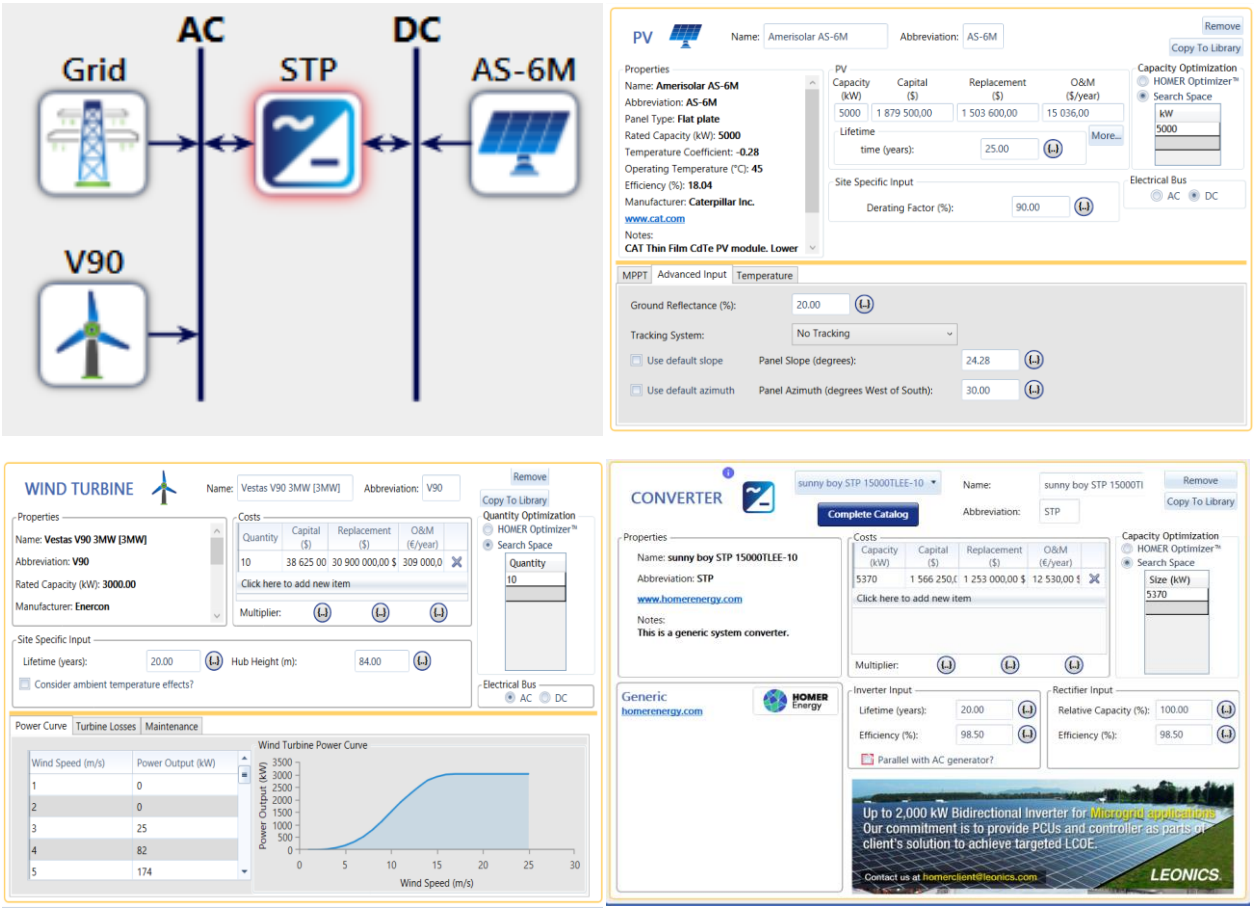

Figure 3.28: HOMER model of the hybrid system

Table 3.2: Summary of the system costs

Component	Capital cost ($)	Replacement cost ($)	OMC (%)
PV panel (AS-6M)	132	105	1
Wind turbine (Vestas V90)	3862500	3090000	1
DC/AC converter (Sunny boy STP 15000)	4375	3500	1

The cost of engineering, logistics and installation (K) has been estimated at 25% of the component's cost, and the operating and maintenance cost is chosen as 1% of the capital cost of the system. The interest rate in 2018 is at 3.75% while the inflation rate is evaluated at 3.41% [86]. Moreover, the recent electricity price in Algeria is fixed at 0.038 $/kWh [87], while electricity producers using solar and wind energies benefit from a premium of 300% of the market price of electricity, this is ensured for the full project lifetime according to law "No.° 02-01 du 22 Dhou El Kaada 1422 (Articles 88 ff)" [88].

For the environmental analysis under HOMER, the amount of sulfur dioxide and nitrogen oxides emitted by a combined cycle power plant using natural gas have been chosen as 2.74 kg/MWh and 1.34 kg/MWh (see Figure 3.29 below), while the amount of CO2 is much higher than the other two gases with a value of 400 kg/MWh [89].

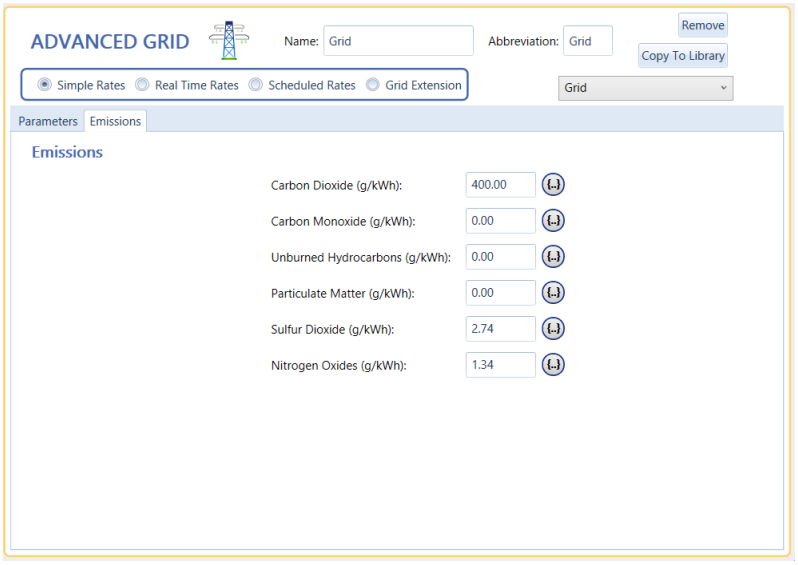

Figure 3.29: Emissions from conventional power plants

CHAPTER FOUR: RESULTS AND DISCUSSION

Outline

4.1. Introduction

In this chapter, the different results obtained from the simulation of the modelled system are presented. The performance of the control is presented along with the energy output of the PV plant and the wind farm. An analysis of the amount of power injected to the grid and the contribution of the hybrid system is conducted. The chapter ends with an economic and environmental analysis of the project.

4.2. The PV System

The performance output of the PV system is affected mainly by the cell's temperature and the irradiation received by the PV generator. Since cell temperature is proportional to ambient temperature, an increase in the latter means a decrease in performance of the PV system, and hence a lower efficiency.

4.2.1. PV cell temperature

Based on the available dry bulb temperature data, the trend of cell temperature levels in the month of January shows slight variations. Peak levels vary each day with a maximum of 52 °C at the beginning and at the end of the month, and a minimum of 41 °C is noticed around mid-January. Figure 4.1 shows hourly variations of cell temperature in January versus that in August where the x-axis represents the number of hours and the y-axis represents the temperature in degrees Celsius.

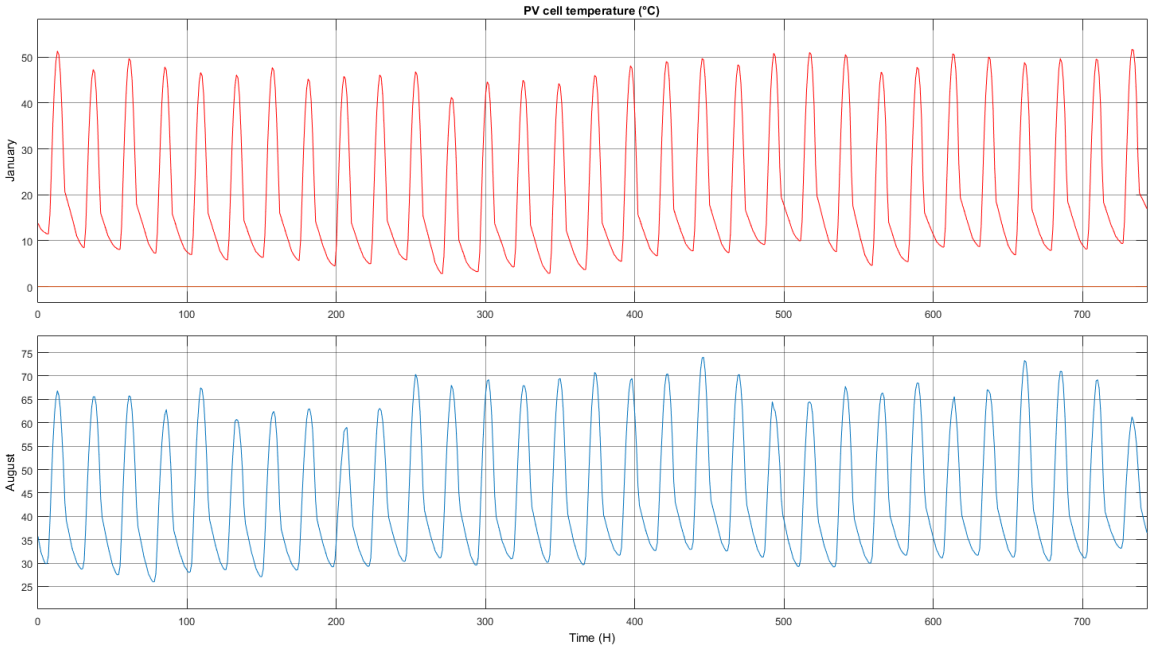

Figure 4.1: PV cell temperature variations (January vs August)

August tells a different story. PV cell temperature levels are quite high maintaining an average of 48 °C. The peak is reached between 2 pm and 4 pm each day as seen in the figure, and ranges between 58 and 74°C this time of the year. Such high temperatures yield a noticeable decrease in the PV output but remains manageable and within the operating temperature range of the chosen panel.

4.2.2. Solar irradiance received by the PV generator

Although ambient temperatures in January are significantly low, the irradiation received by the module is unpredictably high (see Figure 4.2). Minimum radiation levels of around 850W/m² are observed in first and last days of January, this can be attributed to the solar position throughout the year as the distance between the earth and the sun varies and leads to variation of extraterrestrial radiation flux [24].

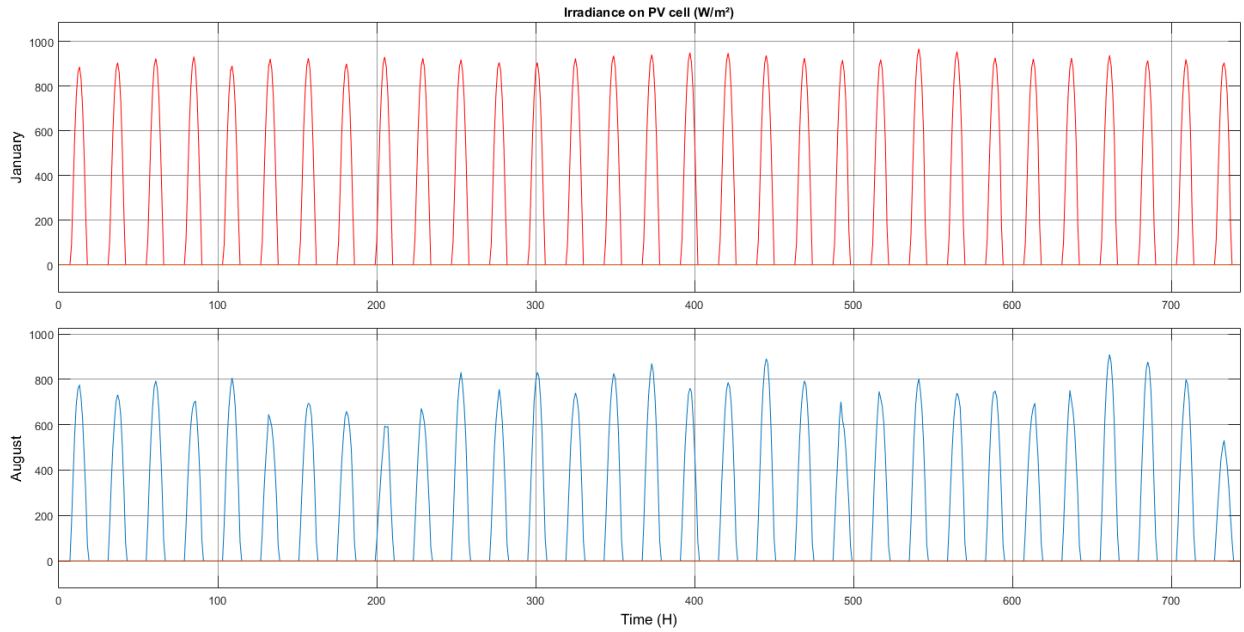

Figure 4.2: Irradiance received by the PV modules (January vs August)

Irradiation levels in August are considerably low compared to January, they barely reach 800 W/m² in most days of the month. Although, a slight increase in irradiation levels is observed in mid-August and towards the end of the month as the graph above shows, it still remains low compared to January. Low irradiation coupled with high temperatures will dramatical reduce the PV output.

4.2.3. MPPT control performance

The perturb and observe algorithm keeps the voltage output of the PV module at its maximum value, the accuracy is determined by the size of the perturbation (ΔV) and thus the output keeps oscillating around the maximum value as demonstrated by Figure 4.3. It is worth mentioning that the MPPT tracker is fast, and the maximum power point is quickly reached, hence the control works perfectly.

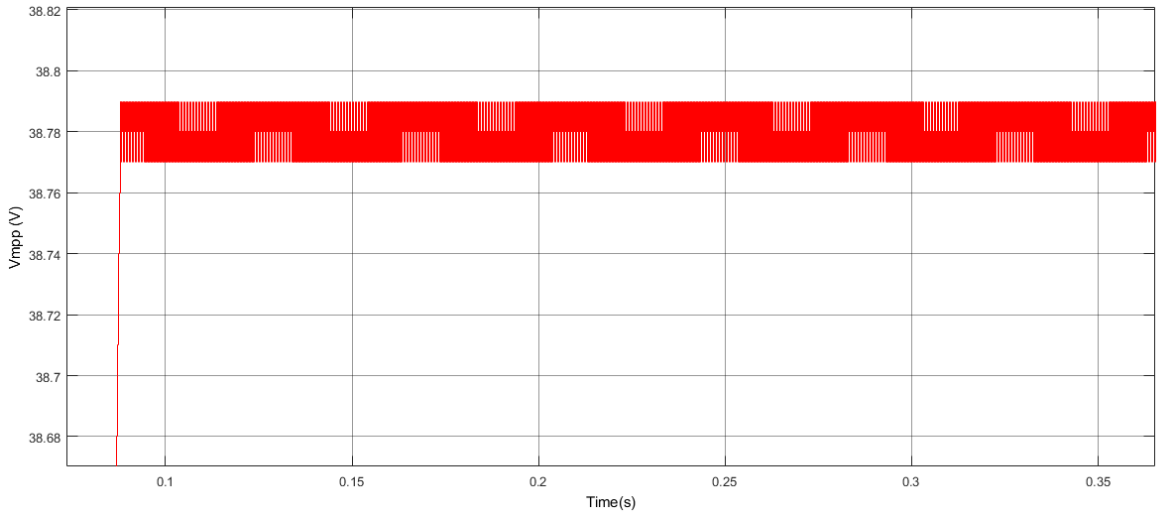

Figure 4.3: Performance of the MPPT tracker

Figure 4.4 below shows how the power output of the PV module follows the maximum power point under STC conditions (G=1000 W/m² and T_c=25°C). The transition from transient to permanent state is done very quickly due to the speed of the MPPT tracker.

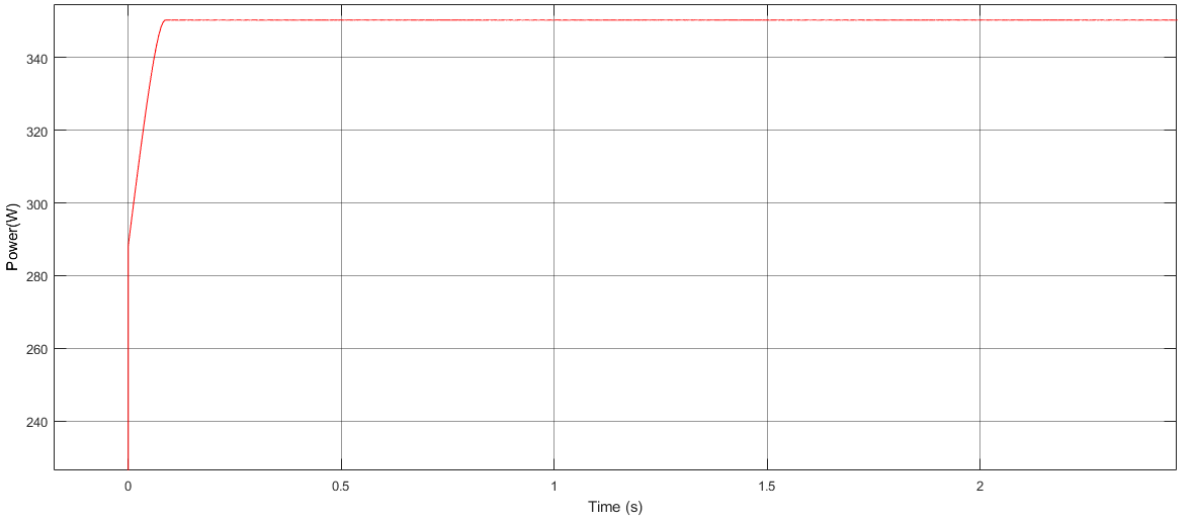

Figure 4.4: PV panel power output at STC

4.2.4. DC-DC converter control

The boost converter receives the current and voltage output of the PV generator and outputs a constant stepped-up voltage of V_{dc}=1200V that matches the one of the DC bus in the wind system. The control maintains V_{dc} constant all the time as observed in the figure below, and the latter will be received by the inverter to be converted into AC form.

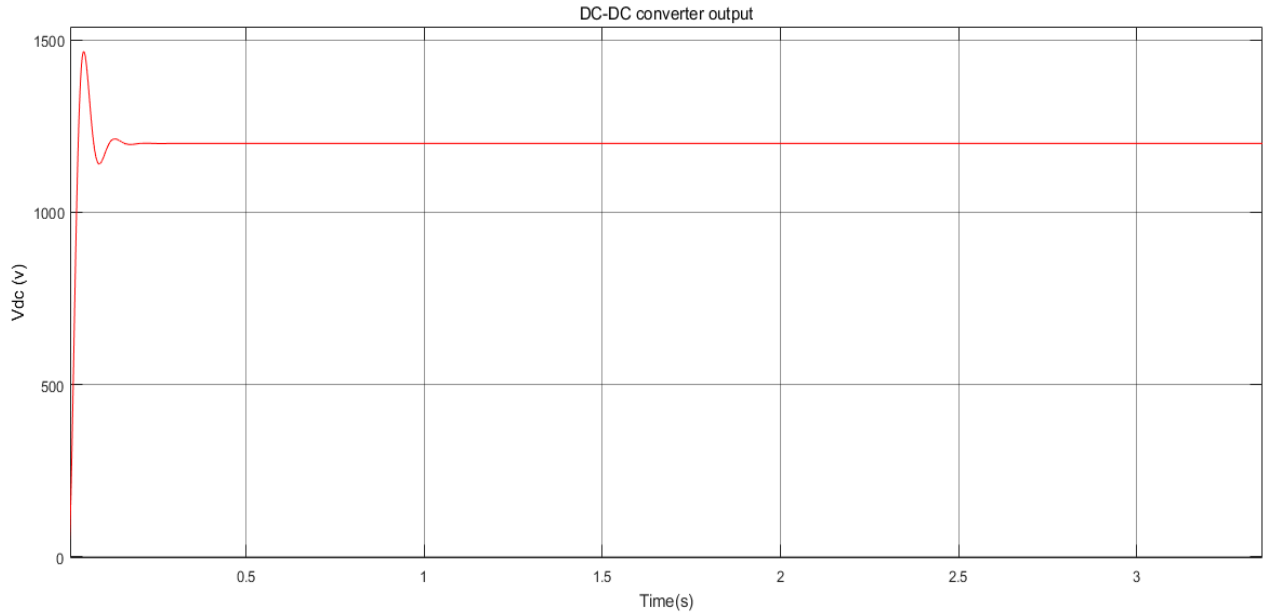

Figure 4.5: DC-DC converter output

4.2.5. Active and reactive power control

The performance of power control of the PV system is shown in Figure 4.6, both active and reactive power follow exactly the reference values. Negative values imply that the energy is injected to the grid while positive values mean that the energy is drawn from the latter. The reactive power is kept around zero to ensure unity power factor.

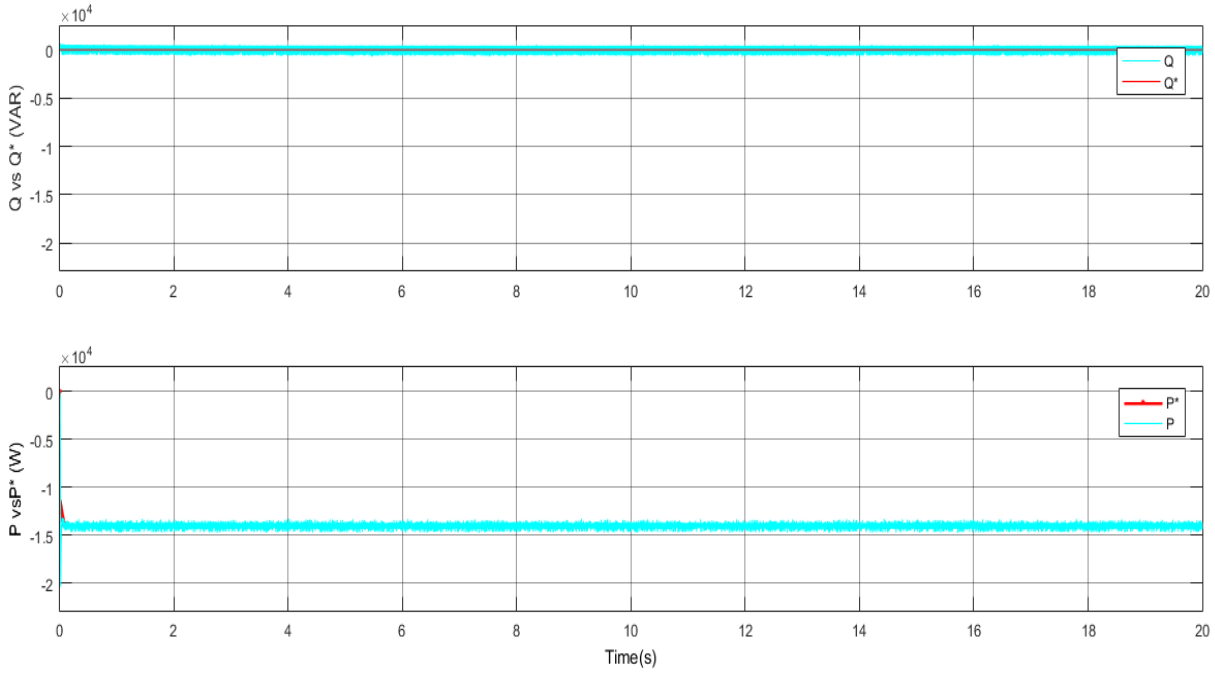

Figure 4.6: PV power control performance

The amount of power generated corresponds to one string under STC conditions, which is equivalent to 14 KW.

4.2.6. Output of the PV plant

The results of the simulation for the month of January show that the PV generator was able to produce from 4.35 MW to 4.73 MW depending on the day, irradiation level and temperature. The power is produced from 7 am to 6 pm with peak production occurring between midday and 2 pm. In addition, the power produced is steady throughout the month and does not fluctuate much.

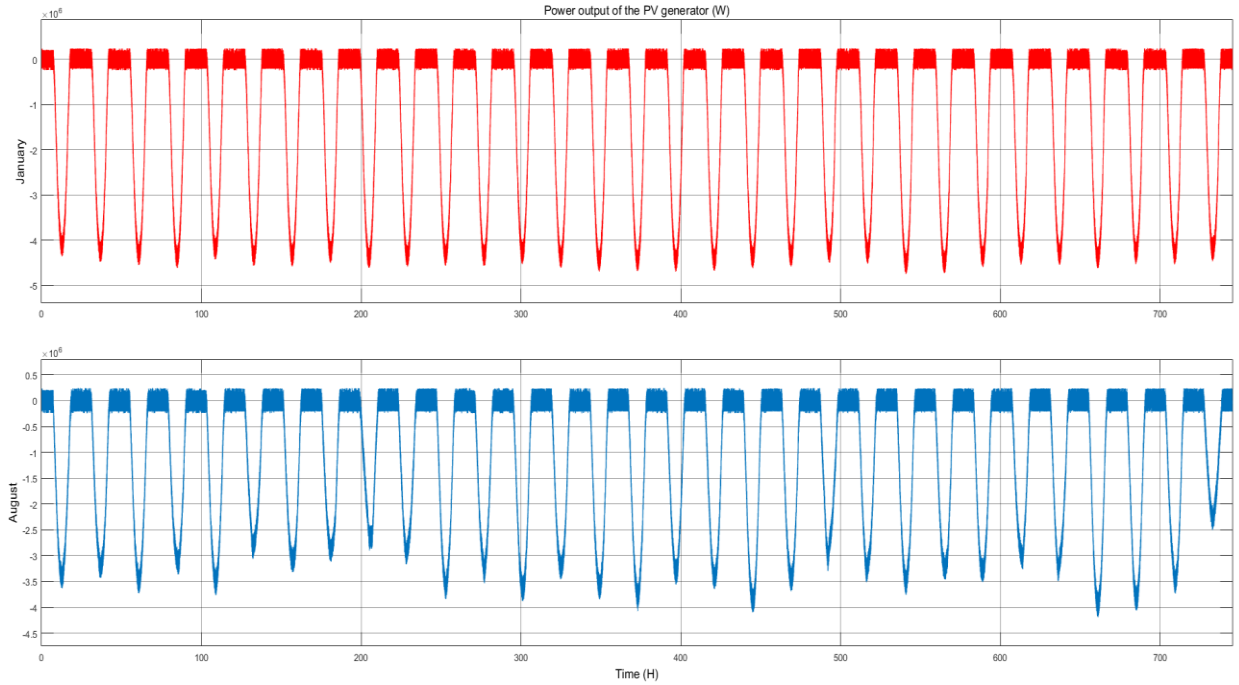

Figure 4.7: Power output of the PV plant (January vs August)

During the month of August, the PV generator produces less power compared to January. This decrease in power output is justified by the high temperatures and lower irradiation levels received by the PV generator. Peak production ranges from 2.45 MW to 4.15 MW. However, the production during the day lasts from 7 am to 7 pm delivering power for an extra hour compared to January, this is because summer days are longer than winter days.

Unlike the previous case, the power production sees some fluctuations where the biggest share is produced during the second third of the month, which is attributed with higher irradiation levels. Moreover, peak production in August occurs between 11 am and 2 pm.

4.3. The Wind System

The wind system composed of the ten large scale wind turbines have a rated power of 30 MW, the power output depends mainly on the speed of wind. The pitch angle of the turbine is fixed at it optimal value since pitch control is not implemented in the Simulink model. The turbines have a hub height of 80 meters, and wind speeds at this height have been calculated and are presented in the following subsection.

4.3.1. Wind speed at hub height

Simulating the wind block in Simulink for January and August resulted in the wind profile shown in Figure 4.8 below. January is characterized by moderate to high wind speeds, occurring between 11 am and 9 pm, the highest speeds are noticed in the second third of the month ranging from 12 to 18 m/s. the average speed is around 6 m/s.

In August, the wind profile shows more potential as high speeds are more frequent and the average speed is around 8 m/s. This means that the system should generate more energy in August than in January, and thus, the performance of the grid should be improved in this period of high demand.

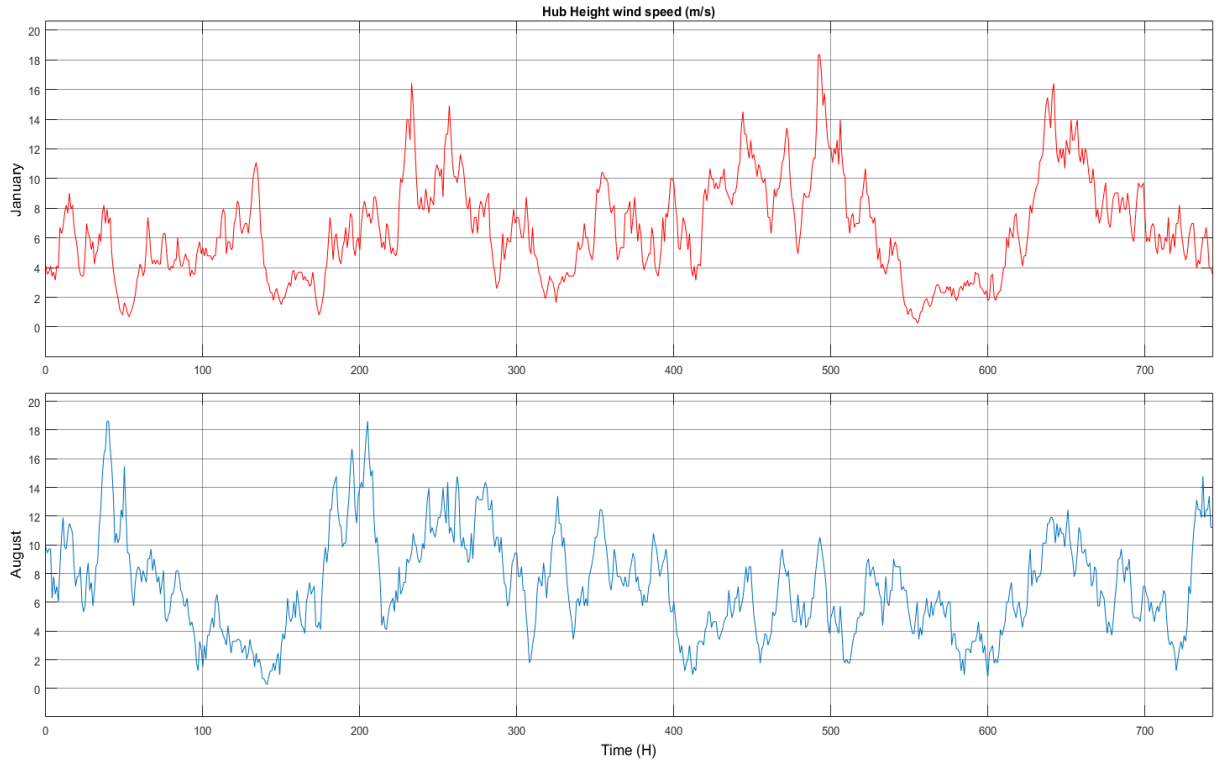

Figure 4.8: Wind speeds at hub height (January vs August)

4.3.2. MPPT control performance

The MPPT implemented to control the rotation speed of the turbine was tested with a multitude of different reference values and the result is presented in Figure 4.9. As observed, the rotational speed follows exactly the reference values, and the robustness of the control is tested by changing the reference values every time. This means in other words that the MPPT ensures maximum power extraction from the wind.

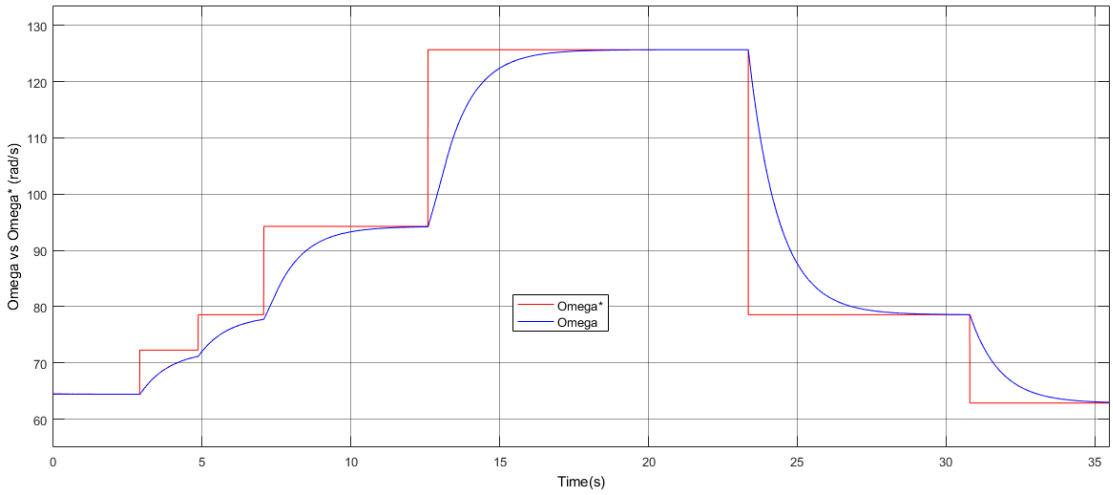

Figure 4.9: MPPT control performance

Figure 4.10 shows how the power coefficient changes with the MPPT. Obviously when changing the reference rotational speed, the power coefficient deviates from it maximum value of C_{pmax}= 0.35 but the MPPT control puts it back on track. Thus, the overall MPPT control handles well wind speed variations.

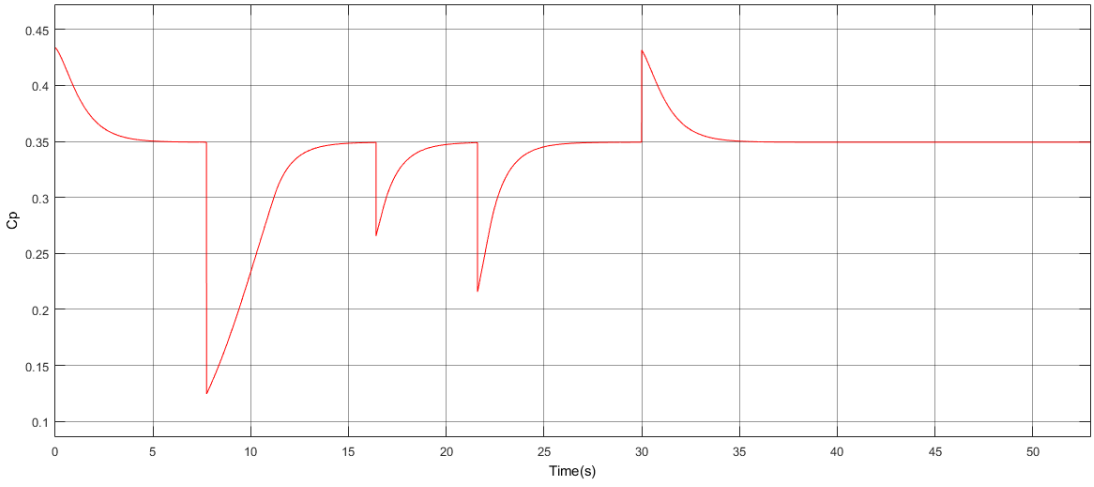

Figure 4.10: Influence of the MPPT on the maximum power coefficient

4.3.3. Active and reactive power from the wind system

Figure 4.11 below shows the performance of the power control implemented in the wind system. In the first graph, the reactive power is maintained zero while in the second graph, the active power follows exactly the given reference values. The reference values in the system are obtained from the mechanical model, these are based on the wind speed as discussed earlier in the previous chapter.

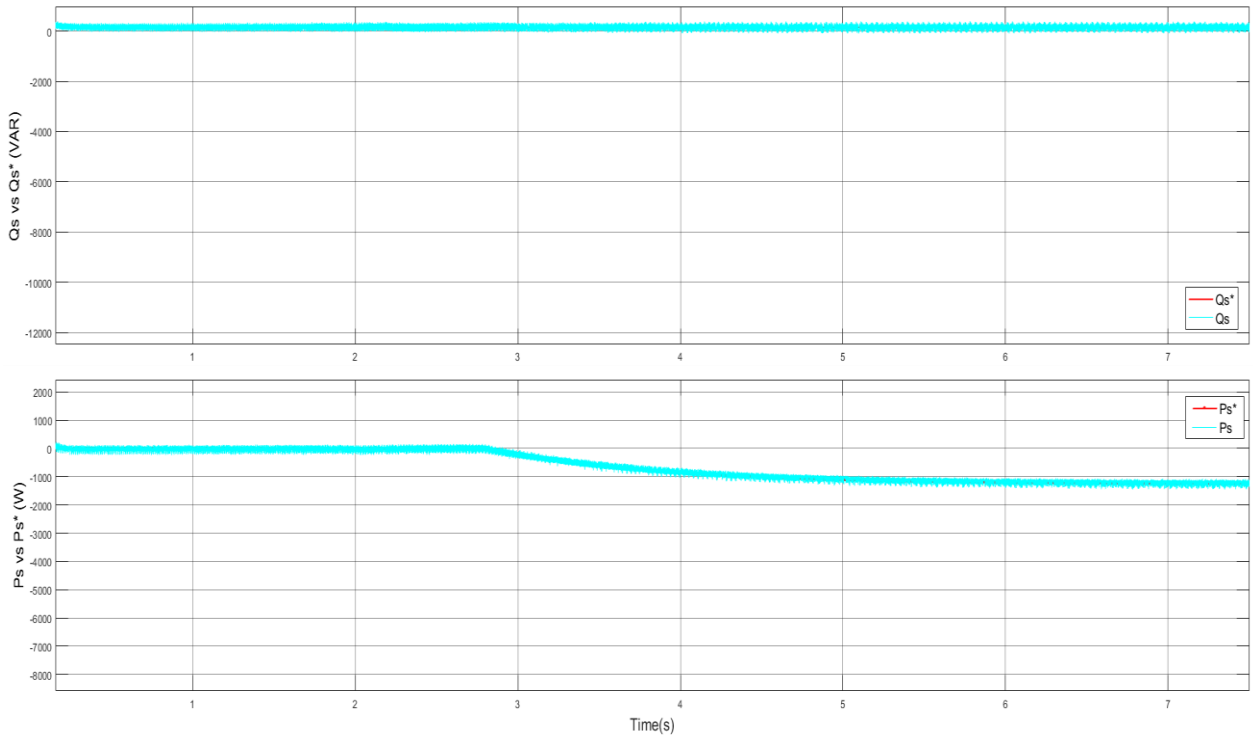

Figure 4.11: Wind power control performance

4.3.4. Output of the wind farm

The power produced by the wind system depends mainly on the wind profile, this changes widely between January and August as seen in the Figure 4.12 below. The month of January is characterized by lower wind speeds; hence the power output is lower compared to August. Peak production is reached in three weeks out of four, and the first week proved to have the lowest production. In most other days the output ranged from 10 to 23 MW.

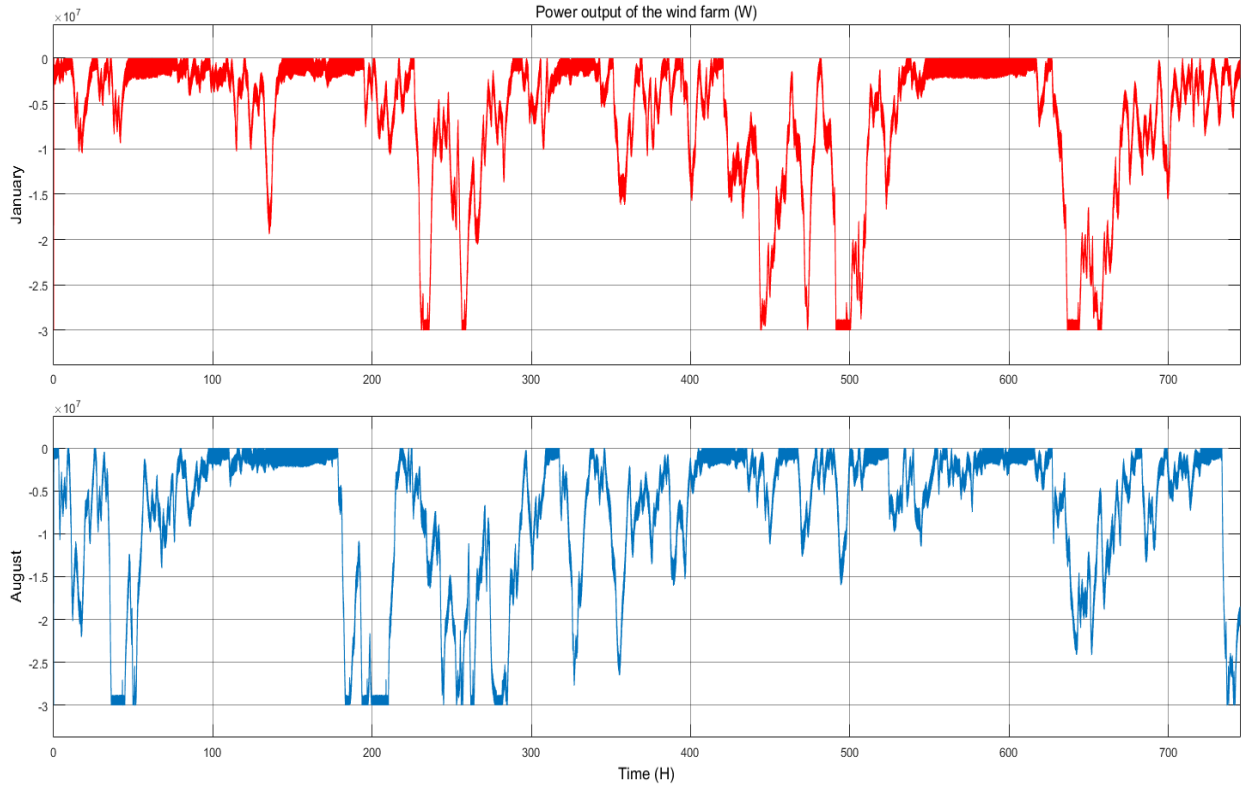

Figure 4.12: Power output of the wind farm (January vs August)

During August, more power was produced and the rated output was often reached especially in the first and last days of the month. An average of around 10 to 12 MW is maintained throughout the month. This amount of power will contribute significantly to grid performance as the load increases in this month.

4.4. The Hybrid System

The hybrid system combines the wind farm with the PV plant, so the total power output of the system is in fact the sum of the active power coming from the PV plant with the one generated by the wind farm. The reactive power is negligible because the reference value for the latter in the implemented power control was set to zero for a unitary power factor. The amount of power produced is compared to the power produced by the central power plant of Adrar to determine the capability of the system to aid the grid and improve its performance.

4.4.1. Hybrid system vs central plant power output

From the simulation results, it appears that the contribution of the system in January outperforms the one in August, although the production rate in August was higher. The power production in January varies from 10 to 34.5 MW which is close to the rated output power of the system. There were days where the hybrid system produced more electricity than the central power plant of Adrar, this means that the designed system was able to meet the entire demand of the city and more in those days. On the other hand, the central power plant produced an average of roughly 35 to 37 MW, and the peak loads seemed to appear from 6 pm to 9 pm late in the evening which is usually the time when most household activities are done and most house equipment are used. The lowest production occurs between 11 am and 2 pm, since at this time no lighting and no heating is required and most individuals are either in school or at work.

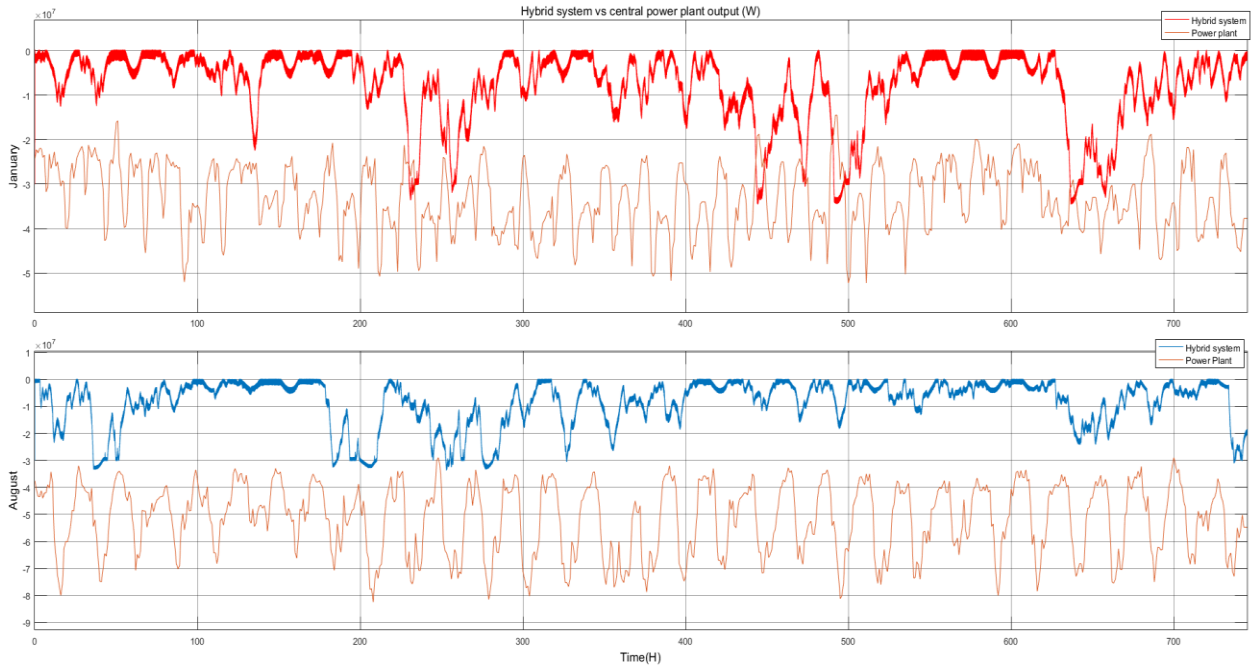

Figure 4.13: System power output vs central plant power production (January vs August)

In August, the hybrid system produced from 12 to 33 MW, however due to the higher wind potential, the amount of generated power was higher than in January. Despite that, the contribution was less since the amount of electricity delivered by the central power plant varies from a minimum of 30 MW to a peak of 82 MW with an average production lying near 50 MW. Peak loads occur between 2 pm and 6 pm while the lowest demand is recorded from 2 am to 10 am. This high demand is due to the cooling load, especially in July and August where temperatures often surpass 45 °C in the region. Despite the system's high power production, it is still low vis a vis the central power plant. But in most days the hybrid system managed to cover up to half of what the plant produces. In other words, the grid performance should be improved by up to 50%.

4.4.2. Power share covered by the hybrid system

Figure 4.14 below shows how much power is covered by the hybrid system for the months of January and August. It can be observed that during January, the hybrid system covered from 50% to 220% of what the central power plant produced. In other days the system managed to provide only 25% due to the low potential.

In August, the share covered by the system varies from 20% to 85% of the total power delivered by the central power plant of Adrar. It is worth mentioning that the power plant is used to supply the whole province of Adrar and that the true load of Adrar's city is in fact much lower. Thus, it can be said that the system performs very well and provides enough power to cover an important portion of the demand.

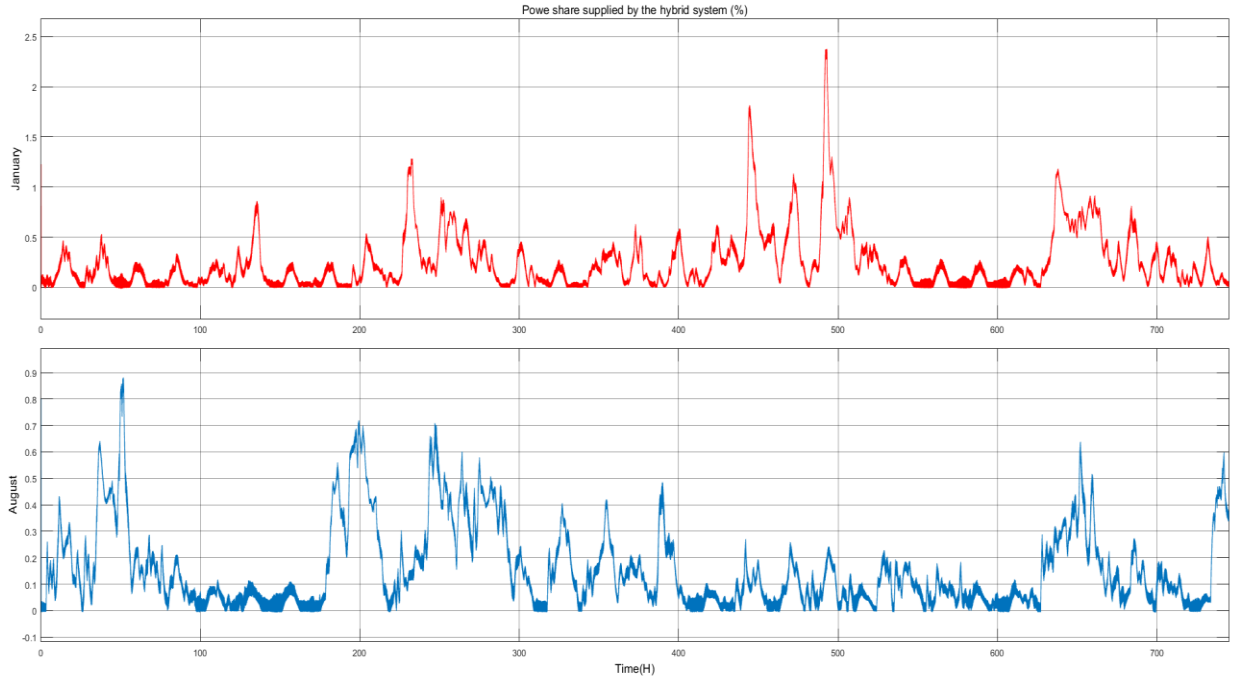

Figure 4.14: Share covered by the hybrid system (January vs August)

4.4.3. Typical daily output of the system

To see how the system performs throughout the day, the Simulink model was simulated for the 27th of each month. The day was picked due to average potential available of both solar and wind sources. Below, Figures 4.15 and 4.16 show the power output from the PV plant and the wind farm. For the PV system, it is clear that in the 27th of January, the PV plant produces power from 7:30 am to 6 pm with a peak production of 4.2 MW around 1.30 pm. In the second chart, power is produced from 7:30 am to 7 pm with the maximum production occurring also around 1 pm.

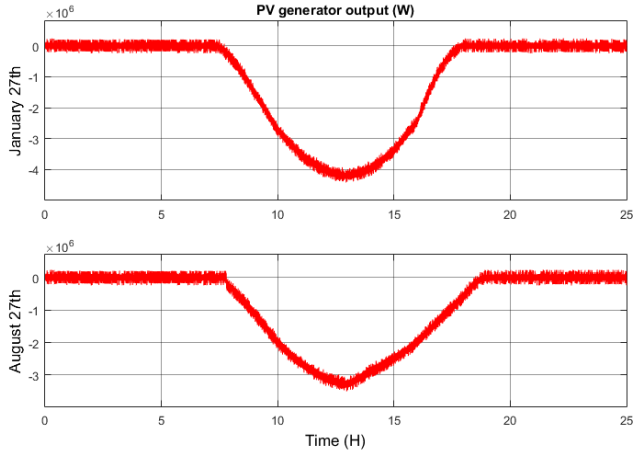

Figure 4.15: PV plant typical daily power output

In this case, the wind farm produced more power on the 27th January then on the 27th of August. The rated power was attained from midday to 8 pm in January while the maximum output in august reached 23 MW around 7 pm. This was a special case as in most days the power output is higher in August.

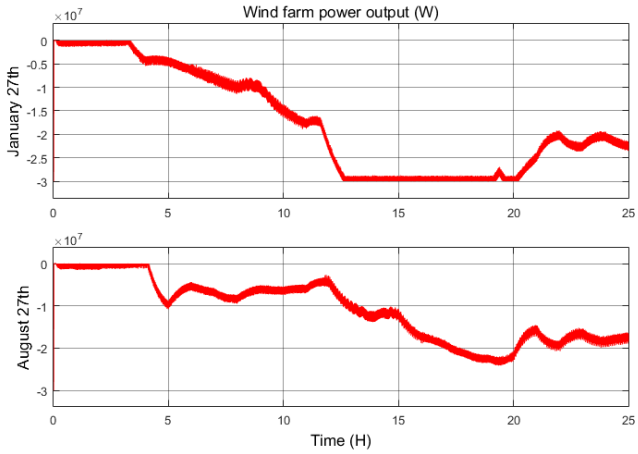

Figure 4.16: Wind farm typical daily power output

The contribution of the PV plant to the total power output is shown in Figure 4.17, it contributed more in August with 40% during peak production versus 18% in January. While the wind farm contribution (shown in Figure 4.18) was significantly higher and ranged between 80% to 100% in January versus 60% to 100% in August. The contribution of the PV plant is quite important especially when considering its low rated power output compared to the wind farm

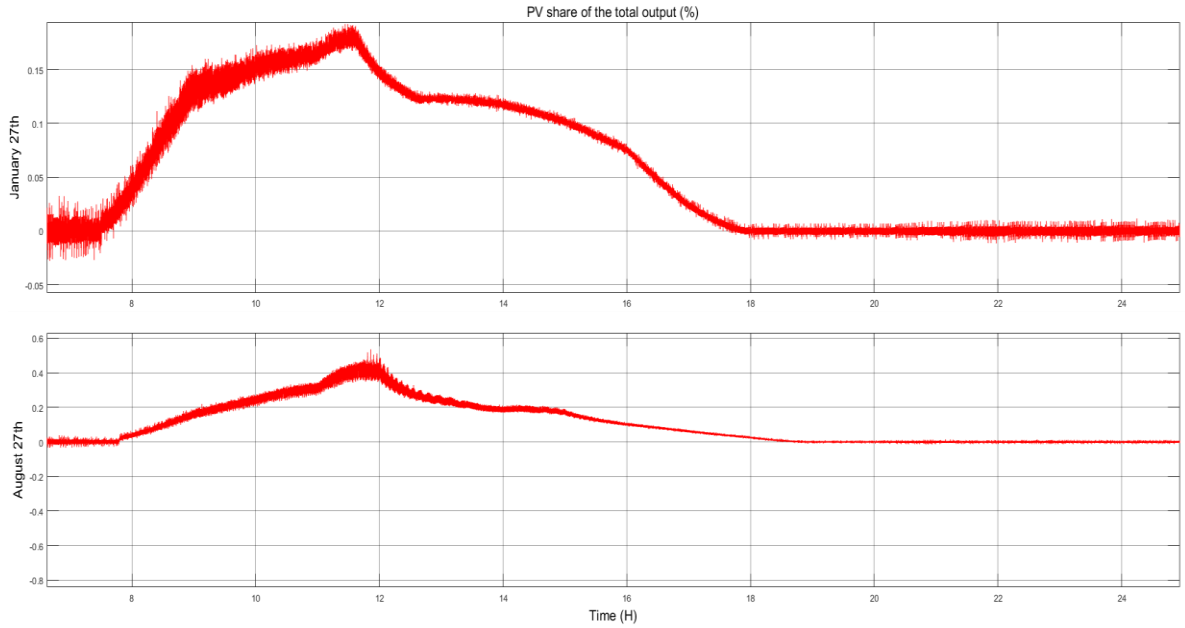

Figure 4.17: Contribution of the PV plant

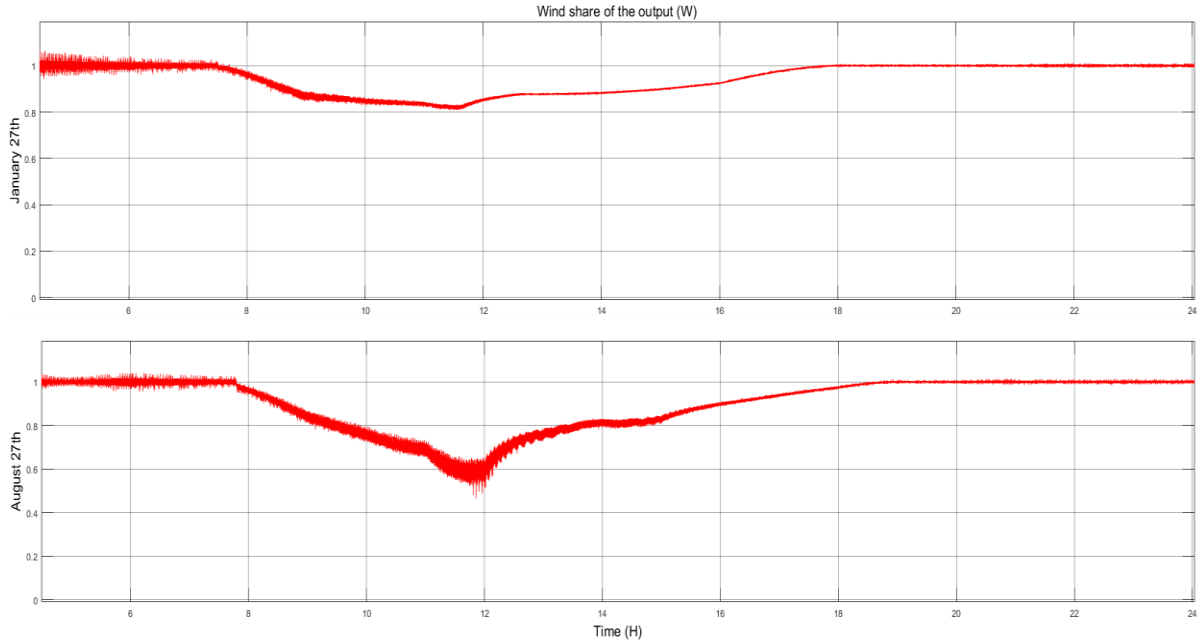

Figure 4.18: Contribution of the wind farm

4.5. Cost Analysis

HOMER results show from an economical point of view that the system composed of a 5 MW rated PV system and a 30 MW rated wind system has a total net present value (NPV) of $167 million, whereas the levelized cost of electricity (LCOE) sits at 0.084 $/kWh. The LCOE is very profitable compared to the selling price of 0.114 $/kWh guaranteed by the feed in tariff for the duration of the project. As a result, the payback period is in just 7.3 years and by the end of the projects lifetime a cumulative net profit of $127 million is reached. Figure 4.18 depicts the cash flow over the lifespan of the project, which shows how much money is either spent on or gained by the project.

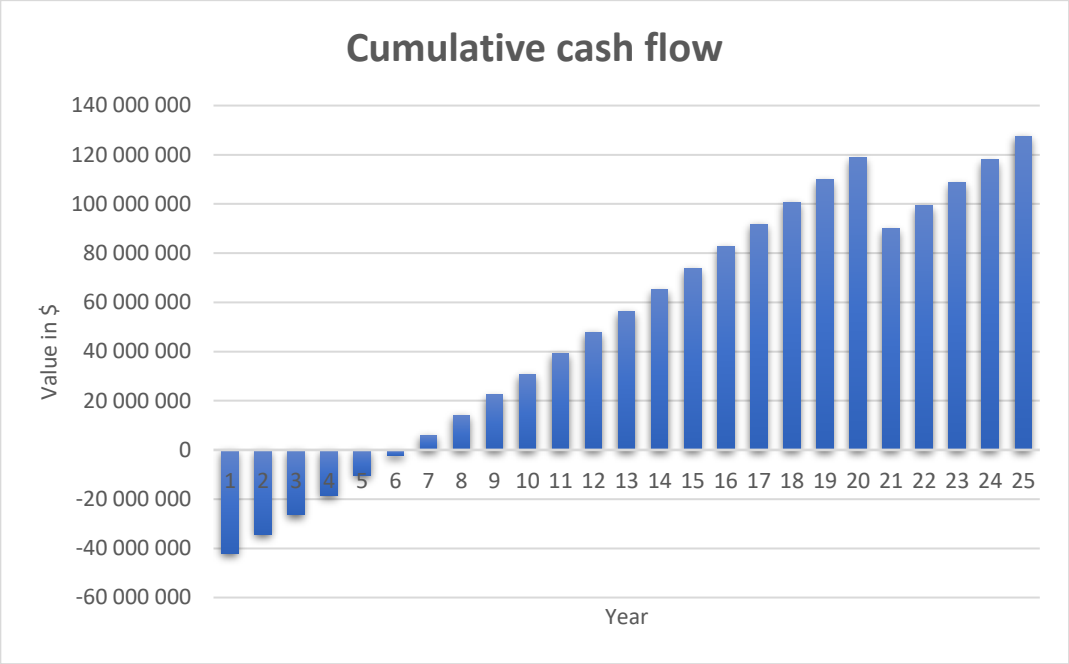

Figure 4.19: Cumulative cash flow of the project

The initial investment for implementing the project is evaluated at $42.1 million, and the total operating and maintenance cost of the whole system for 25 years is $7.46 million. Figure 4.19 shows the cost share of different system components. It is observed that the PV system and the set of converters each cost initially 4% of the initially investment while the rest of the cost is attributed to the wind turbines.

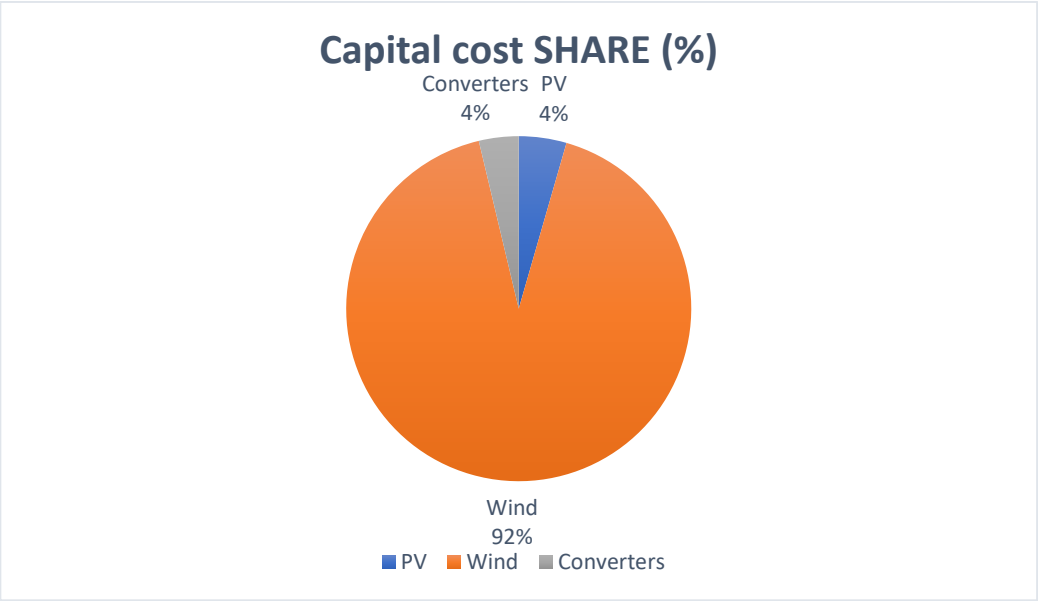

Figure 4.20: Components share of the total cost

Much like the capital cost, wind dominates the share of operating and maintenance costs as seen in Figure 4.20 below, the PV array and converters need $15036 and $12530 respectively for every year of the project lifetime, while the wind turbines require $309000 representing 91.8% of the total cost.

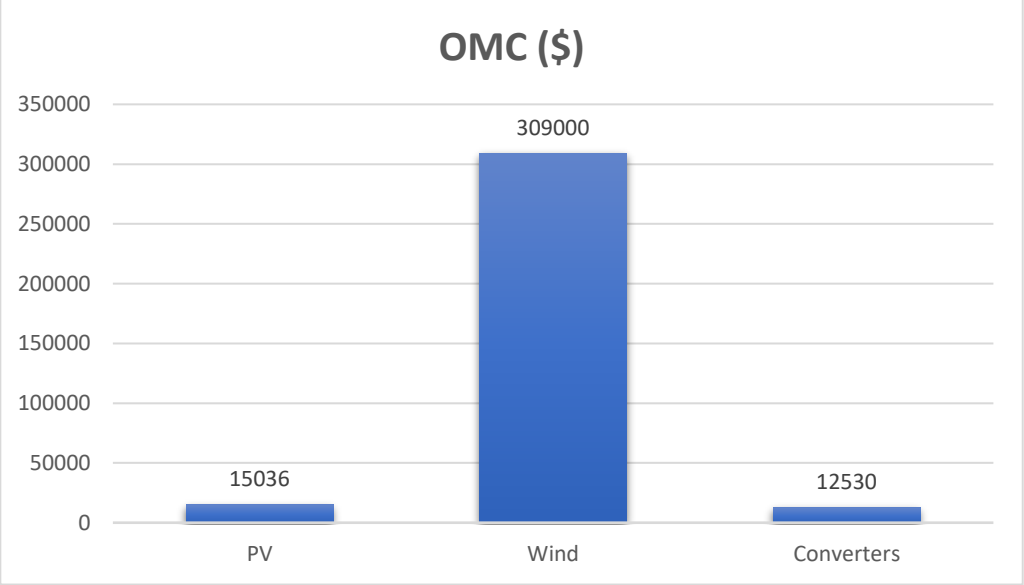

Figure 4.21: Operating and maintenance costs

Furthermore, the PV system contributes to the total power generation by 14.5% versus 85.5% coming from the wind system. The total monthly power production of each system is given in Figure 4.21. This wide

difference in contribution is dependent on two factors; the different size of each system and the difference in site solar and wind potential over the year.

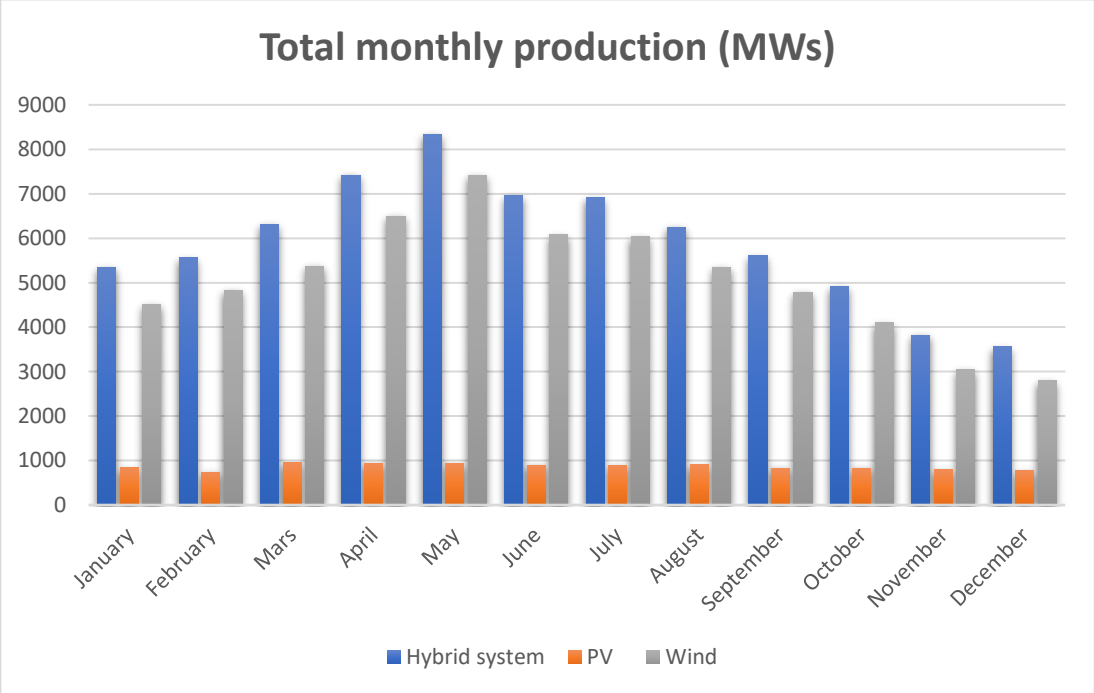

Figure 4.22: Total production per month

4.6. Environmental Impact

From the environmental aspect, the designed system has a significant positive impact on the environment over the conventional power plant. It was found that implementing the hybrid system yields a remarkable reduction in harmful greenhouse gas emissions including CO_2, SO_2 and NO_x. Such emission reductions contribute to mitigating global warming and climate change. The summary of the amounts of avoided emissions have been tabulated below.

Table 4.1: Reduced greenhouse gas emissions

Gas	Emissions avoided (kg/year)
Carbon Dioxide (CO_2)	28 393 342
Sulfur Dioxide (SO_2)	194 494
Nitrogen Oxides (NO_x)	95 118

CHAPTER FIVE: CONCLUSION AND RECOMMENDATIONS

Outline

5.1. Conclusion

In just a few hours, the great desert receives enough solar energy to power what mankind consume in a whole year. Wind potential in Sub-Saharan Africa for instance, can produce several times the current electricity consumption of the whole continent. In line with the will of Algeria to integrate 5 GW of wind energy and 13.6 GW of solar photovoltaic energy in the energy mix by 2030, this study was conducted with the aim of designing, modelling and simulating a PV-wind large scale power plant. The suitable location for the power plant was chosen according to the available wind and solar energy potential and the capability to host large scale PV plants and wind farms. For that, a complete review of the renewable energy potential in Algeria was performed.

The designed power plant houses a PV plant with a rated capacity of 5 MW, and a wind farm consisting of 10 wind turbines and delivering a maximum of 30 MW. Considering the challenges faced by the national grid in the country, the system was decided to be grid-connected and to inject all the produced power into the grid. The system was modelled in Simulink, and proper control of the different system elements was implemented after reviewing the literature. The performance of the designed system was assessed and the system was simulated with hourly weather data for January and August representing the critical periods of the winter and summer seasons. The power output was compared to the central power plant of the region in question to evaluate the contribution to grid performance. To evaluate the feasibility of the such project and determine its cost-benefit contribution, an economic and environmental analysis was performed in HOMER.

In order for the simulation results to be as real as possible, the temperature of PV cells, the wind speed at hub height and the irradiation received by the modules were calculated from the available data. The performance of the PV system was found to be higher in January due to high irradiation levels and low temperatures, while it was reduced by the high temperatures in August. The wind system produced more energy in August due to the higher wind speeds.

The production of the system was able to cover from 50% to more than 200% of the central power plant output in January with production rates varying from 12 to 34.5 MW. In August, the production ranged between 12 and 33 MW accounting for 20% to 85% of the central power plant output. Overall, the PV system produced around 14.5% of the total power output versus 85.5% from the wind system. The contribution to grid performance is higher in January while in August the cooling loads seemed to be a heavy burden lowering the contribution of the system, though the production rates should be enough to tackle power outage problems during this hot period.

The economic analysis in HOMER showed that the power plant project is very feasible with a total initial investment of $42.1 million and a net present value of $167 million over a lifetime of 25 years. The levelized cost of electricity was determined as 0.084 $/kWh while the selling price was evaluated at 0.114 $/kWh, this allowed for a short payback period of 7.3 years and an accumulative net profit of $127 million at the end of the project's lifetime. Moreover, the wind system represents 92% of the initial investment and 91.8% of the total operating and maintenance costs. The environmental analysis revealed that implementing this project yields a significant yearly reduction in greenhouse gas emissions, comprised of 28 393 342 kg of CO_2, 194 494 kg of SO_2, and 95 118 kg of NO_x.

In conclusion, the designed system proved to be technically and economically feasible. Thus, in terms of power, the system will cover a significant share form the total load of the region in question while directly improving the performance of the national grid. From an economical point of view, the project is cost effective, pays back the initial investment quickly and generates long term profits. The environmental aspect is also addressed and the contribution to the adopted renewable energy program is ensured.

5.2. Recommendations

The designed system in this thesis proved its performance and feasibility for the case study of Adrar. However, the system works only in grid-connected mode which means in case of grid blackouts the system will stop for security reasons. Thus, the transition from grid-connected to stand-alone mode of operation should be studied to ensure power supply even in periods of power shortage from the grid.

Large scale power plants are usually not equipped with storage systems, because of the required high storage capacity, thus, future works should address the storage issue and determine its viability.

Finally, deserts are known of their hot weather and frequent sand storms, and sand accumulation over PV panels affects their performance. Hence, future research must address this issue and find solutions to the cleaning process of the PV panels. Moreover, this study could be used to compare PV performance in other regions with lower temperature levels.

BIBLIOGRAPHY

[1] H. Daaou Nedjari, S. K. Haddouche, A. Balehouane, and O. Guerri, "Optimal windy sites in Algeria: Potential and perspectives," *Energy*, vol. 147, pp. 1240–1255, 2018.

[2] G. Mustapha, H. Mohamed, and B. Achraf, "OPEC : Algeria," *Annual Statistical Bulletin 2018*, 2018. [Online]. Available: https://www.opec.org/opec_web/en/about_us/146.htm. [Accessed: 30-Jul-2018].

[3] A. Harrouz, M. Abbes, I. Colak, and K. Kayisli, "Smart grid and renewable energy systems in Algeria," *Sixth Int. Conf. Renew. Energy Res. Appl.*, vol. 1, pp. 1166–1171, 2017.

[4] J. Corry, R. Ferroukhi, C. Garcia Banos, M. Jordan, A. Khalid, A. Reeves, M. Renner and M. Taylor, "Renewables 2016 global status report," *REN21 2016*, 2016.

[5] R. Maoued, A. Mammeri M. D. Draou. and B. Benyoucef, "Techno-economic analysis of a standalone hybrid photovoltaic-wind system. Application in electrification of a house in Adrar region," *Energy Procedia*, vol. 74, pp. 1192–1204, 2015.

[6] Z. Abada and M. Bouharkat, "Study of management strategy of energy resources in Algeria," *Energy Reports*, vol. 4, pp. 1–7, 2018.

[7] L. Schnatbaum, "Solar thermal power plants," *Eur. Phys. J.*, p. 129, 2009.

[8] S. Bouchakour, "Contribution a l'Etude et Commande d'un Couplage des Systèmes Hybrides (Réseaux et Photovoltaïc) pour la Production d'Énergie Électrique," Université Djillali Liabes de Sidi Bel Abbes, 2015.

[9] A. Boudghene Stambouli, Z. Khiat, S. Flazi, and Y. Kitamura., "A review on the renewable energy Development in Algeria: Current perspective, energy scenario and sustainability issues," *Renew. Sustain. Energy Rev.*, vol. 16, 2012.

[10] S. M. Boudia, A. Benmansour, and M. A. Tabet Hellal, "Wind resource assessment in Algeria," *Sustain. Cities Soc.*, vol. 22, pp. 171–183, 2016.

[11] M. Osmani, "Renewable Energies and Shale Gas in Algeria, between fact and perspectives - PDF."

[12] Y.Himri, A. Boudghene Stambouli, B. Draoui, and S.Himri, "Wind power resource in the southwestern region of Algeria," *Renew. Sustain. Energy Rev.*, vol. 14, pp. 554–556, 2010.

[13] "ADRAR: wind potential (JEEE'15)," *Development Unit of Solar Equipments*, 2015. [Online]. Available: http://udes.cder.dz/site anglais/adrar.php. [Accessed: 05-Apr-2018].

[14] K. Abdeladim, S. Bouchakour, A. Hadj Arab and S. Ould Amrouch., "Renewable Energies in Algeria : Current Situation and Perspectives," *29th Eur. Photovolt. Sol. Energy Conf. Exhib. Renew.*, no. September, p. 2014, 2014.

[15] A. Boudghene Stambouli, “Promotion of renewable energies in Algeria: Strategies and perspectives,” *Renew. Sustain. Energy Rev.*, vol. 15, no. 2, pp. 1169–1181, 2011.

[16] M. Djamai and N. Kasbadji Merzouk, “Wind farm feasibility study and site selection in Adrar, Algeria,” *Energy Procedia*, vol. 6, pp. 136–142, 2011.

[17] “Maps of Adrar Province,” *Wikimedia*, 2013. [Online]. Available: https://commons.wikimedia.org/wiki/Category:Maps_of_Adrar_Province. [Accessed: 19May-2018].

[18] B. Bouzidi, “Viability of solar or wind for water pumping systems in the Algerian Sahara regions - Case study Adrar,” *Renew. Sustain. Energy Rev.*, vol. 15, no. 9, pp. 4436–4442, 2011.

[19] M. Yaneva, “Algeria’s Adrar commissions 48 MW of solar power,” *Renewables Now*, 2016. [Online]. Available: https://renewablesnow.com/news/algerias-adrar-commissions-48-mwof-solar-power-516499/. [Accessed: 12-Apr-2018].

[20] E. H. S, “Energie Solaire à Adrar,” *Le Soir d’Algérie*, 2010. [Online]. Available : https://www.djazairess.com/fr/lesoirdalgerie/106930. [Accessed: 14-Apr-2018].

[21] Ministère de Transport, “Recueil de Données,” *Atlas Climatologique National*. Office national de la météorologie, 2008.

[22] R. Dabou, F. Bouchafaa, A. Hadj Arab, A. Bouraiou, M. D. Draou, A. Neçaiba and M. Mostefaoui, “Monitoring and performance analysis of grid connected photovoltaic under different climatic conditions in south Algeria,” *Energy Convers. Manag.*, vol. 130, pp. 200–206, 2016.

[23] S. Sumathi, L. Ashok Kumar, and P. Surekha, *Solar PV and Wind Energy Conversion Systems*. 2015.

[24] J. Twidell and T. Weir, *Renewable Energy Resources*, Third Edit. New York: Routledge, 2006.

[25] A. Abete, E. Barbisio, F. Cane and P. Demartini, “Analysis of photovoltaic modules with protection diodes in presence of mismatching,” *21st IEEE Photovolt. Spec. Conf.*, 1990.

[26] NREL, “Best Research-Cell Efficiencies,” 2018. [Online]. Available: https://www.nrel.gov/pv/assets/images/efficiency-chart.png. [Accessed: 28-Apr-2018].

[27] “Difference between monocrystalline polycrystalline and Amorphous thin film solar cell,” *Sun Tronic Solar*, 2017. [Online]. Available: http://www.suntronicsolar.com/differencebetween-monocrystalline-polycrystalline-and-amorphous-thin-film-solar-cell/. [Accessed: 20-Apr-2018].

[28] P. Stéphane, “Nouvelles architectures distribuées de gestion et de conversion de l’énergie pour les applications photovoltaïques,” Université de Toulouse, 2009.

[29] F. Fabregat-Santiago, G. Garcia-Belmonte, I. Mora-Seró, and J. Bisquert, "Characterization of nanostructured hybrid and organic solar cells by impedance spectroscopy," *Phys. Chem. Chem. Phys.*, vol. 13, no. 20, p. 9083, 2011.

[30] A. M. Bagher, M. M. Abadi Vahid, M. Mirhabibi. Types of Solar Cells and Application. American Journal of Optics and Photonics. Vol. 3, No. 5, 2015, pp. 94-113

[31] R. R. L. King, K. D. Edmondson, K. M. Fetzer, C. M. Kinsey, J. S. Yoon, H. Sherif and R. A. Karam., "40% efficient metamorphic GaInP/GaInAs/Ge multijunction solar cells," *Appl. Phys. Lett.*, vol. 90, no. 18, 2007.

[32] J. S. Manser, J. A. Christians, and P. V. Kamat, "Intriguing Optoelectronic Properties of Metal Halide Perovskites," *Chem. Rev.*, vol. 116, no. 21, pp. 12956–13008, Nov. 2016.

[33] S. Varun, S. D. Stranks, and H. J. Snaith, "Outshining Silicon," *Sci. Am.*, pp. 44–46, 2015.

[34] E. M. Natsheh, A. Albarbar, and J. Yazdani, "Modeling and control for smart grid integration of solar/wind energy conversion system," *2011 2nd IEEE PES Int. Conf. Exhib. Innov. Smart Grid Technol.*, pp. 1–8, 2011.

[35] Alternative Energy Tutorials, "Solar Cell I-V Characteristic," 2016. [Online]. Available: http://www.alternative-energy-tutorials.com/energy-articles/solar-cell-i-v-characteristic.html. [Accessed: 29-Apr-2018].

[36] V. Punyani, "How to Wire Solar Panels in Parallel or Series," *HES PV Blog*, 2014. [Online]. Available: http://hespv.ca/blog/wire-solar-panels-parallel-vs-series/. [Accessed: 29Apr-2018].

[37] A. A. Katkar, N. N. Shinde, and P. S. Patil, "Performance & Evaluation of Industrial Solar Cell w.r.t. Temperature and Humidity," *Int. J. Res. Mech. Eng. Technol.*, vol. 1, no. 1, pp. 69–73, 2011.

[38] A. U. Harad, G. D. Padaval, G. J. Malik, and V. D. Farde, "Factor affecting on polycrystaline photovoltaic (PV) performance," *ational J. Res. Sci. Eng.*, vol. 3, no. 2, pp. 560–566, 2017.

[39] S. Obara, M. Kawai, O. Kawae, and Y. Morizane, "Operational planning of an independent microgrid containing tidal power generators," *SOFCs photovoltaics, Appl. Energy*, vol. 102, pp. 1443–1457, 2013.

[40] T. Jacob and S. Arun, "Maximum Power Point Tracking of hybrid PV and wind energy systems using a new converter topology," *2012 Int. Conf. Green Technol.*, pp. 280–287, 2012.

[41] R. I. Putri, S. Wibowo, and M. Rifa'i, "Maximum power point tracking for photovoltaic using incremental conductance method," *Energy Procedia*, vol. 68, pp. 22–30, 2015.

[42] J. Ahmad, "A fractional open circuit voltage based maximum power point tracker for photovoltaic arrays," *ICSTE 2010 - 2010 2nd Int. Conf. Softw. Technol. Eng. Proc.*, vol. 1, pp. 247–250, 2010.

[43] N. Díaz, A. Luna, and O. Duarte, “Improved MPPT short-circuit current method by a fuzzy short-circuit current estimator,” *IEEE Energy Convers. Congr. Expo. Energy Convers. Innov. a Clean Energy Futur. ECCE 2011, Proc.*, pp. 211–218, 2011.

[44] A. Goetzberger and V. U. Hoffmann, “Photovoltaic Solar Energy Generation,” *Opt. Sci.*, vol. 33, 2005.

[45] F. J. Pazos, “Power frequency overvoltages generated by solar plants,” *20th Int. Conf. Exhib. Electr. Distrib.*, vol. 2, 2009.

[46] H. Colin, C. Duvauchelle, G. Moine, Y. Tanguy, B. Gaiddon, and T. Tran-Quoc, “Raccordement des installations photovoltaïques au réseau public de distribution électrique à basse tension,” *cadre réglementaire, impacts et préconisations, ESPRIT*, 2010.

[47] E. Caamano, J. Thornycroft, H. De Moor, and S. Cobben, “State-of-the-Art on Dispersed PV Power Generation: Publications review on the impacts of PV Distributed Generation and Electricity networks (Technical Report),” 2007.

[48] F. Blaabjerg and K. Ma, “Wind Energy Systems,” *Proc. IEEE*, vol. 105, no. 11, pp. 2116–2131, 2017.

[49] K. Mohammadia, O. Alavib, N. Goudarzid, and M. Jalilvande, “Assessing different parameters estimation methods of Weibull distribution to compute wind power density,” *Energy Conver. Manag*, vol. 108, pp. 322–335, 2016.

[50] L. Y. Pao and K. E. Johnson, “Control of wind turbines,” *IEEE Control Syst. Mag.*, vol. 31, no. 2, pp. 44–62, 2011.

[51] H. Polinder, J. A. Ferreira, B. B. Jensen, A. B. Abrahamsen, K. Atallah, and R. A. McMahon, “Trends in wind turbine generator systems,” *IEEE J. Emerg. Sel. Top. Power Electron.*, vol. 1, no. 3, pp. 174–185, 2013.

[52] P. Tiwari, S. Dhananjay, and K. A. Kumar, “Study of Wind Energy System with Induction Generators,” National Institute of Technology Rourkela, 2013.

[53] H. Houda, “Modélisation, simulation et optimisation d'un système hbride éolienphotovoltaic,” Université Aboubekr Belkaid de Tlemcen, 2010.

[54] J. G. Slootweg and P. W. L. Kling, “Wind Power: Modelling and Impact on Power System Dynamics,” pp. 122-139, 2003.

[55] D. Le Gourières, *Energie éolienne, Théorie, conception et calcul pratique des installations*, Second Edi, pp. 182-196, 2008.

[56] Z. Dekali, L. Baghli, and A. Boumediene, “Experimental Implantation of an Emulator of a Wind Energy Conversion Chain System Based on Double Fed Induction Generator,” *11emes Journées Sci. Tech. JST’11*, vol. 17–19 Apri, 2018.

[57] R. Gasch and J. Twele, *Wind Power Plants: Fundamentals, Design, Construction and Operation*, Second edi, 2012.

[58] M. del Mar Martınez-Dıaz, “Stand-alone hybrid renewable energy systems (HRES),” Universitat Polit`ecnica de Catalunya, 2017.

[59] P. J. Eduardo Monney de Sa, “Integration of Renewable Sources into Hybrid Renewable Energy Systems,” University of Porto, 2011.

[60] R. Luna-Rubio, M. Trejo-Perea, D. Vargas-Vazquez, and G. J. Rıos-Moreno, “Optimal sizing of renewable hybrids energy systems: A review of methodologies.,” *Sol. Energy*, vol. 4, pp. 1077–1088, 2012.

[61] F. J. Vivas, A. De Heras, F. Segura, and J. M. Andújar, “A review of energy management strategies for renewable hybrid energy systems with hydrogen backup,” *Renew. Sustain. Energy Rev.*, vol. 82, no. September 2017, pp. 126–155, 2018.

[62] J. Jana, H. Saha, and K. D. Bhattacharya, “A review of inverter topologies for single-phase grid-connected photovoltaic systems,” *Renew. Sustain. Energy Rev.*, vol. 72, no. November 2016, pp. 1256–1270, 2017.

[63] B. Verhoeven, “Utility Aspects of Grid Connected Photovoltaic Power Systems,” *Int. Energy Agency Photovolt. Power Syst.*, 1998.

[64] A. Chauchan and R.P. Saini, “A review on integrated Renewable Energy Systems based power generation for stand-alone applications: configurations, storage options, sizing methodologies and control.,” *Renew Sustain Energy Rev*, vol. 120, pp. 38–99, 2014.

[65] J. Remund, “A detailed look at the model steps and uncertainties,” Bern, 2015.

[66] “Optimum Tilt of Solar Panels.” [Online]. Available: www.solarpaneltilt.com. [Accessed: 15-Jul-2018].

[67] J. Meyers and C. Meneveau, “Optimal turbine spacing in fully developed wind farm boundary layers,” *Wind Energ*, vol. 15, pp. 305–317, 2012.

[68] M. G. Villalva, J. R. Gazoli, and E. R. Filho, “Comprehensive Approach to Modeling and Simulation of Photovoltaic Arrays,” vol. 24, no. 5, pp. 1198–1208, 2009.

[69] M. A. Mosalam Shaltout, A. A. El-Hadad, M. A. Fadly, A. F. Hassan, and A. M. Mahrous, “Determination of suitable types of solar cells for optimal outdoor performance in desert climate,” *Renew. Energy*, vol. 19, no. 1–2, pp. 71–74, 2000.

[70] F. Aichouche, “Conception, modélisation et simulation d ’ un onduleur assisté (Grid-Tie Inverter), ” University of Aboubekr Belkaid, 2015.

[71] E. Isen and A. F. Bakan, “Development of 10 kW Three-Phase Grid Connected Inverter,” vol. 57, no. 2, pp. 319–328, 2016.

[72] M. Loucif, “Synthèse de lois de commande non-linéaires pour le contrôle d’une machine asynchrone à double alimentation dédiée à un système aérogénérateur,” Université Aboubakr Belkaïd de Tlemcen, pp. 42–44, 2016.

[73] A. Gaillard, “Système éolien basé sur une MADA : contribution à l’étude de la qualité de l’énergie électrique et de la continuité de service,” Université Henri Poincaré, Nancy-I, 2010.

[74] T. Ghennam, “Supervision d’une ferme éolienne pour son intégration dans la gestion d’un réseau électrique, Apports des convertisseurs multiniveaux au réglage des éoliennes à base de machine asynchrone à double alimentation,” Ecole Centrale de Lille, 2011.

[75] R. G. Ross, “Flat-Plate Photovoltaic Array Design Optimization,” in *14th IEEE Photovoltaic Specialists Conference*, 1980, pp. 1126–1132.

[76] P. Gilman, A. Dobos, N. DiOrio, J. Freeman, S. Janzou, and D. Ryberg, “SAM Photovoltaic Model Technical Reference SAM Photovoltaic Model Technical Reference,” *Sol. Energy*, vol. 63, no. May, pp. 323–333, 2015.

[77] P. Bajpai, V. Das, and N. Kishore, “Bi-annual sun tracking for solar PV module support structure: study and implementation,” *Sixt. Natl. Power Syst. Conf.*, pp. 56–61, 2010.

[78] A. J. Smets, K. O. Isabela, V. R. Swaail and M. Zeman, “*The physics and engineering of photovoltaic conversion, technologies and systems*,” Solar Energy. Cambridge: UIT, 2015.

[79] J. J. Michalsky, “The astronomical almanac’s algorithm for approximate solar position (1950–2050),” *Sol. energy*, vol. 40, pp. 227–235, 1988.

[80] A. B. Sproul, “Derivation of the solar geometric relationships using vector analysis,” *Renew. Energy*, vol. 32, no. 7, pp. 1187–1205, 2007.

[81] P. Axaopoulos, “Solar thermal conversion. Active solar systems.,” *Simmetria Publ.*, 2011.

[82] S. K. Chung, “A phase tracking system for three phase utility interface inverters,” *IEEE Trans. Power Electron.*, vol. 15, no. 3, pp. 431–438, 2000.

[83] WMO, “Giude to Meteorological Instruments and Methods of Observation,” vol. 8, pp. 5–13.

[84] M. Kolhe, S. Kolhe, and J. C. Joshi, “Economic viability of stand-alone solar photovoltaic system in comparison with diesel-powered system for India,” *Int. J. Electron. Electr. Engg.(IJEEE)*, vol. 24, pp. 155–165, 2002.

[85] S. C. Bhattacharyya, *Energy Economics: Concepts, Issues, Markets and Governance*, First Edition. New York , University of Dundee, UK, 2011.

[86] Ministry of Finance, “Taux d’inflation,” *Ministry of finance*, 2018. [Online]. Available: http://www.mf.gov.dz/index.php. [Accessed: 27-Aug-2018].

[87] Gloabal Energy Prices, “Electricity prices around the world,” 2018. [Online]. Available: https://www.globalenergyprices.com/en/electricity-prices/. [Accessed: 28-Jul-2018].

[88] M. Meyer-Renschhausen, “Evaluation of feed-in tariff-schemes in African countries,” *J. Energy South. Africa*, vol. 24, no. 1, pp. 56–66, 2013.

[89] D. E. Benhadji Serradj, “Design and performance analysis of a parabolic trough power plant under Tamanrasset climatological conditions” Pan African University, Institute of water and energy sciences (including climate change) of Tlemcen, 2016.

APPENDIX

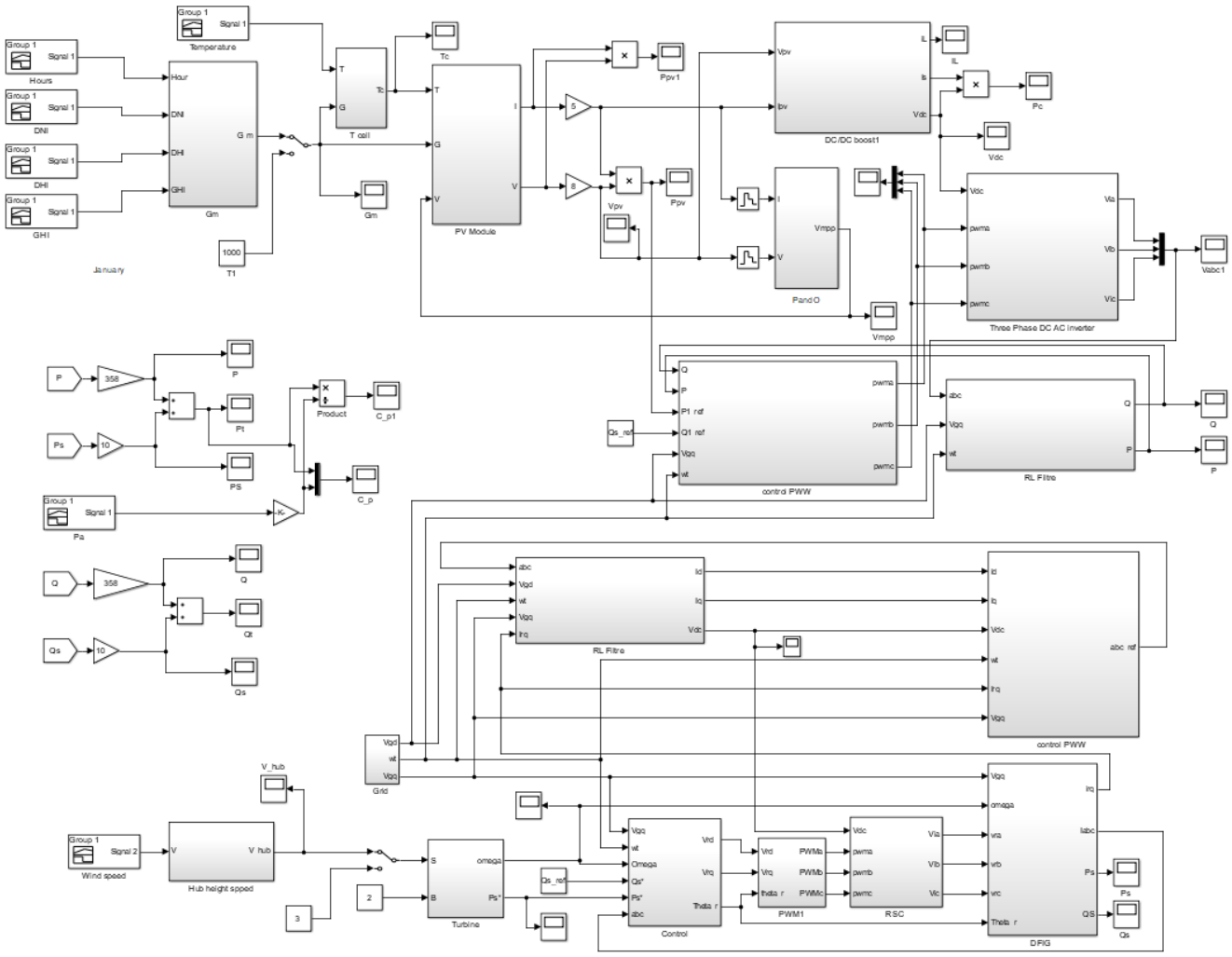

Figure A.1: Simulink model of the whole system

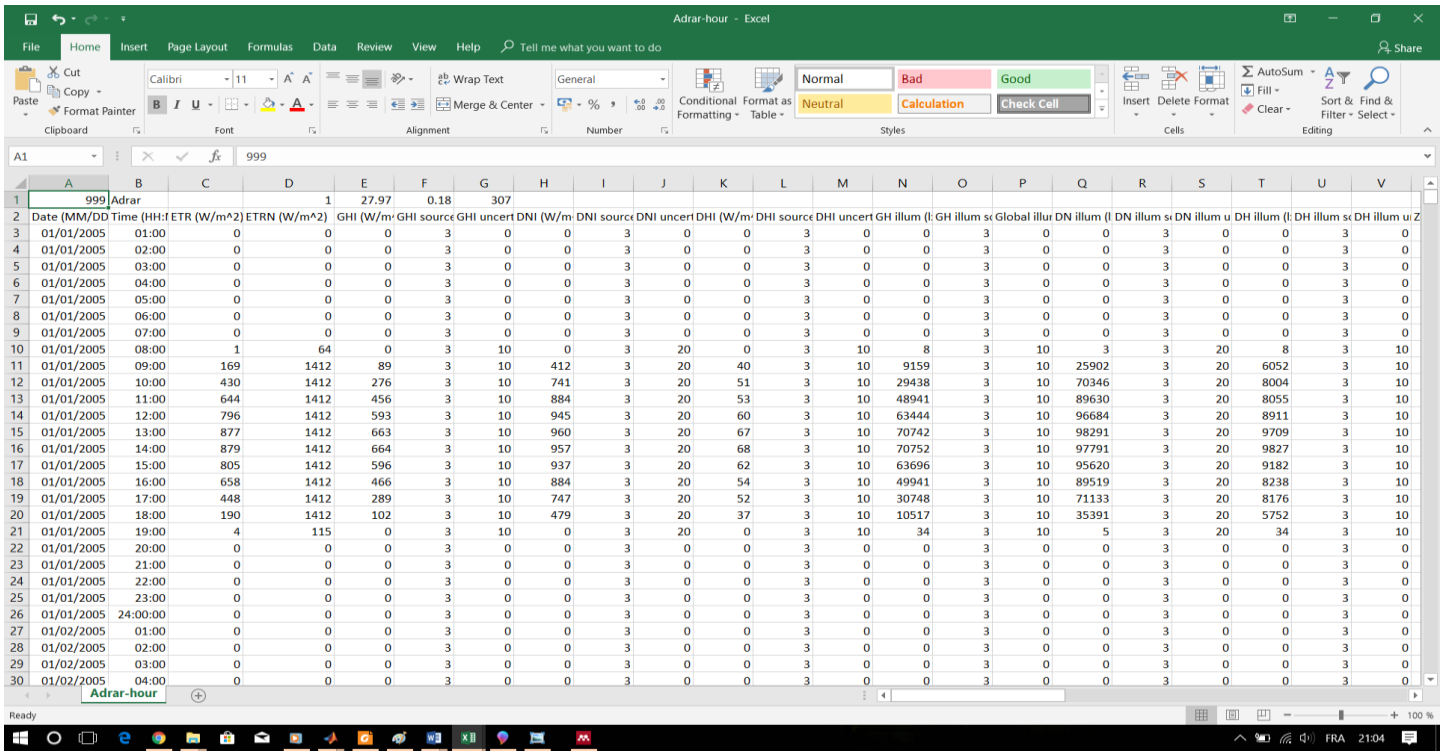

Figure A.2: Weather file

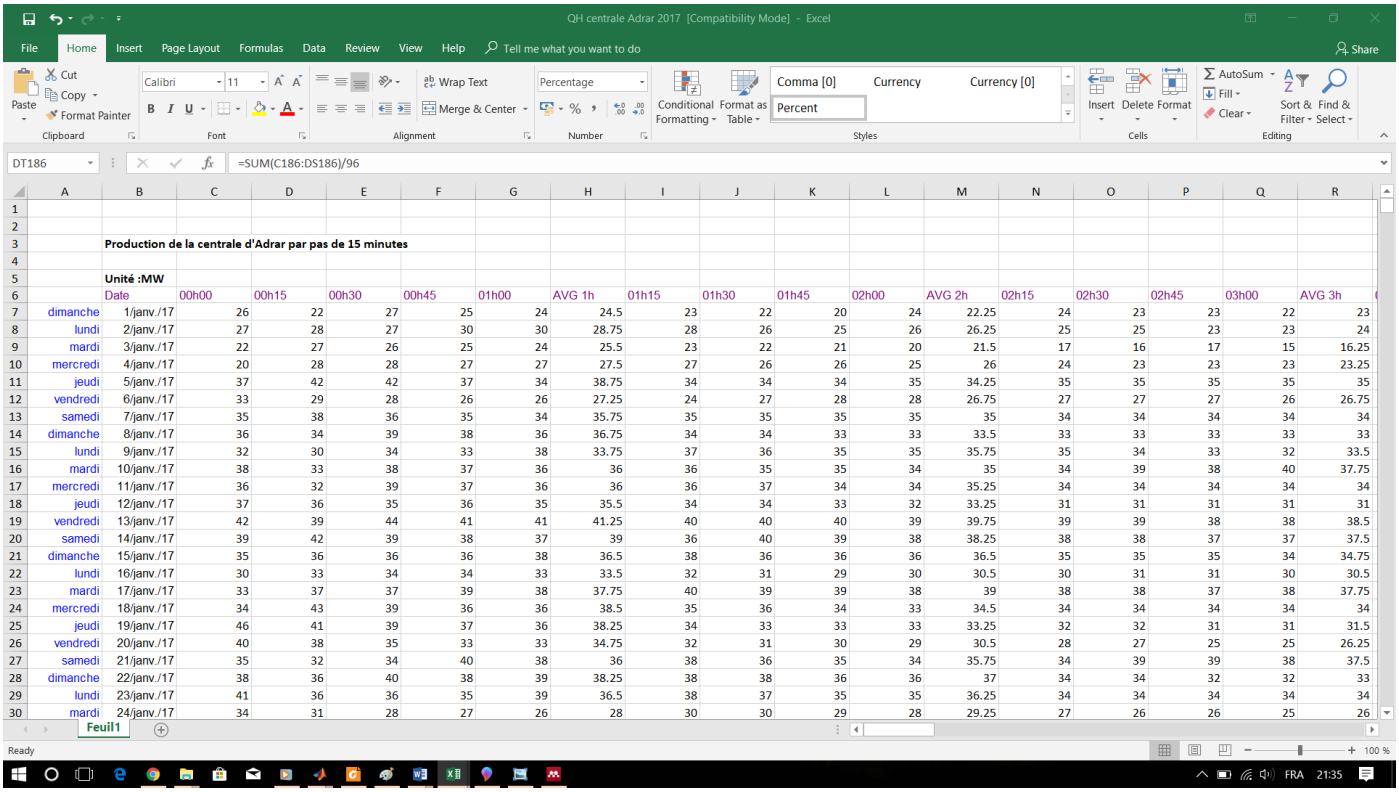

Figure A.3: Adrar central power plant production

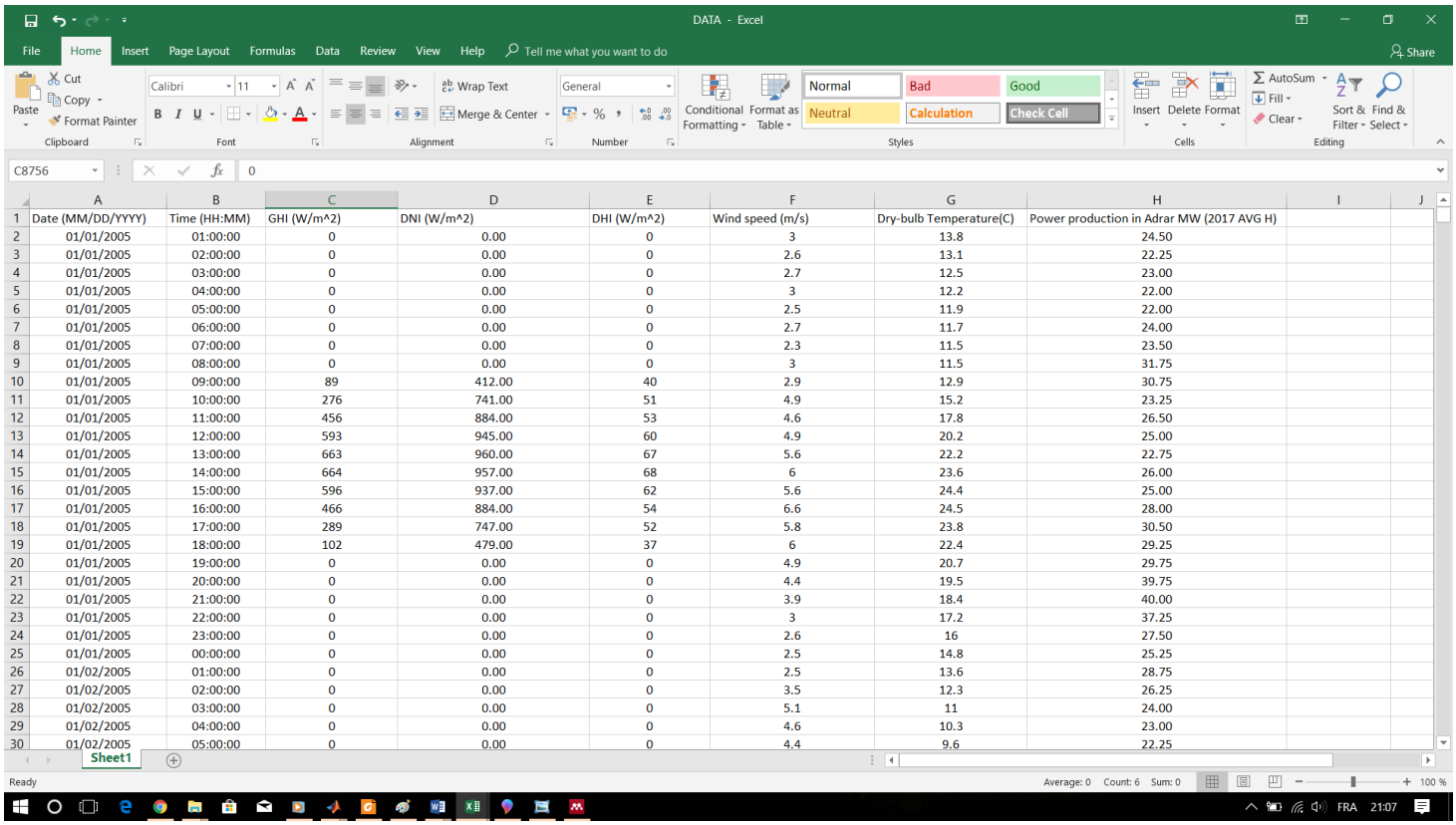

	A	B	C	D	E	F	G	H
1	Date (MM/DD/YYYY)	Time (HH:MM)	GHI (W/m^2)	DNI (W/m^2)	DHI (W/m^2)	Wind speed (m/s)	Dry-bulb Temperature(C)	Power production in Adrar MW (2017 AVG H)
2	01/01/2005	01:00:00	0	0.00	0	3	13.8	24.50
3	01/01/2005	02:00:00	0	0.00	0	2.6	13.1	22.25
4	01/01/2005	03:00:00	0	0.00	0	2.7	12.5	23.00
5	01/01/2005	04:00:00	0	0.00	0	3	12.2	22.00
6	01/01/2005	05:00:00	0	0.00	0	2.5	11.9	22.00
7	01/01/2005	06:00:00	0	0.00	0	2.7	11.7	24.00
8	01/01/2005	07:00:00	0	0.00	0	2.3	11.5	23.50
9	01/01/2005	08:00:00	0	0.00	0	3	11.5	31.75
10	01/01/2005	09:00:00	89	412.00	40	2.9	12.9	30.75
11	01/01/2005	10:00:00	276	741.00	51	4.9	15.2	23.25
12	01/01/2005	11:00:00	456	884.00	53	4.6	17.8	26.50
13	01/01/2005	12:00:00	593	945.00	60	4.9	20.2	25.00
14	01/01/2005	13:00:00	663	960.00	67	5.6	22.2	22.75
15	01/01/2005	14:00:00	664	957.00	68	6	23.6	26.00
16	01/01/2005	15:00:00	596	937.00	62	5.6	24.4	25.00
17	01/01/2005	16:00:00	466	884.00	54	6.6	24.5	28.00
18	01/01/2005	17:00:00	289	747.00	52	5.8	23.8	30.50
19	01/01/2005	18:00:00	102	479.00	37	6	22.4	29.25
20	01/01/2005	19:00:00	0	0.00	0	4.9	20.7	29.75
21	01/01/2005	20:00:00	0	0.00	0	4.4	19.5	39.75
22	01/01/2005	21:00:00	0	0.00	0	3.9	18.4	40.00
23	01/01/2005	22:00:00	0	0.00	0	3	17.2	37.25
24	01/01/2005	23:00:00	0	0.00	0	2.6	16	27.50
25	01/01/2005	00:00:00	0	0.00	0	2.5	14.8	25.25
26	01/02/2005	01:00:00	0	0.00	0	2.5	13.6	28.75
27	01/02/2005	02:00:00	0	0.00	0	3.5	12.3	26.25
28	01/02/2005	03:00:00	0	0.00	0	5.1	11	24.00
29	01/02/2005	04:00:00	0	0.00	0	4.6	10.3	23.00
30	01/02/2005	05:00:00	0	0.00	0	4.4	9.6	22.25

Figure A.4: Extracted data

Amerisolar | New Energy New World®

AS-6M

MONOCRYSTALLINE MODULE

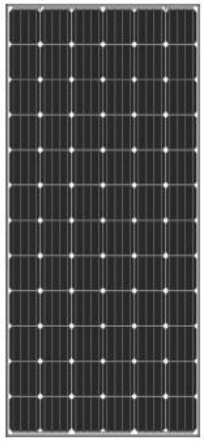

Passionately committed to delivering innovative energy solution

ADVANCED PERFORMANCE & PROVEN ADVANTAGES

- High module conversion efficiency up to 18.04% by using high efficient solar cells and advanced manufacturing technology.
- Low degradation and excellent performance under high temperature and low light conditions.
- Robust aluminum frame ensures the modules to withstand wind loads up to 2400Pa and snow loads up to 5400Pa.
- High reliability against extreme environmental conditions (passing salt mist, ammonia and hail tests).
- Potential induced degradation (PID) resistance.
- Positive power tolerance of 0 ~ +3 %.

CERTIFICATIONS

- IEC61215, IEC61730, IEC62716, IEC61701, CE, CQC, CGC, ETL(USA), JET(Japan), J-PEC(Japan), Kemco(South Korea), KS(South Korea), MCS(UK), CEC(Australia), FSEC(FL-USA), CSI Eligible(CA-USA), Israel Electric(Israel), InMetro(Brazil), TSE(Turkey)
- ISO9001:2008: Quality management system
- ISO14001:2004: Environmental management system
- OHSAS18001:2007: Occupational health and safety management system

SPECIAL WARRANTY

- 12 years limited product warranty.
- Limited linear power warranty: 12 years 91.2% of the nominal power output, 30 years 80.6% of the nominal power output.

ELECTRICAL CHARACTERISTICS AT STC

Nominal Power (P_{max})	310W	315W	320W	325W	330W	335W	340W	345W	350W
Open Circuit Voltage (V_{OC})	45.7V	45.8V	45.9V	46.0V	46.1V	46.2V	46.3V	46.4V	46.5V
Short Circuit Current (I_{SC})	8.83A	8.92A	9.02A	9.12A	9.21A	9.33A	9.45A	9.57A	9.68A
Voltage at Nominal Power (V_{mp})	37.1V	37.2V	37.3V	37.4V	37.5V	37.6V	37.7V	37.8V	37.9V
Current at Nominal Power (I_{mp})	8.36A	8.47A	8.58A	8.69A	8.80A	8.91A	9.02A	9.13A	9.24A
Module Efficiency (%)	15.98	16.23	16.49	16.75	17.01	17.26	17.52	17.78	18.04
Operating Temperature	-40°C to +85°C								
Maximum System Voltage	1000V DC								
Fire Resistance Rating	Type 1(in accordance with UL1703)/Class C(IEC61730)								
Maximum Series Fuse Rating	15A								

STC: Irradiance 1000W/m², Cell temperature 25°C, AM1.5

ELECTRICAL CHARACTERISTICS AT NOCT

Nominal Power (P_{max})	228W	232W	236W	239W	243W	247W	250W	254W	258W
Open Circuit Voltage (V_{OC})	42.1V	42.2V	42.3V	42.4V	42.5V	42.6V	42.7V	42.8V	42.9V
Short Circuit Current (Isc)	7.15A	7.23A	7.31A	7.39A	7.46A	7.56A	7.65A	7.75A	7.84A
Voltage at Nominal Power (V_{mp})	33.8V	33.9V	34.0V	34.1V	34.2V	34.3V	34.4V	34.5V	34.6V
Current at Nominal Power (I_{mp})	6.75A	6.85A	6.94A	7.01A	7.11A	7.20A	7.27A	7.37A	7.46A

NOCT: Irradiance 800W/m², Ambient temperature 20°C, Wind Speed 1 m/s

MECHANICAL CHARACTERISTICS

Cell type	Monocrystalline 156x156mm (6x6inches)
Number of cells	72 (6x12)
Module dimensions	1956x992x50mm (77.01x39.06x1.97inches)
Weight	23kg (50.7lbs)
Front cover	3.2mm (0.13inches) tempered glass with AR coating
Frame	Anodized aluminum alloy
Junction box	IP67, 3 diodes
Cable	4mm² (0.006inches²), 1000mm (39.37inches)
Connector	MC4 or MC4 compatible

TEMPERATURE CHARACTERISTICS

Nominal Operating Cell Temperature (NOCT)	45°C±2°C
Temperature Coefficients of P_{max}	-0.41%/°C
Temperature Coefficients of V_{OC}	-0.31%/°C
Temperature Coefficients of I_{SC}	0.05%/°C

PACKAGING

Standard packaging	21pcs/pallet
Module quantity per 20' container	210pcs
Module quantity per 40' container	462pcs(GP)/506pcs(HQ)

ENGINEERING DRAWINGS

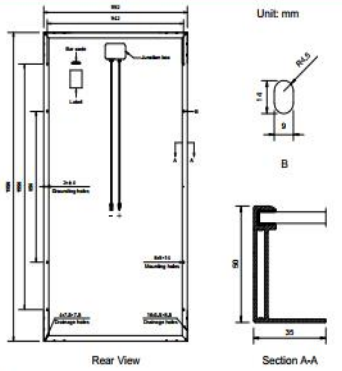

IV CURVES

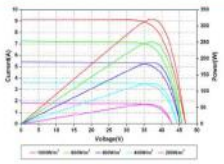

Current-Voltage and Power-Voltage Curves at Different Irradiances

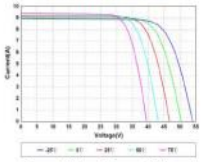

Current-Voltage Curves at Different Temperatures

Specifications in this datasheet are subject to change without prior notice.

Figure A.5: AS-6M data sheet

```
function y= fcn(i,k,o,p)
%Solar irradiation
%k=DNI   o=DHI    p=GHI
n=0;
phi=27.87429;            %latitude
L_st=0;           %standard meridian
L_loc=-0.29388;          %longitude
c=0;              %daylight savings
theta_m=23;        %tilt angle
phi_m=180;          %solar module azimuth
rho=0.2;            %ground albedo
T_off=1;          %time difference

SVF=0.5*(1+cosd(theta_m));
G_gnd=p*rho*(1-SVF);

  n=ceil(i/24);
  C=0.095+0.04*sind(360*(n-100)/365);
  delta=23.45*sind(360*(n-80)/365);
  B=(n-1)*360/365;
  ET=229.2*(0.000075+0.001868*cosd(B)-0.032077*sind(B)-0.014615*cosd(2*B)-0.04089*sind(2*B));
  %cos(w_)=-tan(phi)+tan(delta);
  G_dif=C*p*SVF;

    UT=(i/24-fix(i/24))*24-T_off;
    t=UT+ET+4;%*(L_st-L_loc)+c;

    w=15*(t-12);
    D=sind(delta)*sind(phi)+cosd(delta)*cosd(phi)*cosd(w);              %sin(a)
      %E=sin(phi)*sin(delta)+cos(phi)*cos(delta)*cos(w);              %cos(theta_z)
      %z=x*E+y;                                                       %GHI
    A=(cosd(phi)*sind(delta)-cosd(delta)*sind(phi)*cosd(w))/cosd(asind(D));      %cos(phi_s')

if w>0

    phi_s=360-acosd(complex(A));

else

    phi_s=acosd(complex(A));

end

    F=cosd(asind(complex(D)))*cosd(phi_s-phi_m)*sind(theta_m)+D*cosd(theta_m);     %cos(gama)

          G_dir=k*F;


      G=G_dir+G_dif+G_gnd;

y = real(G);
```

Figure A.6: MATLAB irradiance algorithme.

Table A.1: Main characteristics of the AS-6M module

I_{sc}	Short circuit current (A)	9.68
k_i	Short circuit current of cell at 25 °C and 1000 w/m^2	5×10^{-4}
q	Electron charge (C)	1.6×10^{-19}
V_{oc}	Open circuit voltage (V)	46.5
n	The ideality factor of the diode	1.2
K	Boltzman's constant (J/K)	1.38×10^{-23}
E_{g0}	Band gap energy of the semiconductor (eV)	1.12
N_s	Number of cells connected in series	72
R_s	Series resistor (Ω)	0.100
R_{sh}	Shunt resistor (Ω)	515
P_{max}	Maximum output power(W)	350
V_{mpp}	Maximum power voltage(V)	37.9
I_{mpp}	Maximum power current(A)	9.24

Table A.2: Parameters of the wind system

System	Parameter
Turbine	Number of blades:3
	R=45m
	J_t=1.4 .10^6 kg.m²
	V_n=13 m/s ,N_{tn}=19 rpm
Gear box	G=100
DFIG	$U_r = U_s$= 690 V
	P_n = 3MW, f = 50 Hz, p = 2, Nr/Ns ≈ 1
	R_s = 2.97 mΩ, R_r = 3.82 mΩ
	L_{fs} = 121 µH, L_{fr} = 57.3 µH, L_m = 12.12 mH
	J_g = 114 kg.m²
DC bus	C = 38 mF, V_{dc} = 1200 V
RL Filter	R_f = 0.75 Ω, L_f = 0.75 mH
Grid	U = 690 V, f = 50 Hz

Table A.3: Control parameters of the wind system

Control	Parameter
MPPT	λ_{opt} = 7.07
	C_{pmax} = 0.35
Rotor currents	Response time: t_r = 0.05 s
	$K_{pr} = 3.\sigma.\frac{L_r}{t_r} \approx 0.01062$
	$K_{ir} = 3.\frac{R_r}{t_r} \approx 0.2292$
Stator currents	Response time: t_{rf} = 0.01 s
	$K_{pf} = 3.\frac{L_f}{t_{rf}} \approx 0.3$
	$K_{if} = 3.\frac{R_{rf}}{t_{rf}} \approx 30$

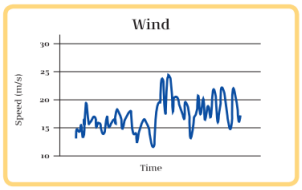

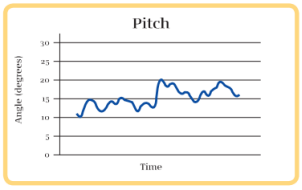

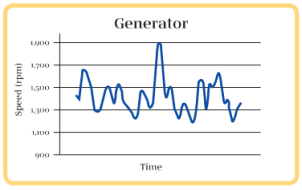

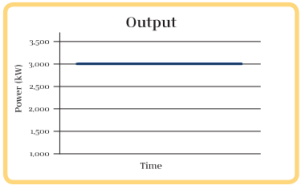

OptiSpeed® allows the rotor speed to vary within a range of approximately 60 per cent in relation to nominal rpm. Thus with OptiSpeed®, the rotor speed can vary by as much as 30 per cent above and below synchronous speed. This minimises both unwanted fluctuations in the output to the grid supply and the loads on the vital parts of the construction.

**Vestas OptiSpeed® is not available in the USA and Canada.*

Rotor

Diameter:	90 m
Area swept:	6,362 m²
Nominal revolutions:	16,1 rpm
Operational interval:	8,6-18,4 rpm
Number of blades:	3
Power regulation:	Pitch/OptiSpeed®
Air brake:	Full blade pitch by three separate hydraulic pitch cylinders.

Tower

Hub height: 80 m, 105 m

Operational data

Cut-in wind speed:	4 m/s
Nominal wind speed:	15 m/s
Cut-out wind speed:	25 m/s

Generator

Type:	Asynchronous with OptiSpeed®
Rated output:	3,000 kW
Operational data:	50 Hz 1,000 V

Gearbox

Type: Two planetary and one helical stage

Control

Type: Microprocessor-based control of all the turbine functions with the option of remote monitoring. Output regulation and optimisation via OptiSpeed® and OptiTip® pitch regulation.

Weight

Nacelle:	70 t
Rotor:	41 t

Towers:

Hub height:	IEC IA	IEC IIA	DIBt II	DIBt III
80 m	160 t	-	-	160 t
105 m	-	285 t	235 t	-

t = metric tonnes.

DIB towers are only approved for Germany.

All specifications subject to change without notice.

Figure A.7: Data sheet of the Vestas V90

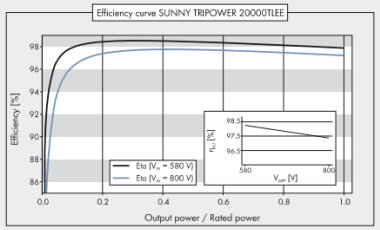

Accessories


RS485 interface DM-485CIB-10


Speedwire/Webconnect interface SWDM-10


Multi-function relay MFR01-10


Power Control Module PWCMOD-10

* Does not apply to all national appendices of EN 50438
Provisional data, as of July 2013

Provisional Technical Data	Sunny Tripower 15000TL	Sunny Tripower 20000TL
Input (DC)		
Max. DC power (@ cos ϕ = 1)	15 260 W	20 450 W
Max. input voltage	1 000 V	1 000 V
MPP voltage range with a line voltage of 230 V / rated input voltage	580 V – 800 V / 580 V	580 V – 800 V / 580 V
Min. input voltage / start input voltage	570 V / 620 V	570 V / 620 V
Max. input current	36 A	36 A
Max. input current per string	36 A	36 A
Number of independent MPP inputs / strings per MPP input	1 / 6	1 / 6
Output (AC)		
Rated power (@ 230 V, 50 Hz)	15 000 W	20 000 W
Max. apparent AC power	15 000 VA	20 000 VA
Nominal AC voltage	3 / N / PE, 230 V / 400 V	3 / N / PE, 230 V / 400 V
Nominal AC voltage range	160 V – 280 V	160 V – 280 V
AC power frequency / range	50 Hz, 60 Hz / −6 Hz, +5 Hz	50 Hz, 60 Hz / −6 Hz, +5 Hz
Rated power frequency / rated grid voltage	50 Hz / 230 V	50 Hz / 230 V
Max. output current	24 A	29 A
Power factor at rated power	1	1
Displacement power factor, adjustable	0.8 overexcited ... 0.8 underexcited	0.8 overexcited ... 0.8 underexcited
Feed-in phases / connection phases	3 / 3	3 / 3
Efficiency		
Max. efficiency / European weighted efficiency	98.5 % / 98.3 %	98.5 % / 98.2 %
Protective devices		
DC-side disconnection device	○	○
Ground fault monitoring / grid monitoring	● / ●	● / ●
DC surge arrester (type II), can be integrated	–	–
DC reverse polarity protection / AC short-circuit current capability / galvanically isolated	● / ● / –	● / ● / –
All-pole-sensitive residual-current monitoring unit	●	●
Protection class (as per IEC 62103) / overvoltage category (as per IEC 60664-1)	I / III	I / III
General data		
Dimensions (W/H/D)	665 / 680 / 265 mm (26.2 / 26.8 / 10.4 inch)	665 / 680 / 265 mm (26.2 / 26.8 / 10.4 inch)
Weight	45 kg (99.2 lb)	45 kg (99.2 lb)
Operating temperature range	−25 °C ... +60 °C (−13 °F ... +140 °F)	−25 °C ... +60 °C (−13 °F ... +140 °F)
Noise emission (typical)	51 dB(A)	51 dB(A)
Self-consumption (at night)	1 W	1 W
Topology / cooling concept	Transformerless / OptiCool	Transformerless / OptiCool
Degree of protection (per IEC 60529)	IP65	IP65
Climatic category (as per IEC 60721-3-4)	4K4H	4K4H
Maximum permissible value for relative humidity (non-condensing)	100 %	100 %
Features		
DC terminal	SUNCLIX	SUNCLIX
AC connection	Spring clamp terminal	Spring clamp terminal
Display	Chart	Chart
Interfaces: RS485, Bluetooth®, Speedwire/Webconnect	○/●/○	○/●/○
Multi-function relay / Power Control Module	○/○	○/○
Warranty: 5 / 10 / 15 / 20 / 25 years	●/○/○/○/○	●/○/○/○/○
Certificates and approvals (more available on request)	AS 4777, BDEW 2008, C10/11, CE, CEI 0-21, EN 50438*, G59/2, IEC 61727, IEC 62109-1/-2, NEN EN 50438, PPC, PPDS, RD 1699, RD 661/2007, SI4777, UTE C15-712-1, VDE 0126-1-1, VDE-AR-N 4105	
Type designation	STP 15000TLEE-10	STP 20000TLEE-10

● Standard features ○ Optional features – Not available – Data at nominal conditions

www.SMA-Solar.com SMA Solar Technology

Figure A.8: Data sheet of the inverter

Table A.4: Description of research grant use

Items \ Time		March	April	May	June	July	Cost ($)	DZD
Trips	Tlemcen-Adrar Tlemcen-Algiers Tlemcen-Hassi Messoud						390 245 150	46000 28590 17000
Transport	Algiers						65	7490
Lodging	Algiers (Internship)						690	81500
Software	Matlab						450	53000
	Homer Meteonorm						210 60	25000 7000
Printing, Internet, Mobility and General supplies							250	29560
Contingency							200	24000
Conference							680	80000
Total							3325	392140

Two internships were conducted in April and in July, the expenses for commutation and the total number of trips from the hometown to the internship place amount to $245 for the first internship in Algiers which lasted 30 days, and $150 for the trips to Hassi Messoud including a one-way flight. Local transport in Algiers cost $65, this includes transport from the hotel to the internship place. Housing in a humble hotel cost $690 for nearly one month, and three software tools were used to simulate the designed system, Homer which cost $210, MATLAB costs 450 for a one-year license including all modules, and meteorological data for Adrar generated by meteonorm was purchased for just $60.

For the load profile of Adrar, data was obtained from Sonelgaz of Adrar and the round trip by taxi cost $390. In addition, a conference on renewable energy in Tunisia was attended by the student in March which cost about $680 total. For mobility, internet and printing the total amount spent is $250 plus the contingency sum of $200.

The table above details all the expenses that were covered by the research grant.